

# FROM DIFFUSION MRI TO BRAIN CONNECTOMICS

THÈSE N° 3230 (2005)

PRÉSENTÉE À LA FACULTÉ SCIENCES ET TECHNIQUES DE L'INGÉNIEUR

Institut de traitement des signaux

PROGRAMME DOCTORAL EN INFORMATIQUE ET COMMUNICATIONS

ÉCOLE POLYTECHNIQUE FÉDÉRALE DE LAUSANNE

POUR L'OBTENTION DU GRADE DE DOCTEUR ÈS SCIENCES

PAR

**Patric HAGMANN**

Docteur en médecine, Université de Lausanne  
de nationalité suisse et originaire de Däniken (SO)

acceptée sur proposition du jury:

Prof. J.-P. Thiran, Prof. R. Meuli, directeurs de thèse  
Prof. P. Magistretti, rapporteur  
Prof. K. Prüssmann, rapporteur  
Prof. V. J. Wedeen, rapporteur

Lausanne, EPFL  
2005



*Science sans conscience n'est que ruine de  
l'âme...*

Rablais



## Acknowledgements

There are so many people to thank that I don't really know how to begin; I just hope I won't forget anybody. Let's maybe start with my advisors, Jean-Philippe Thiran and Reto Meuli, who gave me the opportunity to acquire a scientific education and who were sufficiently confident in my capabilities to let an M.D. work on a technical research project. They are also the persons who, at the right time, saw the interesting perspectives of diffusion MRI and oriented me in this exciting research area. There is actually a hidden, third advisor. I had the chance to meet Van Wedeen, not only an exceptional scientist with an incredible intuition but also a very generous person who is keen on sharing his ideas and knowledge. Many of the ideas developed in this thesis come from our endless and captivating discussions. For all that, I would like to thank him. Then there is Leila Cammoun, together with her, we realized this complex study on language networks and I would like to thank her for her dedication to this project. I had the chance to share my office with an incredibly joyful and pleasant person. Lisa Jonasson and I were simultaneously involved in diffusion MRI; we spent lots of time, sharing ideas, enthusiasm and despair. Then there are all these guys in the lab, who helped me punctually on subjects as various as, mathematics, physics, programming and computer OS installation as well as recovering my lost data after a system crashes. I would like to thank, Olivier Cuisenaire, Pierre Vanderghynst, Oscar Divorra, Simon Chatelain, Diego Santa-Cruz, Xavier Bresson, Roberto Martuzzi and all the other anonymous I have forgotten. It is maybe also important to mention that Signal Processing Institute at EPFL as well as Department of Radiology at CHUV, my both hosting institutions, are ideal research places as personal initiatives are encouraged and the people working there are pleasant and positively minded. Finally I would like to thank my beloved Myriam for her endless and essential support.

Financially I was supported over these three years by a grant coming from the Swiss National Science Foundation (3235B0-102868) and by a generous private donator, Mr. Yves Paternot, that I would like to thank here.



---

# Contents

---

<b>1</b>	<b>Preface</b>	<b>1</b>
1.1	Context . . . . .	1
1.2	Approach and Outline . . . . .	1
1.3	Main contributions . . . . .	2
<b>I</b>	<b>Diffusion MRI</b>	<b>5</b>
<b>2</b>	<b>Basics in Diffusion MRI</b>	<b>7</b>
2.1	Introduction . . . . .	7
2.2	One-Dimensional Description of Molecular Diffusion . . . . .	8
2.2.1	Macroscopic Description . . . . .	8
2.2.2	Microscopic Description . . . . .	9
2.3	Displacement of One Spin . . . . .	11
2.4	Voxel Averaged Spin Displacements . . . . .	12
2.5	Diffusion Anisotropy in the Brain . . . . .	13
2.6	Diffusion Contrast . . . . .	13
2.7	Signal-Propagator Fourier Relationship . . . . .	15
2.8	$\delta$ -Averaged Displacement . . . . .	16
2.9	Diffusion Tensor Imaging . . . . .	17
2.9.1	Imaging the ADC . . . . .	17
2.9.2	Imaging the Diffusion Tensor . . . . .	18
2.9.3	Mean Diffusion, Fractional Anisotropy and Diffusion Color Maps . .	19
<b>3</b>	<b>Why Diffusion Contrast is Positive</b>	<b>21</b>
3.1	Introduction . . . . .	21
3.2	Positivity Under the Narrow Pulse Approximation . . . . .	22
3.2.1	Problem Formulation . . . . .	22
3.2.2	The Diffusion Process as a Markov Chain . . . . .	23
3.2.3	The Fourier Transform of the Diffusion Spectrum . . . . .	23

3.3	Finite Duration Diffusion Encoding . . . . .	24
3.4	Conclusions . . . . .	26
<b>4</b>	<b>Diffusion Spectrum Magnetic Resonance Imaging</b>	<b>29</b>
4.1	Introduction . . . . .	29
4.2	Theory . . . . .	30
4.3	Methods . . . . .	30
4.4	Results . . . . .	32
4.5	Discussion . . . . .	37
4.5.1	A General Approach for Biological Samples . . . . .	37
4.5.2	Diffusion Spectrum and Fiber Orientation . . . . .	37
4.5.3	DSI vs Other Diffusion MRI Techniques . . . . .	38
4.6	Conclusion . . . . .	39
<b>II</b>	<b>Tractography: Between Contrast Mechanism and Axonal Model- ing</b>	<b>41</b>
<b>5</b>	<b>Statistical Fibre Tracking and Virtual Dissection from DTI</b>	<b>43</b>
5.1	Introduction . . . . .	43
5.2	Material and Methods . . . . .	44
5.2.1	MRI Data Acquisition . . . . .	44
5.2.2	Data Pre-processing . . . . .	44
5.2.3	Statistical Axonal Trajectories . . . . .	45
5.2.4	Tract Selection or Virtual Dissection . . . . .	46
5.2.5	Various Connectivity Maps . . . . .	48
5.3	Results . . . . .	49
5.3.1	Cortico-Bulbar and Cortico-Spinal Tracts . . . . .	50
5.3.2	Cortico-Thalamic Projections . . . . .	51
5.3.3	Corpus Callosum and Limbic System . . . . .	51
5.3.4	Cortical Association Bundles . . . . .	51
5.3.5	Cerebellar Peduncles and Medial Lemniscus . . . . .	54
5.4	Discussion . . . . .	55
<b>6</b>	<b>DSI Tractography in Complex Cerebral White Matter</b>	<b>59</b>
6.1	Introduction . . . . .	59
6.2	Methods . . . . .	60
6.2.1	MR Acquisition . . . . .	60
6.2.2	Tractography . . . . .	60
6.3	Results . . . . .	61
6.3.1	Study of the Pons . . . . .	61
6.3.2	Study of the Centrum Semi-Ovale . . . . .	62
6.4	Discussion . . . . .	65



6.5	Conclusion . . . . .	66
<b>7</b>	<b>Tractography by Segmentation in Position Orientation Space</b>	<b>67</b>
7.1	Introduction . . . . .	67
7.2	Theory . . . . .	68
7.2.1	What is Position-Orientation Space? . . . . .	68
7.2.2	Segmentation of POS in Two Classes . . . . .	70
7.2.3	Fibertract Labelling . . . . .	73
7.3	Material . . . . .	73
7.4	Results . . . . .	73
7.5	Conclusion . . . . .	73
<b>III</b>	<b>Human Brain Neuronal Network Topology</b>	<b>77</b>
<b>8</b>	<b>Hand Preference and Gender Shape the Architecture of Language Networks</b>	<b>79</b>
8.1	Introduction . . . . .	79
8.2	Methods . . . . .	80
8.3	Results . . . . .	81
8.3.1	Intra-hemispheric connectivity . . . . .	82
8.3.2	Inter-hemispheric connectivity . . . . .	84
8.4	Discussion . . . . .	88
<b>9</b>	<b>Does Human Brain Axonal Connectivity Form a Small World Network?</b>	<b>91</b>
9.1	Introduction . . . . .	91
9.2	Methods . . . . .	92
9.2.1	Constructing the Brain Connectivity Graph . . . . .	92
9.2.2	Construction of an Equivalent Random Graph . . . . .	94
9.2.3	Various Graph Measures . . . . .	94
9.3	Results . . . . .	95
9.4	Discussion . . . . .	97
<b>10</b>	<b>Axonal Network Topology Reveals the Hierarchical Organization of the Human Brain</b>	<b>99</b>
10.1	Introduction . . . . .	99
10.2	Methods . . . . .	100
10.3	Results . . . . .	101
10.4	Discussion . . . . .	102
<b>11</b>	<b>Conclusion: Towards Brain Connectomics?</b>	<b>107</b>
11.1	Achievements . . . . .	107

11.2 Perspectives . . . . .	108
11.2.1 Technical Improvements . . . . .	108
11.2.2 Defining the Brain Connectome . . . . .	108
<b>Bibliography</b>	<b>111</b>
<b>Curriculum Vitæ</b>	<b>123</b>

---

# Version Abrégée

---

Le succès de l'IRM de diffusion est profondément enraciné dans le fait que durant leur déplacement aléatoire les molécules d'eau dans un échantillon biologique explorent sa structure. En marquant magnétiquement les protons liés aux molécules d'eau qui se déplacent, l'IRM de diffusion fournit un reflet de la taille et de l'orientation des divers compartiments présents dans le tissu étudié. C'est par la relation causale entre d'un côté la mesure de la mobilité restreinte et orientée des molécules et de l'autre côté l'orientation des axones dans la matière blanche cérébrale, que l'IRM de diffusion est devenue une méthode puissante pour l'étude de la connectivité cérébrale et de l'architecture de ses fibres nerveuses.

Cet travail est non seulement un voyage, qui nous emmène de la physique de l'IRM de diffusion jusqu'à l'étude de la circuiterie neuronale du cerveau, mais aussi une thèse visant à démontrer la puissance de l'analyse à grande échelle de la connectivité cérébrale où chaque composant technologique nécessaire à sa mesure est essentiel.

Suite à une petite introduction sur la diffusion moléculaire et l'IRM de diffusion, nous commençons par montrer que le contraste IRM de diffusion est réel et positif. Ceci est un point clé, qui jusqu'à présent n'avait été que postulé. En effet, cette propriété du signal IRM permet de justifier que pour mesurer correctement la diffusion le seul module du signal est nécessaire. Diverses techniques IRM émergentes qui mesurent une diffusion non gaussienne peuvent dès lors trouver une justification fondée. En particulier, ce résultat nous permet de calculer la distribution du déplacement des molécules d'eau en prenant la transformée de Fourier du seul module du signal et par là faire de l'Imagerie du Spectre de Diffusion. Nous illustrons le potentiel de cette technique par diverses expériences, dans lesquelles l'on voit de quelle manière cette distribution dans un tissu biologique aux multiples et tortueux compartiments peut être mesuré, et comment l'hétérogénéité mesurée est un miroir de l'architecture axonale.

La tractographie est le lien nécessaire qui permet, à partir de mesures IRM, de reconstruire, in vivo, les trajectoires de fibres nerveuses ainsi que des cartes de connectivité cérébrale. Dans cette thèse deux algorithmes sont proposés, alors que le premier est développé pour l'IRM du tenseur de diffusion, le second est façonné pour l'IRM de diffusion à haute résolution angulaire et est spécifiquement testé sur des images acquises en IRM du Spectre de Diffusion. Après avoir considéré les avantages et les limites de ces algorithmes de traçage, nous nous posons la question si la tractographie peut être formulée comme

un problème de segmentation dans un espace non-euclidien de haute dimension: l'espace position-orientation.

C'est à l'aide de ces outils que nous formulons quelques questions neuroscientifiques d'importance. En se basant sur les images cérébrales acquises chez 32 volontaires sains en IRM du tenseur de diffusion, le réseau neuronal du langage est étudié. Il en ressort que les hommes droitiers sont massivement interconnectés entre aires du langage dans l'hémisphère gauche alors qu'entre les régions homologues à droite cette connectivité est faible. Ceux-ci ont aussi des connections interhémisphériques importantes entre aires du langage et leurs homologues contralateral. Chez les hommes gauchers ainsi que les femmes cette connectivité intrahémisphérique semble égale dans les deux hémisphères, mais les femmes ont une densité de connections interhémisphérique plus importante. Après cette étude quantitative, nous étudions la organisation globale des connections cérébrales d'un sujet avec l'aide d'une acquisition en IRM du Spectre de Diffusion et de la tractographie. Ici la clé est de modéliser cette connectivité à l'échelle du cerveau entier par un graphe abstrait. Ceci nous permet de démontrer que le réseau ainsi formé est de topologie "petit monde", ou "small world" en anglais. C'est un type d'architecture bien particulier qui se retrouve dans de multiples réseaux de communication de grande échelle. Ceux-ci résultent en général d'un processus de développement où l'optimalité de la capacité de communication entre composants est modulée par des limites de ressources. D'autre part nous montrons aussi que l'architecture de la connectivité axonale entre aires corticales est aussi organisée hiérarchiquement. Ces résultats, qui confirment des études bien moins directes, nous permet de mettre en perspective l'histoire de l'évolution cérébrale, le développement cérébral ainsi que le traitement de l'information au niveau du cerveau tout entier.

---

# Abstract

---

The success of diffusion MRI is deeply rooted in the fact that during their micrometric random displacements water molecules explore tissue microstructure. Hence by labeling magnetically spins of displaced water, diffusion MRI provides us with exquisite information about the sizes and orientations on the multiple compartments present inside an imaging voxel. Through the causal relation between on one hand the imaged restricted and oriented water mobility and on the other hand the axonal orientations in brain white matter, diffusion MRI has become a powerful method to infer fiber tract architecture and brain anatomic connectivity.

This work is not only a journey that takes us from essential diffusion MRI physics to an investigation of the brain neuronal circuitry, but also a thesis aiming at demonstrating the power of large scale analysis of brain connectivity, where every technological component is essential.

After a short introduction on molecular diffusion and diffusion NMR, we start by showing that diffusion contrast is positive. This key issue that was only postulated up to now, allows us to justify why diffusion can be computed accurately with the only signal modulus. Accordingly, various emerging MRI techniques that map non-Gaussian diffusion have found a sound justification. In particular it is precisely the result that allows us to map distribution of diffusion related spin displacements by Fourier transformation of the measured signal modulus, hence to do Diffusion Spectrum MRI. We show through multiples MR experiments how the shape of this distribution in a complicated multi-compartment biological system can be measured and how its characteristic local heterogeneity is a mirror of fiber architectures. We discuss in detail its interpretation and its relation to other diffusion MRI techniques.

Tractography is the necessary link that from diffusion MRI provides us with nerve fiber trajectories and maps of brain axonal connectivity. In this thesis two algorithms are proposed, while the first is designed for diffusion tensor MRI, the second is shaped for high angular resolution diffusion MRI and specifically tested on Diffusion Spectrum MRI. After having considered the potentials and the limitations of these line generation algorithms, we investigate whether tractography can be formulated as a segmentation problem in a high dimensional non Euclidean space, i.e. position-orientation space.

With the help of the developed tools we address some key neuro-scientific questions.

Based on diffusion tensor MRI data of 32 healthy volunteers, language networks are investigated. It is shown that right-handed men are massively interconnected between the left-hemisphere speech areas whereas the homologous in the right hemisphere are sparse; furthermore interhemispheric connections between the speech areas and their contralateral homologues are relatively strong. Women and left-handed men have equally strong intrahemispheric connections in both hemispheres, but women have a higher density of interhemispheric connections. After this quantitative study, Diffusion Spectrum MRI data of a single subject is collected and tractography performed in order to analyze the global connectivity pattern of the human brain. For this purpose we propose to model this large scale architecture by an abstract graph. It is shown that the long-range axonal network exhibits a "small world" topology. This type of particular architecture is present in various large scale communication networks. They emerge usually from a growing process where optimal communication has to be developed under some resource constraints. Furthermore we show also that the architecture of axonal connectivity between cortical areas exhibits a hierarchical organization. These results, which confirm more indirect studies, provide essential material to discuss not only brain evolution and development but also information processing at the level of the brain.

---

# Preface

---

## 1.1 Context

Diffusion MRI has become over the last decade an important area of MRI research, boosted by established successes in clinical neuro-diagnostics and foreseen powerful new applications for the study of brain anatomy in-vivo. While the current clinical applications are mainly acute stroke management [135, 136, 157] and in a smaller extent axonal "integrity" measurements [78], it is clearly the potential use of diffusion MRI for the study of neural fiber tract anatomy and brain connectivity that is responsible for the current tremendous research effort in this domain.

While during last decade diffusion MRI has been dominated by the Diffusion Tensor (DT) model \*, currently more and more researchers recognize its limitations for axonal connectivity inference and turn their interest towards techniques with better "angular" resolutions†. Important issues have not yet found their definite answers in the domain and are currently discussed in the scientific community. Can water diffusion be precisely and rigorously inferred from the modulus of the diffusion encoded signal? What is the exact relation between water diffusion and axonal anatomy? What does tractography really measure? How should brain connectivity be quantified from diffusion MRI? What can we do with tractography?

## 1.2 Approach and Outline

With the help of various experiments and theoretical arguments, the present work investigates many of those issues. Beside the answers that this thesis provides to some specific questions, it aims also at demonstrating the power of large scale analysis of brain connec-

---

\*For overview see the November-December 2002 special issue of *NMR in Biomedicine*.

†An excellent overview of early work in that area can be found in the thesis of D. Tuch [150].

tivity. In order to emphasize the three essential steps on the way from the MRI acquisition to brain anatomical connectivity analysis this work is organized in three parts.

After a primer on diffusion and diffusion MRI, we address a fundamental question of diffusion MRI. Indeed, in the context of emerging "high angular resolution" diffusion MR techniques, the critical positivity issue of diffusion contrast must be clarified. With the help of various experiments, we then go through a comprehensive analysis of diffusion spectrum MRI, a six-dimensional diffusion imaging modality of high angular resolution. To make the link between diffusion imaging and brain connectivity, we consequently propose two tractography algorithms, one for the well established DT-MRI and one for the rather recent diffusion spectrum MRI. While the essential aspects of Part I and II are respectively diffusion MRI physics and algorithmic modeling, Part III addresses neuro-scientific questions. We investigate the specific architecture of language networks, and borrow from communication science concepts on large-scale networks in order to analyze the global topology or organization of the human brain neuronal network, essential aspect of modern integrative neurosciences.

Although a thesis is a personal work, its scientific content is always the result of an intense collaboration. Therefore I have chosen to write this thesis using "we" instead of "I", it is a way for me acknowledge all my great collaborators.

### 1.3 Main contributions

The main contributions of this dissertation can be summarized as follows.

- Demonstration that under some weak assumptions diffusion contrast is positive, key issue for justifying emerging MRI techniques that map non-Gaussian diffusion by measuring the only signal modulus.
- Based on multiple MR experiments, comprehensive analysis of Diffusion Spectrum MRI and its relation to other diffusion MRI techniques.
- Development of a DT-MRI tractography method.
- Development of a tractography method designed for high angular diffusion MRI data and tested on Diffusion Spectrum MRI data.
- Using a hidden Markov random field model, development of a segmentation algorithm in a five-dimensional space of position and orientation in order to identify fiber tracts in brain white matter.
- Demonstration of the non trivial relationship between gender and handedness with the intra- and inter-hemispheric anatomical architecture of language networks.
- Demonstration that long-range axonal human brain connectivity forms a small world network.



- 
- Demonstration that the hierarchical organization of human cortex connectivity can be revealed by the study of the topology of the brain neuronal network.



**Part I**

**Diffusion MRI**



---

# Basics in Diffusion MRI

---

# 2

*I will be brief. Not nearly as brief as Salvador Dali, who gave the World's shortest speech. He said, "I will be so brief I have already finished", and he sat down.*

E. O. Wilson

## 2.1 Introduction

This chapter aims at reviewing the basic principles behind water molecular diffusion and diffusion weighted MRI. We will, however, not discuss the basics of NMR or MRI, concepts that are on one hand very widely explained in the didactic books (see for example [28, 29]) and on the other hand not really essential to understand this thesis. Hence the not-expert reader will just have to take for granted some equations of Section 2.6 in order to be able to follow the rest of the text.

It is probably not so wrong to say that the large majority of the literature discussing the principles of scalar and tensor valued diffusion MRI shares two constant features (see for examples [9, 97] and [7, 98, 99, 100, 102] for review). First, diffusion is always addressed with the use of the macroscopic diffusion equation. Second, diffusion is considered Gaussian and formulas are derived from this assumption. It has its reason: simplicity. But nature is complex and therefore needs sometimes more subtle tools to keep it simple. Therefore and in order to avoid repeating too much the literature, this chapter is an attempt to go over the basic material, with the formalism that we use in next chapters where general diffusion processes is discussed. Accordingly, we will introduce concepts that, while not really necessary for scalar or tensor imaging, are going to be very useful later on.

## 2.2 One-Dimensional Description of Molecular Diffusion

### 2.2.1 Macroscopic Description

A drop of water-soluble dye placed in a glass of water will spread out and its color will become less intense until the glass is filled with a solution of uniform color. This sentence summarizes the idea behind the macroscopic description of diffusion. In 1855, Adolf Fick, a 25 year old professor at University of Zürich, described this process by which a population of particles is transported from regions of high concentration to regions of low concentration so as to decrease the concentration gradient. This phenomenological description is currently known as Fick's first and second laws. In the following we will explain them in the one-dimensional case as schematized in Figure 2.1 in order to focus on the guiding principle and reduce the technical details. The generalization to three dimensions is however straightforward.

#### Fick's First Law

This empirical law states that the flux,  $J(x, t)^*$ , is proportional to the spatial gradient of particle concentration  $c(x, t)^\dagger$ :

$$J(x, t) = -D \frac{\partial}{\partial x} c(x, t), \quad (2.1)$$

where  $D$  is a scalar called the diffusion coefficient. In the sequel  $D$  is considered as a constant.

#### Continuity Equation

As the number of particles in the system is conserved, another relation between  $J$  and  $c$  holds. Imagine a small rectangular volume element centered in  $x$  of left and right surface areas  $A$  and thickness  $\epsilon$  (Figure 2.1). The net influx of particles into the volume element in a small time interval  $[t, t + h]$  can be approximated by:

$$(J(x - \epsilon/2, t) - J(x + \epsilon/2, t)) Ah. \quad (2.2)$$

Similarly, the change in particle number in the same volume element is approximated as:

$$(c(x, t + h) - c(x, t)) A\epsilon. \quad (2.3)$$

If the number of particles is conserved, then the net influx must equal the increase in the number of particles in the volume element, therefore letting  $\epsilon \rightarrow 0$  and  $h \rightarrow 0$  we get:

$$\frac{\partial}{\partial x} J(x, t) = -\frac{\partial}{\partial t} c(x, t), \quad (2.4)$$

which is the continuity equation in one dimension. It links the rate of change of particle concentration at a point in space with the divergence of the local flux.

---

\*Flux is the net number of particles crossing from left to right per unit time at time  $t$  a unit area located at  $x$  perpendicular to the x-axis.

†Concentration must be understood as a number of particles per unit volume.

### Fick's Second Law

If we differentiate Eq. (2.1) with respect to  $x$  we get:

$$\frac{\partial}{\partial x} J(x, t) = -D \frac{\partial^2}{\partial x^2} c(x, t), \quad (2.5)$$

taking into account that  $D$  is constant. By combining Eq. (2.5) with Eq. (2.4) we get:

$$\frac{\partial}{\partial t} c(x, t) = D \frac{\partial^2}{\partial x^2} c(x, t), \quad (2.6)$$

which is Fick's second Law, linking the time evolution to the concentration with its spatial Laplacian.

### Solutions to Fick's Second Law

In case where the medium can be considered as homogeneous (constant  $D$ ) and infinite (no boundary condition), the evolution of the concentration of a solute in this medium can be computed easily. We set the initial condition as  $c(x, 0) = \delta(x)$ , where  $\delta(\cdot)$  is the Dirac distribution, then Eq. (2.6) admits the solution:

$$c(x, t) = \frac{1}{\sqrt{4\pi Dt}} e^{-\frac{x^2}{4Dt}}. \quad (2.7)$$

Eq. (2.7) tells us that with time the concentration spreads out as a Gaussian distribution that dilates.

Another situation that is easy to understand (the analytical derivation can be found in [126]), is the infinite time limit solution of the dye drop in a glass of water. In one dimension, if the boundaries of the glass are fixed at  $-d$  and  $+d$ , the equilibrium concentration will be the square function:  $c(x, \infty) = \frac{1}{2d} \mathbf{1}_{[-d < x < +d]}$ , with  $\mathbf{1}_{[\cdot]}$  the indicator function, taking value 1 if the statement in brackets is satisfied and 0 otherwise .

Fick's description is based on the notion of gradient, "force" that drives the diffusion process. It is well suited for describing macroscopic quantities, like concentration, during their evolution towards equilibrium. From the discussion above we see that the system is in motion as long as the gradient is non-zero. Once the equilibrium reached, the system seems to "freeze" (see glass of water). However, according to our current knowledge of molecular physics, we know that the system is definitely not inert and that it is only at the macroscopic level that things don't move.

### 2.2.2 Microscopic Description

Molecular diffusion or Brownian motion was first formally described by Einstein in 1905 [44]. It refers to the notion that any type of molecule in a fluid experiences random displacements, as, agitated by thermal energy, they collide with other particles in a chaotic way. This erratic particle motion is best described in probabilistic terms. The simplest probabilistic description for Brownian motion is the one-dimensional random walk model. As we will see,

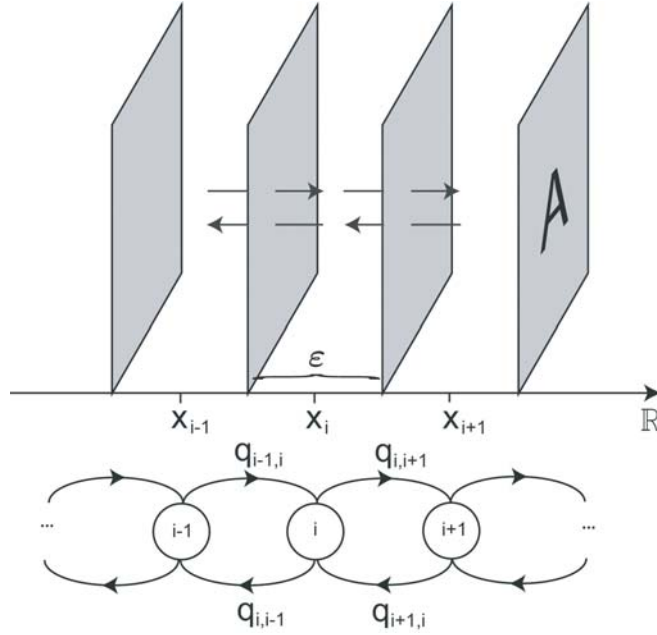


**Figure 2.1:** Particle diffusion in one dimension. The medium is virtually scattered into small rectangular volume elements centered on  $x_i$  and of side area  $A$  and thickness  $\epsilon$ . The inter-compartment particle exchange is ruled by the defined flux rates  $(q, \cdot)$ .

the microscopic description has the advantage to characterize (statistically) the behavior of each individual particle, a necessary condition for understanding diffusion MRI. It also makes no difference whether we study the evolution of a particular solute (e.g. dye) in a solution (e.g. water), or whether we look at water self-diffusion\*, situation where the notion of gradient is not evident.

Let us consider the continuous time stochastic process  $\{x(t)\}_{t \geq 0}$  with values in the set of positions  $\{x_i\}_{i \in \mathbb{Z}}$ , where  $x_i \in \mathbb{R}$ , as the random walk of a particle on the line (Figure 2.1).  $\mu(x_i, t)$  is the probability of finding the particle in  $x_i$  at time  $t$ . It can also be seen as the particle mass in volume element of side area  $A$  and thickness  $\epsilon$  centered in  $x_i$  divided by the total particle mass in the system. The exchange rules between any two neighboring compartments  $x_i$  and  $x_{i+1}$  is governed by the flux rates  $q_{i,i+1}$  and  $q_{i+1,i}$ , coefficients that can be described as the mass flux from  $x_i \rightarrow x_{i+1}$  per unit mass in  $x_i$  and from  $x_{i+1} \rightarrow x_i$  per unit mass in  $x_{i+1}$ , respectively. The first order expansion of mass evolution in compartment  $x_i$  is:

$$\begin{aligned} \mu(x_i, t+h) = & \mu(x_i, t) + h \{ q_{i-1,i} \mu(x_{i-1}, t) - q_{i,i-1} \mu(x_i, t) + \\ & + q_{i,i+1} \mu(x_{i+1}, t) - q_{i+1,i} \mu(x_i, t) \} + o(h). \end{aligned} \quad (2.8)$$

It tells us that for a small time interval  $h$ , the mass in volume element  $x_i$  at time  $t+h$  only depends on the mass in  $x_i$  and its direct neighbors at time  $t$ . We recall that  $o(h)$

\*Water molecular displacements in water due to thermal energy.



symbol represents a function defined in a neighborhood of 0 for which  $\lim_{h \rightarrow 0} \frac{|o(h)|}{h} = 0$ . It is worth to notice that in Eq. (2.8), the expression in brackets is sometimes called the weighted graph Laplacian operator applied on  $\mu$ . Reordering the terms and taking the limit when  $h \rightarrow 0$  yields:

$$\frac{\partial}{\partial t} \mu(x_i, t) = q \{ (\mu(x_{i+1}, t) - \mu(x_i, t)) - (\mu(x_i, t) - \mu(x_{i-1}, t)) \}, \quad (2.9)$$

where we have set the flux rate to a constant  $q$ , as we model presently diffusion in a homogenous and infinite medium.

In order to link this microscopic and discrete model with the continuous model of Section 2.2.1, we have to make the volume elements sufficiently small such that the continuous approximation holds. First, we redefine  $x_i \triangleq x$ ,  $x_{i-1} \triangleq x - \epsilon$  and  $x_{i+1} \triangleq x + \epsilon$  and replace it in Eq. (2.9); we get:

$$\frac{\partial}{\partial t} \mu(x, t) = q\epsilon^2 \frac{(\mu(x + \epsilon, t) - \mu(x, t)) - (\mu(x, t) - \mu(x - \epsilon, t))}{\epsilon^2}. \quad (2.10)$$

If we divide on both side of Eq. (2.10) by  $A\epsilon$  and define  $D \triangleq q\epsilon^2$  and let  $\epsilon$  be sufficiently small, we get a good approximation of Eq. (2.6).

We have seen here how the microscopic and the macroscopic description match. Depending on the context, we will choose the one or the other model. With respect to the microscopic model, the concentration  $c(x, t)$  can up to a constant be interpreted as the probability density function (PDF) of the particle random position after diffusion time  $t$  given its initial position  $x = 0$  at time  $t = 0$ .

## 2.3 Displacement of One Spin

We know from the above discussion that the three-dimensional random displacement of a single spin in a medium can be described by a PDF. Usually it does depend not only on the time interval  $\Delta$  during which displacement occurs, which we call mixing time, but also on the starting position.

Given that at time  $t = 0$  spin position is  $\mathbf{x}(0)$ , its random position  $\mathbf{x}(\Delta)$  after diffusion time  $\Delta$  is well characterized by a Gaussian PDF when the medium is homogeneous:

$$p(\mathbf{x}(\Delta)|\mathbf{x}(0)) = \frac{1}{(4\pi D\Delta)^{\frac{3}{2}}} \exp\left(-\frac{\|\mathbf{x}(\Delta) - \mathbf{x}(0)\|^2}{4D\Delta}\right). \quad (2.11)$$

The diffusion coefficient  $D$  only depends on the molecule mass, the temperature and the viscosity of the medium. For example, for pure water at a temperature of 37°C, the diffusion coefficient is equal to  $3 \times 10^{-9} \text{m}^2/\text{s}$ . In other words, for a typical mixing time used in diffusion MRI, of  $\Delta = 50 \text{ ms}$ , the characteristic length ( $l = \sqrt{6D\Delta}$ ) equals  $17 \mu\text{m}$ . In 50 ms 32% of the molecules have moved at least this distance, while only 5% have reached over  $34 \mu\text{m}$ .

As we will see further down, it is not so much the exact spin position ( $\mathbf{x}(\Delta)$  or  $\mathbf{x}(0)$ ) which is of interest in diffusion MRI but more the dynamic displacement over mixing time  $\Delta$ :  $\mathbf{r} \triangleq \mathbf{x}(\Delta) - \mathbf{x}(0)$ , so that for emphasis, we often write Eq. (2.11) as:

$$p(\mathbf{x}(0) + \mathbf{r}|\mathbf{x}(0)) = \frac{1}{(4\pi D\Delta)^{\frac{3}{2}}} \exp\left(-\frac{\|\mathbf{r}\|^2}{4D\Delta}\right). \quad (2.12)$$

For completeness we should add that, if this fluid in addition to diffusion experiences a net mean flux of velocity  $\mathbf{v}$ , the term  $\|\mathbf{r}\|$  should be replaced by  $\|\mathbf{r} - \mathbf{v}\Delta\|$  in Eq. (2.12).

It is clear that biological tissues are through their cellular organization highly compartmented and that therefore their diffusion PDFs, for the above given time-scale, are far from Gaussian [6]. Basically, we can expect  $p(\mathbf{x}(\Delta)|\mathbf{x}(0))$ , which is sometimes called the conditional propagator, to potentially take any shape as long as it is positive and of integral one. The conditional propagator describes the possible displacement of a spin, given the initial spin position is  $\mathbf{x}(0)$ .

## 2.4 Voxel Averaged Spin Displacements

In MRI a signal is never detected from one single spin but instead via a coherent superposition of signals from a very large number of molecules. Therefore the resulting signal associated to an imaging voxel is the result of a signal integration over that specific voxel, typically a box of several millimeter cube. Accordingly, we need to adopt an "ensemble averaged" view in order to depict the overall behavior.

This can be done by introducing the average propagator  $\bar{p}_\Delta(\mathbf{r})$  that is the probability distribution that describes the voxel averaged spin random dynamic displacements. In the case of absence of net translation or flux, it describes the voxel averaged diffusion process. We define it first very generally as:

$$\bar{p}_\Delta(\mathbf{r}) = \int \mathbf{1}_{[\mathbf{x}(\Delta) - \mathbf{x}(0) = \mathbf{r}]} dp(\mathbf{x}(\Delta), \mathbf{x}(0)), \quad (2.13)$$

where the Lebesgue integral is taken with respect to the joint probability measure of random position  $\mathbf{x}(\Delta)$  and  $\mathbf{x}(0)$ . This notation emphasizes the fact the average propagator captures the pair of random positions  $(\mathbf{x}(0), \mathbf{x}(\Delta))$  such that their vector distance is  $\mathbf{r}$ .

Practically, Eq. (2.13) can be expressed in the continuous case by summing, for a given dynamic displacement, the individual spin conditional propagators over an imaging voxel  $\subset \mathbb{R}^3$ :

$$\bar{p}_\Delta(\mathbf{r}) = \int_{\text{voxel}} p(\mathbf{x}(0) + \mathbf{r}|\mathbf{x}(0)) \mu(\mathbf{x}(0)) d^3\mathbf{x}(0), \quad (2.14)$$

where  $\mu$  is the normalized spin mass density:  $\int_{\text{voxel}} \mu(\mathbf{x}) d^3\mathbf{x} = 1$ ; hence also the PDF of a spin position.

While in the case of complex diffusion the average propagator captures the shape of the individual conditional propagator of various compartments; in the case of a homogenous medium the average propagator is identical to the conditional propagator, as diffusivity is the same over the voxel:

$$\bar{p}_\Delta(\mathbf{r}) = \frac{1}{(4\pi D\Delta)^{\frac{3}{2}}} \exp\left(-\frac{\|\mathbf{r}\|^2}{4D\Delta}\right). \quad (2.15)$$

Again as in Section 2.3, if there is uniform flux through the voxel, the centered Gaussian is translated away from the origin by  $\mathbf{v}\Delta$ .

## 2.5 Diffusion Anisotropy in the Brain

Biological tissues are highly heterogeneous media made of various compartments with different diffusivities. In analogy to material sciences [29] the cyto-histological architecture of living material can be seen as a porous structure made of a set of more or less connected compartments arranged in a network-like fashion. During their diffusion driven random displacements, spin movements are impeded by compartment boundaries and other molecular obstacles, such that the actual diffusion distance is reduced as compared to the unrestricted case. The particularity of neuronal tissue is its fibrillar structure made of tightly packed and coherently aligned axons, often organized in bundles. As a result the micrometric water molecular movements are hindered to a greater extent in directions perpendicular to the axonal orientation than along its parallel direction (Figure 2.2). As the diffusive properties change with direction one speaks about anisotropy.

The experimental evidence suggest that the tissular component responsible for the observed orientational anisotropy in White Matter (WM) [34] is principally the spatial organization of cellular membranes, which is modulated by the degree of myelination of the individual axons and the density of cellular packing. On the other hand, it is unlikely that, given its low velocity, axonal transport or neurofilaments play a significant role in the MRI measured anisotropy [14, 16].

In such tortuous material, the conditional propagator in the voxel space is now a PDF that is highly dependent on the initial spin position as well as the mixing time considered and accordingly its explicit description difficult to guess and impossible to measure. With respect to some simplifications, on the contrary, the global shape of the measurable average propagator is intuitive. First, let's consider a voxel traversed by a unique fiber bundle (Figure 2.2), where all axons are more or less oriented similarly; on average, over the voxel, diffusion will be more intense along the fiber direction than perpendicularly. If a voxel is traversed by say two fiber populations, one would expect for an appropriate mixing time to observe an average propagator with two orientational maxima, corresponding to both fiber orientations.

## 2.6 Diffusion Contrast

The effect of spin displacement on the NMR signal can be understood from a simple Pulsed Gradient Spin Echo (PGSE) experiment (Figure 2.3) as described by Stejskal and Tanner [138]. The purpose of these gradient pulses is to magnetically label the individual spins according to their dynamic displacements.

Let us first go through the sequence step by step. The spin system is first transversally excited with a  $\pi/2$  RF-pulse, then exposed to a first strong magnetic field gradient of duration  $\delta$ . The produced dephasing is then reverted by a  $\pi$  RF pulse and followed, at a time  $\Delta$

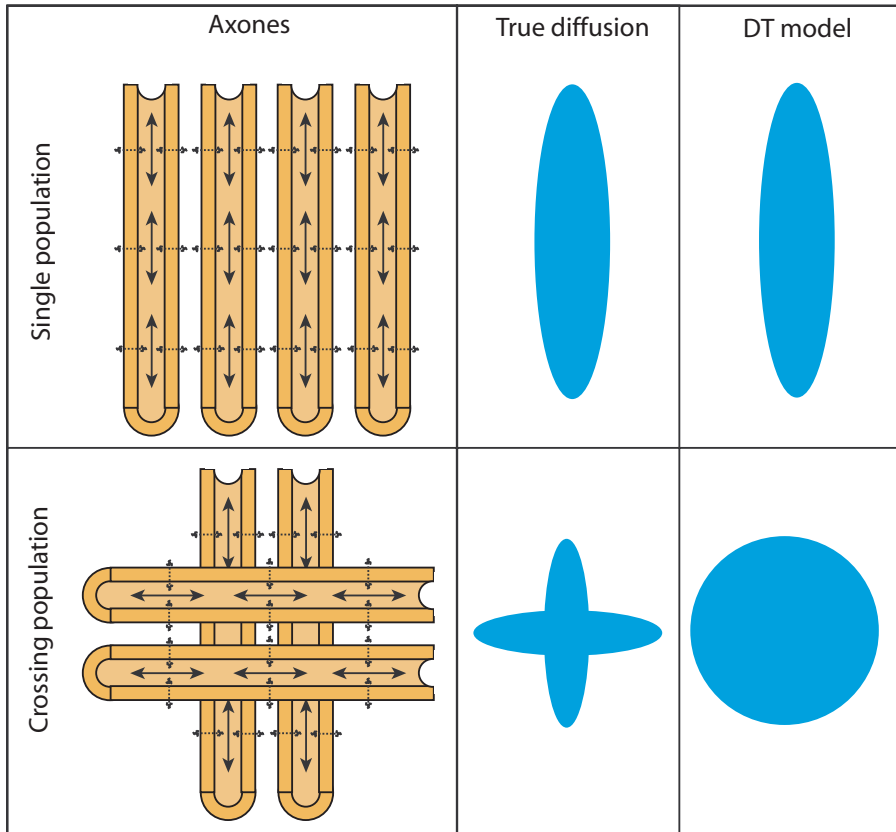


**Figure 2.2:** Relation between axonal tissue organization and average diffusion propagator. In the case of a voxel with one single fiber population, the true average propagator is a cigar shaped function, with an orientational maximum pointing in the direction of the fiber tangent. Under the diffusion tensor model, the average propagator has a similar shape as its real counterpart. When two fiber population cross, the average propagator has a cross like shape, with local maxima corresponding to fiber orientations. Under the diffusion tensor model, however, the angular contrast is lost.

after the start of the first gradient, by a second rephasing gradient of identical shape as the first one. The echo is acquired at time TE.

As readily mentioned the effect of the first diffusion gradient is to induce a phase shift,  $\phi(0)$ , of the spin transverse magnetization, which depends on the spin position  $\mathbf{x}(t)$  on labelling:

$$\phi(0) = \mathbf{q} \cdot \frac{1}{\delta} \int_0^\delta \mathbf{x}(t) dt, \quad (2.16)$$

where for convenience we define  $\mathbf{q}$  as the gradient wave vector:  $\mathbf{q} = \gamma\delta\mathbf{g}$ , with  $\gamma$  being the proton gyromagnetic ratio and assume the magnetic gradient  $\mathbf{g}$  to be constant over time  $\delta$ .

After the  $\pi$  RF pulse, which transforms  $\phi(0)$  into  $-\phi(0)$ , the second gradient pulse produces a phase shift:

$$\phi(\Delta) = \mathbf{q} \cdot \frac{1}{\delta} \int_\Delta^{\Delta+\delta} \mathbf{x}(t) dt, \quad (2.17)$$

which results in a net dephasing:

$$\phi = \phi(\Delta) - \phi(0). \quad (2.18)$$

At this stage it may be useful to assume for some instant that the duration  $\delta$  of the diffusion sensitizing gradient is negligible as compared to the mixing time  $\Delta$ . Under this narrow pulse approximation (p. 338 [29]) the relationship between dephasing and spin displacement simplifies in the following manner:

$$\phi = \mathbf{q} \cdot [\mathbf{x}(\Delta) - \mathbf{x}(0)] \quad (2.19)$$

$$= \mathbf{q} \cdot \mathbf{r}, \quad (2.20)$$

and we immediately observe that dephasing is proportional to the spin dynamic displacement.

Finally, we remember that the MR signal is a voxel averaged measure ( $\langle \cdot \rangle$ ) such that we can write diffusion contrast in the following terms:

$$S_\Delta = S_0 \langle e^{i\phi} \rangle, \quad (2.21)$$

where  $S_0$  is a constant that can be computed by the spin echo experiment without diffusion weighting and  $i \triangleq \sqrt{-1}$ .

## 2.7 Signal-Propagator Fourier Relationship

In order to improve our understanding of equation Eq. (2.21), we pursue with the narrow pulse approximation for a moment. We observe that if the voxel average is considered as an expectation  $E(\cdot)$ , then the MR signal becomes proportional to the characteristic function (p. 33 [23]) of the dynamic spin displacement vector. If we replace the dephasing by Eq. (2.20),

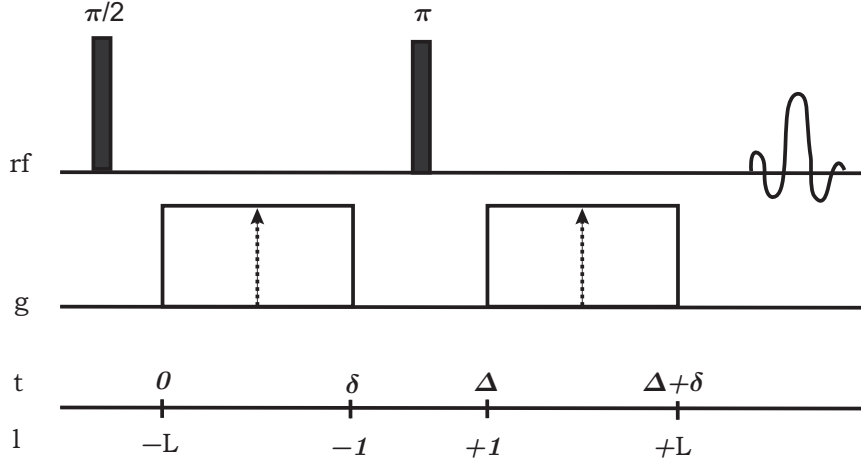


**Figure 2.3:** Pulsed Gradient Spin Echo (PGSE) experiment as described by Stejskal-Tanner [138]. The gradient amplitude is  $g$ , the pulse duration  $\delta$ , the gradient pulse spacing  $\Delta$ . A continuous time variable ( $t$ ) and a discrete time index ( $l$ ) is depicted. For the narrow pulse approximation, the gradients are represented by a pair dotted arrows, symbolizing the dirac-like function of infinitesimal duration of gradient duration and of integral  $\delta g$ .

it yields a Fourier relationship between the MR signal and the underlying density which is the previously defined average propagator,  $\bar{p}_\Delta(\mathbf{r})$ :

$$S_\Delta(\mathbf{q}) = S_0 E(e^{i\phi}) \quad (2.22)$$

$$= S_0 \int_{\mathbb{R}^3} \bar{p}_\Delta(\mathbf{r}) e^{i\mathbf{q} \cdot \mathbf{r}} d^3\mathbf{r}. \quad (2.23)$$

$\bar{p}_\Delta(\mathbf{r})$  can be regarded as the spectrum of the diffusion contrast. Accordingly we rename in the sequel  $\bar{p}_\Delta(\mathbf{r})$  the diffusion spectrum or displacement spectrum due to diffusion .

## 2.8 $\delta$ -Averaged Displacement

As just seen, the narrow pulse approximation allows us to easily understand the intrinsic Fourier relationship between the MR signal and the underlying water mobility. In practice, however, the duration  $\delta$  of the diffusion encoding gradient is no more negligible as compared to the diffusion time  $\Delta$  (i.e.  $\delta \approx \Delta$ ), so that the formalism developed above must be reexamined. Interestingly the description provided by Eq. (2.23) still remains valid with non infinitesimal diffusion encoding gradients. Nevertheless, as shown by Mitra and Halperin [110], the interpretation of the dynamic displacement vector  $\mathbf{r}$ , changes slightly and is obvious from the following expression which is derived directly from Eqs. (2.16), (2.17) and (2.20):

$$\mathbf{r} = \frac{1}{\delta} \int_{\Delta}^{\Delta+\delta} \mathbf{x}(t) dt - \frac{1}{\delta} \int_0^{\delta} \mathbf{x}(t) dt. \quad (2.24)$$

In this case  $\mathbf{r}$  must be interpreted as the  $\delta$ -averaged dynamic spin displacement. It means that  $\mathbf{r}$  describes the displacement of the spin mean position between time 0 to  $\delta$  and between time  $\Delta$  to  $\Delta + \delta$ .

In practice we see that the difference in interpretation of  $\mathbf{r}$  and its distribution  $\bar{p}_\Delta(\mathbf{r})$  for  $\delta \ll \Delta$  and  $\delta \approx \Delta$  is not very important. However we can notice from Eq. (2.24) and from Figure 2.4 that the longer the gradient encoding  $\delta$  and the shorter the mixing time  $\Delta$  the less contrasted the diffusion spectrum  $\bar{p}_\Delta(\mathbf{r})$  will be, with a consequent diminution of the fiber separation power.

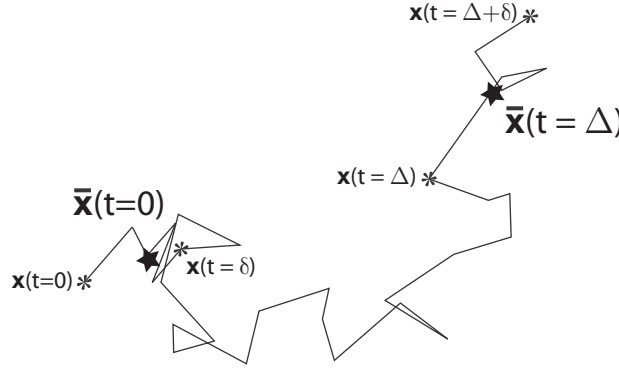


**Figure 2.4:** Random spin displacement. The black line is random spin trajectory. Its position  $\mathbf{x}(t)$  is depicted for some critical times corresponding to the beginning and end of gradient application.  $\bar{\mathbf{x}}(t=0)$  is the spin average position between time  $t=0$  and  $t=\delta$ , whereas  $\bar{\mathbf{x}}(t=\Delta)$  is the spin average position between time  $t=\Delta$  and  $t=\Delta+\delta$ .

## 2.9 Diffusion Tensor Imaging

At this stage we have sufficient elements in mind in order to draw, in a succinct manner, the principles behind scalar diffusion MRI and Diffusion Tensor MRI (DTI) (for early papers see [9, 97] and for review see [7, 98, 99, 102]). The following description is axiomatic as the reasoning is based on a list of hypotheses, which although not necessarily true are very useful conceptually. After having done some work, we will come back to the interpretation of DTI in Chapter 4 in order to better understand those hypotheses.

### 2.9.1 Imaging the ADC

Still keeping in mind the narrow pulse approximation, let us at first instance assume that the medium under study is homogeneous and experiences no net flux. Accordingly, the average propagator as well as its Fourier Transform (FT) are centered Gaussians of variance  $2D\Delta$  and  $(2D\Delta)^{-1}$  respectively. And we obtain a signal of exponential decay in the square of the gradient intensity  $\|\mathbf{q}\|^2$ :

$$S_\Delta(\mathbf{q}) = S_0 \exp(-D\Delta\|\mathbf{q}\|^2). \quad (2.25)$$

In order to account for the finite pulsed gradient duration in the Stejskal-Tanner sequence, the effective mixing time  $\Delta$  should be replaced by  $\Delta - \delta/3$  [97, 98]. It is also common usage in the MR community to put in one single variable the various imaging parameters. Accordingly, a b-factor was introduced and defined as  $b = (\Delta - \delta/3)\|\mathbf{q}\|^2$  for the Stejskal-Tanner sequence [98].

Eq. (2.25) provides a simple way to measure the diffusion coefficient as:

$$D = -b \ln \left( \frac{|S(b)|}{|S_0|} \right). \quad (2.26)$$

The careful reader will have observed that in Eq. (2.26) the signal modulus appears instead of the full complex signal. We must remember that the diffusion encoding gradients are very strong in order to capture diffusion related microscopic spin displacements. Accordingly the signal is even more sensitive to more macroscopic molecular motion that can be caused by flux, i.e. perfusion, or macroscopic sample displacement, i.e. brain pulsation and subject movements. Consequently the measured average propagator is translated away from its origin, which dephases the signal. As we know that the diffusion related signal, in the Gaussian case, is real and positive, it is sufficient to compute the diffusion coefficient from the signal modulus. We must also mention that at this stage we consider the medium isotropic, hence the direction of the gradient wave vector  $\mathbf{q}$  can be arbitrarily chosen.

It must be bared in mind that we recover from relation Eq. (2.26) the "true" diffusion coefficient, in the sense of a marker of the viscosity of the medium, only if the medium is homogeneous, hence the conditional propagator Gaussian. However, it was suggested from early biological studies, that the complicated diffusion processes that occur in living tissues at the voxel scale can be described by using the microscopic, free-diffusion model. But the physical diffusion coefficient  $D$  ought to be replaced by a global statistical parameter, the Apparent Diffusion Coefficient (ADC) [101].

### 2.9.2 Imaging the Diffusion Tensor

Along the same lines as the above ADC model, the Diffusion Tensor (DT) has emerged from a simple, yet more sophisticated, Gaussian model. It refers to concepts present in physics of liquid-crystals which is a class of materials that exhibits organizational anisotropy [18]. Proposed by Basser et al. [8], a second order symmetric and positive definite tensor is fitted to the data instead of the scalar ADC. Doing so, it is assumed that the biological restrictions to water mobility results in Gaussian but possibly anisotropic diffusion. Hence the average propagator is modified as follows:

$$\bar{p}_\Delta(\mathbf{r}) = \frac{1}{\sqrt{\det |\mathbf{D}|} (4\pi\Delta)^3} \exp \left( -\frac{\mathbf{r}^T \mathbf{D}^{-1} \mathbf{r}}{4\Delta} \right). \quad (2.27)$$

Accordingly by FT, the signal model takes the following form:

$$S_\Delta(\mathbf{q}) = S_0 \exp \left( -\Delta \mathbf{q}^T \mathbf{D} \mathbf{q} \right), \quad (2.28)$$



when  $\delta \ll \Delta$ . The DT is a symmetric  $3 \times 3$  matrix therefore has 6 unique coefficients [11]. Consequently, at least 7 image acquisitions are necessary to reconstruct the diffusion tensor:  $N \geq 6$  diffusion weighted images,  $S(\mathbf{q})$ , of various gradient orientation — ideally uniformly distributed over a sphere of radius  $|\mathbf{q}|$  — and one to obtain the unattenuated reference image ( $S_0$ ). The tensor elements can then be estimated by linear regression as follows:

$$\mathbf{d} = (\mathbf{U}^T \mathbf{U})^{-1} \mathbf{U}^T \mathbf{s}, \quad (2.29)$$

where  $\mathbf{d} \triangleq [d_{11}, d_{12}, \dots, d_{33}]^T$  is the vector containing the tensor components,  $\mathbf{s}$  the weighted signal logarithm:

$$\mathbf{s} \triangleq -b \ln \begin{bmatrix} S(\mathbf{q}_1)/S_0 \\ \vdots \\ S(\mathbf{q}_N)/S_0 \end{bmatrix}, \quad (2.30)$$

and  $\mathbf{U}$  the gradient direction matrix:

$$\mathbf{U} \triangleq \begin{bmatrix} u_1^1 u_1^1 & u_1^1 u_1^2 & \dots & u_1^3 u_1^3 \\ u_2^1 u_2^1 & u_2^1 u_2^2 & \dots & u_2^3 u_2^3 \\ \vdots & \vdots & \ddots & \vdots \\ u_N^1 u_N^1 & u_N^1 u_N^2 & \dots & u_N^3 u_N^3 \end{bmatrix}, \quad (2.31)$$

with  $[u^1 u^2 u^3]^T \triangleq \mathbf{q}/\|\mathbf{q}\|$ .

The reconstructed DT image can be represented as a plot of fuzz balls where each surface corresponds to the set of points such that:  $\mathbf{u}^T \mathbf{D} \mathbf{u}$ , with  $\mathbf{u}$  defined on the unit sphere (Figure 2.5).

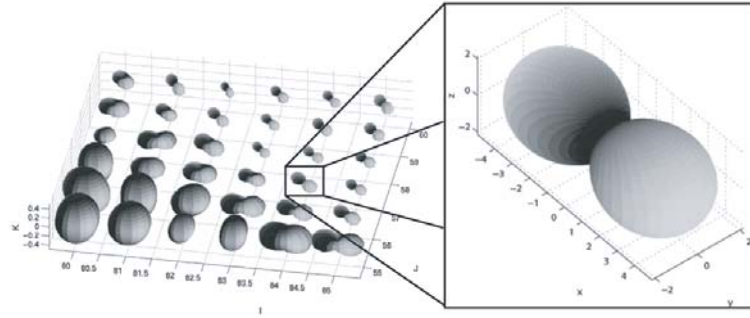


**Figure 2.5:** Map of fuzz balls. Each DT in a voxel is represented as a polar plot. Regions of isotropic diffusion have ball like shapes, while anisotropic regions display peanut like shapes, oriented along the fiber tracts.

### 2.9.3 Mean Diffusion, Fractional Anisotropy and Diffusion Color Maps

Depending on the context, displaying the DT as a three-dimensional polar plot, is not always the most informative and practical visualization. Therefore various rotationally invariant

scalar measures have been developed for the DT. They have the advantage to be represented as gray level images, which, in the perspective of cohort studies, allow univariate statistical analysis. The two most commonly used are mean diffusion ( $\langle D \rangle$ ) and Fractional Anisotropy (FA) [10].

Mean diffusion can simply be computed by taking the normalized trace of the DT:

$$\langle D \rangle = \frac{1}{3} \text{Trace}(\mathbf{D}). \quad (2.32)$$

In practice it has the same meaning as averaging the ADC that has been computed over several gradient directions.

FA measures the deviation of  $\mathbf{D}$  from the equivalent isotropic tensor  $\langle D \rangle \mathbf{I}$ , where  $\mathbf{I}$  is the identity matrix. It can be expressed in terms of the eigenvalues  $\{\lambda_i\}$  of  $\mathbf{D}$ :

$$FA = \sqrt{\frac{3}{2}} \sqrt{\frac{\sum_i (\lambda_i - \langle \lambda \rangle)^2}{\sum_i \lambda_i^2}}, \quad (2.33)$$

where  $\langle \lambda \rangle$  is the average over all eigenvalues. This measure is such that in brain areas where fibers are coherently aligned, its value will be high as  $\mathbf{D}$  will be cigar shaped, while in regions of distributed fiber orientations or in the ventricles, its value will be close to zero.

Finally the FA maps can be color coded by using the orientation of the principal eigenvector  $\mathbf{e}_1$  of  $\mathbf{D}$ . The vectorial RGB channel  $\mathbf{v}_{RGB}$  is then expressed as:  $\mathbf{v}_{RGB} = FA \mathbf{e}_1$  [120].

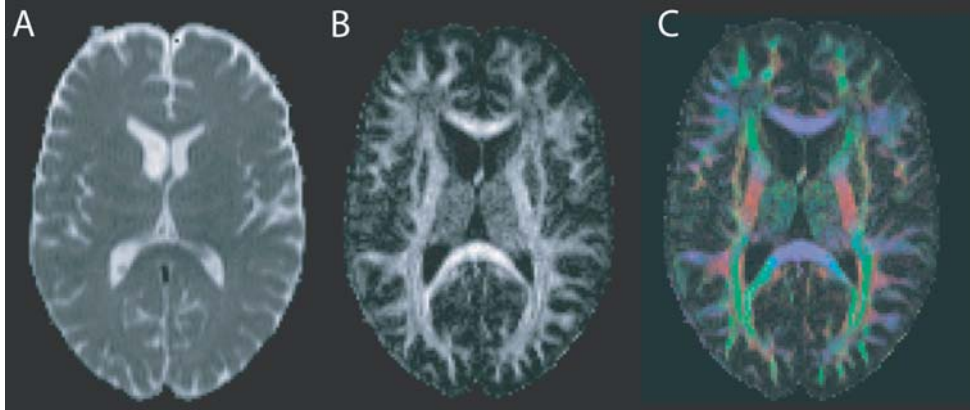


**Figure 2.6:** Visualizing DTI on an axial brain slice. A) mean diffusion map, B) fractional anisotropy, C) color map, where green codes for fronto-occipital, blue for transverse and red for cranio-caudal main diffusion axis.

---

# Why Diffusion Contrast is Positive

---

# 3

*Everything should be made as simple as possible, but not simpler.*

A. Einstein

## 3.1 Introduction

Diffusion MRI techniques base their reconstruction on the modulus of the MR signal, as in practice phase is polluted by macroscopic displacements. We have seen in Chapter 2 that in the case of DT- MRI this short cut is admissible because the resulting signal of assumed Gaussian diffusion is real and positive. This result is straightforward and follows from the Fourier duality between the diffusion spectrum and the diffusion encoded MR signal. Novel diffusion imaging techniques — like Diffusion Spectrum MRI [160] which will be presented and discussed in Chapter 4 and others like q-ball [151] and PAS [82] — aim at measuring general diffusion phenomena in biological samples, where diffusion is clearly restricted. Accordingly, there is no more obvious guaranty for diffusion contrast ( $S_{\Delta}(\mathbf{q})$ ) to be positive. There is therefore a compelling necessity to better understand the signal generation and the condition under which it might be possible to reconstruct the diffusion spectrum ( $\bar{p}_{\Delta}(\mathbf{r})$ ) using the only signal modulus. In the present work we want to show how diffusion can be modeled by a Markov process on a network and how it exposes the essential features of diffusion that allows us to understand why, even in the general case, the diffusion encoded signal is real and positive.

## 3.2 Positivity Under the Narrow Pulse Approximation

### 3.2.1 Problem Formulation

In order to draw an accurate model of spin displacement in a voxel of biological tissue, let us first consider several general properties of our system, which will actually serve as starting hypothesis. First, we consider that spin motion is caused purely by diffusion such that there is no net flux across or within the voxel. Indeed, in a tissue that is not directly perfused, net fluxes are probably too slow to be relevant compared to the current imaging time scales that are in the order of tens of milliseconds. Second, we look at the voxel as an isolated system. Indeed, spin displacements are upper bounded by the free water diffusion case. Therefore, the mass that can transfer from one voxel to another during the experimental mixing time is no more than a few percent of the total voxel mass, influencing proportionally the MR signal. Finally, we admit that the system properties remain constant for the considered experimental time intervals (e.g. local diffusion coefficients and compartment sizes do not change during the acquisition time  $\Delta$ ).

The narrow pulse approximation as described in Section 2.6 is a nice way to begin our analysis, since it yields a simple Fourier relationship between signal and diffusion spectrum (Eq. (2.23)). Hence we need to show that:

*In a closed system, the Fourier transform of a displacement spectrum due to a homogeneous diffusion process in the stationary state is **real** and **positive**.*

We decide to model water diffusion in a voxel by the random walk of spins on a finite network, where the  $N$  vertices correspond to a sufficient number of compartments and the edges to the connection between them. First, we assume that there exists a path from any compartment to any other compartment (there is no isolated sub-network; we say that the network is irreducible). Next we assume that at equilibrium there is no net flow between any two compartments as the system is only driven by diffusion.

We build the network with a complete directed graph of order  $N$  and associate to every vertex  $i$ :

- a position vector  $\mathbf{x}_i \in \text{voxel} \subset \mathbb{R}^3$ ,
- a spin mass or number  $\mu_i(t)$ , which we define without loss of generality to be normalized:  $\sum_i \mu_i(t) = 1$  for all  $t \in \mathbb{R}^+$ .

To each edge  $i \rightarrow j$ , we associate a weight  $q_{ij}$  which can be considered as the average mass transfer from compartment  $i$  to compartment  $j$  per unit time and per unit mass in  $i$  (or simply flux rate from  $i$  to  $j$ ). The matrix  $\mathbf{Q} \triangleq (q_{ij})_{ij}$  is a set of numbers that fully characterizes the system properties by incorporating all the effects influencing spin transfer, like local diffusion coefficients, local compartment volumes and geometries.

Let the stochastic process  $\{\mathbf{x}(t)\}_{t \geq 0}$  with values in  $\{\mathbf{x}_1, \dots, \mathbf{x}_N\}$ , be a random walk of a particle on that network.

### 3.2.2 The Diffusion Process as a Markov Chain

In the Markov Chain (MC) formalism (Chapter 8 in [23]), the stochastic process  $\{\mathbf{x}(t)\}_{t>0}$  can be understood as a regular jump continuous-time homogeneous MC of finite state space. Accordingly, the mass distribution vector,  $\boldsymbol{\mu}(t) \triangleq [\mu_1(t), \dots, \mu_N(t)]^T$  becomes the distribution of the MC, whereas the flux rate matrix  $\mathbf{Q}$  becomes its infinitesimal generator. The diffusion process is guided by a system of differential equations that is expressed in the MC context by the Kolmogorov's differential system (p. 338, 342 [23]). Its solution shows that the transition matrix  $\mathbf{P}_t$  can be expressed in terms of  $\mathbf{Q}$ :

$$\mathbf{P}_t = e^{t\mathbf{Q}}. \quad (3.1)$$

$\{\mathbf{P}_t\}_{t>0}$  is called the transition semigroup of the chain and, in our case, it corresponds to the family of operators that drive the diffusion process. In other words,  $\mathbf{P}_t$  is responsible for the evolution of the mass distribution vector  $\boldsymbol{\mu}(s)$  along the time:

$$\boldsymbol{\mu}^T(s+t) = \boldsymbol{\mu}^T(s)\mathbf{P}_t, \text{ with } t, s \in \mathbb{R}^+. \quad (3.2)$$

From the problem formulation we see that this MC is irreducible and ergodic (p. 357 [23]). It admits a unique stationary distribution  $\boldsymbol{\pi}$  (p. 360 [23]). Moreover, as we study a pure diffusion process at equilibrium there must be no net flow. In MC terminology, it means that the stationary distribution must satisfy the detailed balance equations, i.e.  $\pi_i q_{ij} = \pi_j q_{ji}$ . Interestingly, this relation can be expressed in matrix form by saying that  $\mathbf{Q}$  has a similar matrix  $\tilde{\mathbf{Q}}$  that is symmetric:

$$\mathbf{Q} = \boldsymbol{\Pi}^{-\frac{1}{2}} \tilde{\mathbf{Q}} \boldsymbol{\Pi}^{\frac{1}{2}}, \quad (3.3)$$

where  $\boldsymbol{\Pi} \triangleq \text{diag}\{\pi_1, \dots, \pi_N\}$ . Similar matrices have identical eigenvalues (p. 44 [77]) and symmetric matrices have real eigenvalues (p. 170 [77]). Therefore  $\mathbf{Q}$  and  $\tilde{\mathbf{Q}}$  have identical and *real eigenvalues*:  $\boldsymbol{\Lambda} \triangleq \text{diag}\{\lambda_1, \dots, \lambda_N\}$ . If  $\tilde{\mathbf{Q}}$  admits the eigen-decomposition:

$$\tilde{\mathbf{Q}} = \mathbf{V} \boldsymbol{\Lambda} \mathbf{U}^T, \quad (3.4)$$

then  $\mathbf{Q}$  can be written as:

$$\mathbf{Q} = (\boldsymbol{\Pi}^{-\frac{1}{2}} \mathbf{V}) \boldsymbol{\Lambda} (\boldsymbol{\Pi}^{\frac{1}{2}} \mathbf{U})^T, \quad (3.5)$$

where  $\boldsymbol{\Pi}^{-\frac{1}{2}} \mathbf{V}$  and  $\boldsymbol{\Pi}^{\frac{1}{2}} \mathbf{U}$  are respectively left and right eigenvector matrices of  $\mathbf{Q}$ . By replacing  $\mathbf{Q}$  by Eq. (3.5), Eq. (3.1) can be expressed as:

$$\mathbf{P}_t = \boldsymbol{\Pi}^{-\frac{1}{2}} e^{t\tilde{\mathbf{Q}}} \boldsymbol{\Pi}^{\frac{1}{2}}. \quad (3.6)$$

### 3.2.3 The Fourier Transform of the Diffusion Spectrum

Lets define the displacement spectrum over the network  $\bar{p}_t(\mathbf{r})$  as the probability for a spin in the network to experience a relative vector displacement  $\mathbf{r}$  for a diffusion time  $t$ . If  $\mathbf{x}(0)$  and  $\mathbf{x}(t)$  are the random variables that define the positions of an individual spin at time 0 and time  $t$ , respectively, then we can write:

$$\bar{p}_t(\mathbf{r}_k) = \sum_{i,j: \mathbf{x}_j - \mathbf{x}_i = \mathbf{r}_k} M_{ii} P_{ij}, \quad (3.7)$$

with  $(M_{ij})_{ij} \triangleq \mathbf{M} \triangleq \text{diag}\{\mu_1(t), \dots, \mu_N(t)\}$  and  $(P_{ij})_{ij} \triangleq \mathbf{P}_t$ . In other words, the sum over the joint distribution  $p(\mathbf{x}(t) = \mathbf{x}_j, \mathbf{x}(0) = \mathbf{x}_i) = M_{ii} P_{ij}$  is restricted to the displacements such that:  $\mathbf{x}(t) - \mathbf{x}(0) = \mathbf{r}_k$ .

It remains to take the Fourier Transform (FT) of the diffusion spectrum:

$$\Psi(\mathbf{q}) = \sum_k \bar{p}_t(\mathbf{r}_k) e^{i\mathbf{q} \cdot \mathbf{r}_k} \quad (3.8)$$

$$= \sum_{i,j} M_{ii} P_{ij} e^{i\mathbf{q} \cdot (\mathbf{x}_j - \mathbf{x}_i)} \quad (3.9)$$

$$= \mathbf{f}_q^* (\mathbf{M} \mathbf{P}_t) \mathbf{f}_q, \quad (3.10)$$

where the effect of the spatial Fourier encoding on the network is represented by the  $N$ -dimensional vector  $\mathbf{f}_q = [e^{i\mathbf{q} \cdot \mathbf{x}_1}, \dots, e^{i\mathbf{q} \cdot \mathbf{x}_N}]^T$  and its Hermitian  $\mathbf{f}_q^*$ . Substituting  $\mathbf{P}_t$  in Eq. (3.10) by Eq. (3.6) yields:

$$\Psi(\mathbf{q}) = \mathbf{f}_q^* (\mathbf{M} \mathbf{\Pi}^{-\frac{1}{2}} e^{t\tilde{\mathbf{Q}}} \mathbf{\Pi}^{\frac{1}{2}}) \mathbf{f}_q. \quad (3.11)$$

If we place our selves in *stationary state*,  $\mathbf{M} = \mathbf{\Pi}$  and therefore Eq. (3.11) simplifies as follows:

$$\Psi(\mathbf{q}) = (\mathbf{f}_q^* \mathbf{\Pi}^{\frac{1}{2}}) e^{t\tilde{\mathbf{Q}}} (\mathbf{\Pi}^{\frac{1}{2}} \mathbf{f}_q) \quad (3.12)$$

$$= \mathbf{u}_q^* e^{t\tilde{\mathbf{Q}}} \mathbf{u}_q, \quad (3.13)$$

where  $\mathbf{u}_q \triangleq \mathbf{\Pi}^{\frac{1}{2}} \mathbf{f}_q$ .

As the eigenvalues of  $\tilde{\mathbf{Q}}$  are real, by the spectral mapping theorem (p. 36, 300 [77] or p. 381 [94]) those of  $e^{t\tilde{\mathbf{Q}}}$  are real and positive, therefore:

$$\mathbf{u}^* e^{t\tilde{\mathbf{Q}}} \mathbf{u} > 0, \text{ for all } \mathbf{u} \in \mathbb{C}^N \setminus \{0\} \text{ and for all } t \in \mathbb{R}, \quad (3.14)$$

completing the proof.  $\square$

### 3.3 Finite Duration Diffusion Encoding

As mentioned in Chapter 2, the diffusion gradient pulses in the Stejskal-Tanner experiment are indeed of finite duration. Therefore we must verify that even in this case the MR signal is guaranteed to be positive. The framework remains the same as in Section 3.2, which means that the system is characterized by an isolated system homogenous diffusion process in stationary state. We note that the MR signal can be seen as proportional to the expected value of the dephasing due to spin motion (Eq. (2.22)). However, the phase is

no more proportional to the dot product between the q-wave vector and the relative spin displacement. Thus we need to consider the original expression deduced from Eqs. (2.16), (2.17) and (2.18):

$$\phi = \mathbf{q} \cdot \frac{1}{\delta} \left[ \int_{\Delta}^{\Delta+\delta} \mathbf{x}(t) dt - \int_0^{\delta} \mathbf{x}(t) dt \right]. \quad (3.15)$$

We use the formalism developed by Caprihan et al. [31], where Eq. (3.15) is written as a function of a multiplet of infinitesimal narrow pulses. Time is discretized regularly at intervals  $\xi = \frac{\Delta+\delta}{2L}$  and indexed by  $l \in \{-L, -L+1, \dots, L\}$ , where  $-L$  and  $-1$  are respectively the times at the beginning and end of the first diffusion gradient; 0 corresponds to the time of the  $\pi$  RF-pulse;  $+1$  and  $+L$  respectively to the beginning and end of the second diffusion gradient (Figure 2.3). Without loss of generality, it yields a simple expression when two identical rectangular gradient pulses are used:

$$\phi = \mathbf{q} \cdot \sum_{l=-L}^L a_l \mathbf{x}(l) \quad (3.16)$$

with  $a_l = -a_{-l}$  and  $a_0 = 0$ .

Mathematically, we can consider  $\{\mathbf{x}(l)\}_{-L \leq l \leq L}$  to be the embedded discrete MC of the diffusion process  $\{\mathbf{x}(t)\}_{t>0}$  described in Section 3.2. It has transition matrix  $\mathbf{P}_\xi$  and is reversible as it satisfies the detailed balance equations (p. 362 [23]). In this context each  $\mathbf{x}(l)$  is a random variable defined on the set of the network vertices and represents the position of the random walk at time index  $l$ . We call  $\sum_{l=-L}^L a_l \mathbf{x}(l)$  with  $a_l = -a_{-l}$  and  $a_0 = 0$  a **bipolar balanced random sum**.

In order to convince ourself that the MR signal is real and positive, even with finite duration gradient pulses. We must verify that:

*For a reversible discrete homogenous MC  $\{\mathbf{x}(l)\}_{-L \leq l \leq L}$  of positive transition matrix  $\mathbf{P}_\xi$  and in stationary state, the function:*

$$\Psi(\mathbf{q}) = E \left( e^{i\mathbf{q} \cdot \sum_{l=-L}^L a_l \mathbf{x}(l)} \right), \quad (3.17)$$

*where  $a_l = -a_{-l}$  and  $a_0 = 0$  is **real** and **positive** for all  $\mathbf{q} \in \mathbb{R}^3$ .*

We start with the function defined in (3.17). For notational simplicity we choose  $a_l = -a_{-l} = 1$ . The MC is in stationary state and is reversible (p. 81 [23]), therefore it is possible to express  $\Psi(\mathbf{q})$  as the expectation of the product of two conditional expectations\* by time reversal of the first half of the MC. We have:

$$\Psi(\mathbf{q}) = E \left( e^{i\mathbf{q} \cdot \sum_{l=-L}^L a_l \mathbf{x}(l)} \right) \quad (3.18)$$

$$= E \left( E \left( e^{-i\mathbf{q} \cdot \sum_{l=-L}^{-1} \mathbf{x}(l)} \middle| \mathbf{x}(-1) \right) E \left( e^{i\mathbf{q} \cdot \sum_{l=1}^L \mathbf{x}(l)} \middle| \mathbf{x}(1) \right) \right), \quad (3.19)$$

---

\* For two random variables  $A$  and  $B$  the conditional expectation  $E(A|B = b)$  is the value of the expectation of  $A$  knowing that  $B$  takes the value  $b$ .

where the outer expectation is taken with respect to the joint distribution  $p(\mathbf{x}(1), \mathbf{x}(-1))$ .

By analogy with Section 3.2, we redefine a  $N$ -dimensional vector  $\mathbf{f}_q = [f_1, \dots, f_N]^T$  such that:

$$f_j = E \left( e^{i\mathbf{q} \cdot \sum_{l=1}^L \mathbf{x}(l)} \middle| \mathbf{x}(1) = \mathbf{x}_j \right). \quad (3.20)$$

$f_j$  represents the value, which the second conditional expectation of (3.19) takes knowing that the value of the chain at time  $l = 1$  is  $\mathbf{x}_j$ . It remains to express the Hermitian vector  $\mathbf{f}_q^* = [\bar{f}_1, \dots, \bar{f}_N]$  in terms of the values of the first conditional expectation of (3.19). This is possible because the forward half chain  $\{\mathbf{x}(l)\}_{1 \leq l \leq L}$  given  $\mathbf{x}_1$  is equally distributed as the backward half chain  $\{\mathbf{x}(-l)\}_{-L \geq -l \geq -1}$  given  $\mathbf{x}_{-1}$ . Thus we have:

$$\begin{aligned} \bar{f}_i &= E \left( e^{-i\mathbf{q} \cdot \sum_{l=1}^L \mathbf{x}(l)} \middle| \mathbf{x}(1) = \mathbf{x}_i \right) \\ &= E \left( e^{-i\mathbf{q} \cdot \sum_{l=-L}^{-1} \mathbf{x}(l)} \middle| \mathbf{x}(-1) = \mathbf{x}_i \right). \end{aligned} \quad (3.21)$$

We can rewrite (3.19) in matrix form by using the newly defined vectors  $\mathbf{f}_q$  and  $\mathbf{f}_q^*$ . We remember that, *in stationary state*, the joint distribution  $p(\mathbf{x}(1) = \mathbf{x}_j, \mathbf{x}(-1) = \mathbf{x}_i) = \Pi_{ii} P_{ij}$ , where  $P_{ij} \triangleq (\mathbf{P}_{2\xi})_{ij}$  hence:

$$\Psi(\mathbf{q}) = \mathbf{f}_q^* (\mathbf{\Pi} \mathbf{P}_{2\xi}) \mathbf{f}_q \quad (3.22)$$

$$= (\mathbf{f}_q^* \mathbf{\Pi}^{\frac{1}{2}}) e^{2\xi \tilde{\mathbf{Q}}} (\mathbf{\Pi}^{\frac{1}{2}} \mathbf{f}_q), \quad (3.23)$$

by using the same substitution as in Section 3.2.3. It follows that:

$$\Psi(\mathbf{q}) > 0 \quad (3.24)$$

since we have seen in Section 3.2.3 that  $e^{2\xi \tilde{\mathbf{Q}}}$  is a positive operator.  $\square$

### 3.4 Conclusions

The positivity of the displacement spectrum FT of general diffusion processes described above generalizes familiar facts. If diffusion is homogeneous and unrestricted, i.e. Gaussian, its FT is positive. If diffusion is restricted and fully evolved, then its displacement spectrum tends to the autocorrelation of the restriction geometry [29] — a function whose FT again is positive. The present approach encompasses the general situation expected in vivo in which microenvironments of distinct anisotropic diffusivities exchange spins across a continuum of timescales. Accordingly, diffusion imaging in complex and restricted samples can be performed safely using only the signal modulus, while keeping in mind the quite weak assumptions mentioned. Although these constraints should be respected in most voxels of the current in-vivo diffusion experiments, the preconditions of positivity may be violated. Indeed, spin flux related for example to perfusion [98] or virtual flux produced by inhomogeneous relaxation as well as significant asymmetric mass exchange at voxel boundaries, possibly occurring with very high resolution imaging (e.g. sub-millimetric voxel model of



Liu et al. [104]), could induce a phase-shift but only if such processes have sufficient spatial coherence to produce significant net orientational asymmetry at the scale of one voxel.

The developed framework provides not only useful safeguards with respect to imaging but also a simple tool for simulation. In this sense it highlights how the positivity of the diffusion encoded signal is uniquely determined by a flux rate matrix  $\mathbf{Q}$  that must only satisfy the detailed balance equations as we want to study a pure diffusion process. In order to avoid a common pitfall, it is worthwhile to notice that the stationary mass distribution is fully determined by  $\mathbf{Q}$ . Consequently, when performing diffusion simulation it is necessary to start the system in stationary state. If this is not the case, the simulation may measure potential phase terms due to mass flux within the system as it moves toward mass equilibrium. In other words, the equilibrium mass distribution is not achieved simply by putting a constant mass at each unit volume in a simulation. The equilibrium mass distribution is in fact a consequence of the diffusion process. Finally, modelling diffusion on an abstract graph, in our view, provides greater clarity of formulation than traditional approaches based on infinitesimal calculus, where detailed assumptions about microscopic boundary conditions may be difficult to understand and justify in relation to biological systems.



---

# Diffusion Spectrum Magnetic Resonance Imaging

---

# 4

*There is no quality in this world that is not what it is merely by contrast. Nothing exists in itself.*

H. Melville

## 4.1 Introduction

In the past decade, magnetic resonance imaging methods have been developed that by mapping the Diffusion Tensor of tissue water can nondestructively map the structural anisotropy of fibrous tissues in living systems (see Chapter 2 or for example [100]). These methods have been used to elucidate fiber architecture and functional dynamics of the myocardium [148, 149] and of skeletal muscle [159], and used in the nervous system to identify and map the trajectories of neural white matter tracts and infer neuroanatomic connectivity (see Chapter 5 or for example [113]).

Notwithstanding this progress, the DT paradigm has notable limitations. Because MRI spatial resolution typically is far in excess of the diffusion scale, each voxel represents many distinct diffusional environments, a complex signal which is in general under-specified by the six degrees of freedom of the DT (Figure 2.2). An example of particular interest occurs when a tissue has a composite fiber structure, so that each small region may contain fibers of multiple orientations corresponding to distinct diffusion anisotropies [163]. Here we describe an MRI methodology first presented by Wedeen et al. [160], called Diffusion Spectrum Imaging (DSI) that affords the capacity to resolve intra-voxel heterogeneity of diffusion by measuring diffusion spectra.

## 4.2 Theory

We remember from Section 2.6 that a classical Stejskal-Tanner experiment (Figure 2.3) [138] allows the phase-encoding of spin displacements, making the MR signal proportional to the voxel average spin dephasing. With the narrow pulse approximation, introduced in Section 2.7, we get a simple Fourier relationship (Eq. (2.23)), that we recall here, between signal ( $S_\Delta(\mathbf{q})$ ) and displacement spectrum ( $\bar{p}_\Delta(\mathbf{r})$ ):

$$S_\Delta(\mathbf{q}) = S_0 \int_{\mathbb{R}^3} \bar{p}_\Delta(\mathbf{r}) e^{i\mathbf{q} \cdot \mathbf{r}} d^3\mathbf{r}.$$

As we have seen in Section 2.4,  $\bar{p}_\Delta(\mathbf{r}) d^3\mathbf{r}$  can be interpreted as a measure of the probability for a spin in a considered voxel to make during the experimental mixing time  $\Delta$  a vector displacement  $\mathbf{r}$ , which in the absence of net translation or flow describes the voxel averaged diffusion process.

Practically, to exclude phase shifts arising from tissue motion, diffusion spectra are reconstructed by taking the Fourier Transform (FT) of the modulus of the complex MR signal:

$$\bar{p}_\Delta(\mathbf{r}) = |S_0|^{-1} (2\pi)^{-3} \int_{\mathbb{R}^3} |S_\Delta(\mathbf{q})| e^{-i\mathbf{q} \cdot \mathbf{r}} d^3\mathbf{q}. \quad (4.1)$$

Significantly, this modulus is precisely the information required to reconstruct the diffusion spectra, as the FT of displacement spectra due to diffusion are real and positive (see Chapter 3). This statement is not necessarily true but verified when spin motion is caused by pure diffusion in an isolated system of time invariant properties, conditions that are well suited to our problem.

The narrow pulse approximation is a useful simplification in order to introduce the Fourier duality between signal and spin displacement spectrum. In practice, however, we remember from Section 2.8 that the duration  $\delta$  of the diffusion encoding gradient is no more negligible as compared to the diffusion time  $\Delta$  (i.e.  $\delta \approx \Delta$ ), so that rigorously  $\mathbf{r}$  is actually the  $\delta$ -averaged relative spin displacement, detail that does not significantly change the interpretation of the imaging method, as the only consequence is a displacement distance underestimation (Figure 2.4).

## 4.3 Methods

Data were acquired on two healthy volunteers with two different systems. The first data set, centered on the brainstem only, was acquired on a 3T Allegra system from Siemens, using a single-shot EPI MRI acquisition. The spin-echo pulse sequence was augmented by diffusion encoding gradient pulses and incorporating two  $\pi$  RF pulses to minimize effects of eddy currents [128].  $TR$  and  $TE$  used were respectively 3000 and 154 ms. The second data set, a whole brain study, was acquired on a 3T Intera system from Philipps using the standard Stejskal-Tanner pulsed gradient spin-echo sequence and a  $TR$  of 3000 and a  $TE$  of 100 ms.

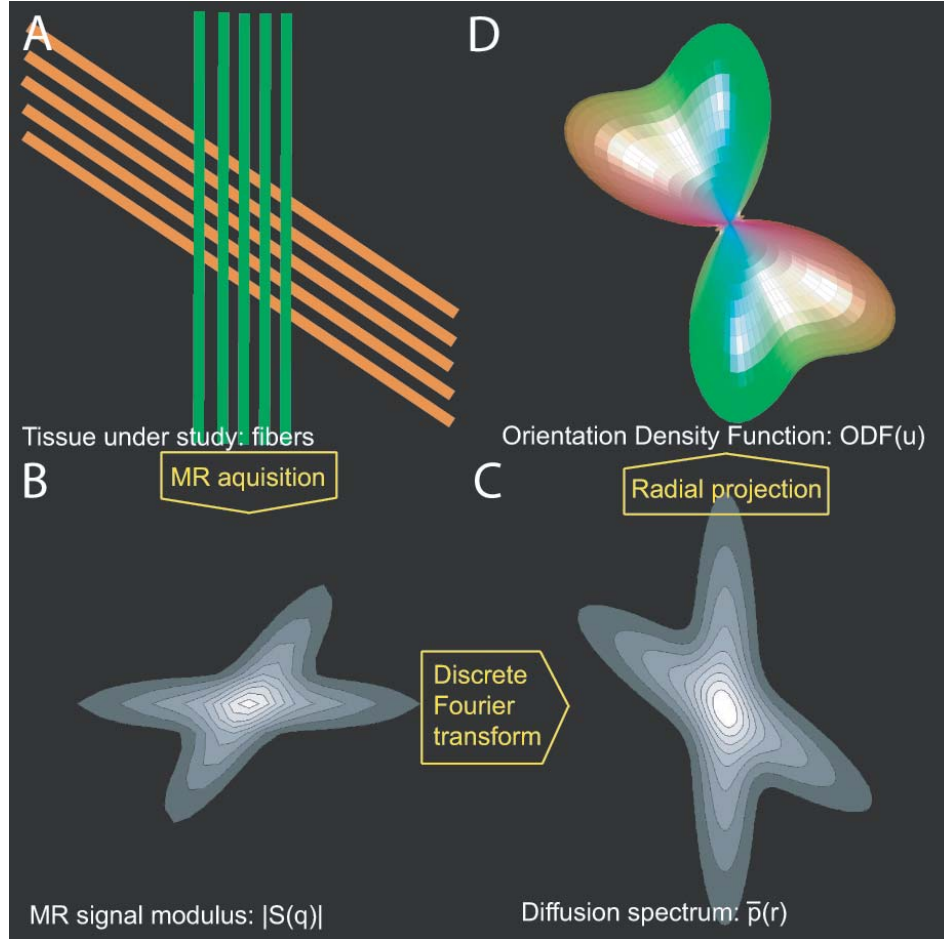


**Figure 4.1:** DSI reconstruction scheme. (A) We consider the tissue in a voxel under study. Here the tissue is represented by two populations of fibers that cross. (B) Through the MR acquisition scheme the signal  $|S_{\Delta}(\mathbf{q})|$  is sampled. (C) In order to reconstruct the diffusion spectrum, the 3D discrete FT is taken. (D) To simplify the representation of an imaging slice, the angular structure of diffusion is represented as a polar plot of the radial projection (ODF).

At each location, diffusion-weighted images were acquired for  $N = 515$  values of  $\mathbf{q}$ -encoding, comprising in  $\mathbf{q}$ -space the points of a cubic lattice within the sphere of 5 lattice units in radius (Figure 4.1B).

$$\mathbf{q} = a\mathbf{q}_x + b\mathbf{q}_y + c\mathbf{q}_z, \quad (4.2)$$

with  $a, b, c$  integers and  $\sqrt{a^2 + b^2 + c^2} \leq 5$ .  $\mathbf{q}_x, \mathbf{q}_y$  and  $\mathbf{q}_z$  denote the unit phase modulations in the respective coordinate directions (keyhole ref.). For the first data set, with gradient pulses of peak intensity  $g_{\max} = 40$  mT/m and net duration  $\delta = 60$  ms, these gradients encode diffusion spectra with isotropic resolution  $r_{\min} = 10\mu\text{m}$  and field-of-view  $r_{\max} = 50\mu\text{m}$ . This encoding produces a peak diffusion sensitivity  $b_{\max} = 1.7 \cdot 10^4$  s/mm<sup>2</sup> given an experimental mixing time  $\Delta = 66$  ms. The voxel spatial resolution was  $4 \times 4 \times 4$  mm<sup>3</sup>. For the second data set, made of 32 axial slices of resolution  $128 \times 128$  with voxels of  $2 \times 2 \times 3$  mm<sup>3</sup>, was acquired with a peak intensity diffusion gradient of 70 mT/m and a duration of  $\delta = 35$  ms, thus achieving with a mixing time of  $\Delta = 47.6$  ms a  $b_{\max} = 1.2 \cdot 10^4$  s/mm<sup>2</sup>.

The diffusion spectrum was then reconstructed by taking the discrete 3D FT of the signal modulus (Figure 4.1C). The signal is pre-multiplied by a Hanning window before the FT in order to ensure a smooth attenuation of the signal at high  $|\mathbf{q}|$  values.

As we are mainly interested in the angular structure of the diffusion spectrum, we further simplified the data by taking a weighted radial summation of  $\bar{p}_{\Delta}(\mathbf{r})$ :

$$\text{ODF}(\mathbf{u}) = Z^{-1} \int_{\mathbb{R}^+} \bar{p}_{\Delta}(\rho\mathbf{u}) \rho^2 d\rho, \quad (4.3)$$

with  $\|\mathbf{u}\| = 1$  and  $Z$  a normalization constant. It defines the Orientation Density Function (ODF), a function that measures the quantity of diffusion in direction of the unit vector  $\mathbf{u}$  (Figure 4.1D).

## 4.4 Results

Diffusion spectrum MRI of the brain of a normal volunteer is shown in Figures 4.2 and 4.3. Figure 4.2 compares the signal  $|S_{\Delta}(\mathbf{q})|$  and its 3D FT, the diffusion spectrum  $\bar{p}_{\Delta}(\mathbf{r})$ , for a voxel within the brainstem. Here, the signal  $|S_{\Delta}(\mathbf{q})|$  is clearly multi-modal and far from Gaussian, and its spectrum has 3D directional maxima orthogonal to those of  $|S_{\Delta}(\mathbf{q})|$ .

Figure 4.3 illustrates the DSI experiment on a coronal slice that includes elements of the corticospinal tract and the pontine decussation of the middle cerebellar peduncles. While Figure 4.3A shows the DT image reconstructed from the DSI data, Figures 4.3 B and C zoom in the brainstem and centrum semi-ovale. At each voxel is shown the ODF represented as a spherical polar plot and colored according to local orientations. In Figure 4.3B-DSI, we see that while many voxels show spectral maxima of single orientations, corresponding to the axial corticospinal tract (blue) and medio-lateral ponto-cerebellar fibers (red), voxels within the intersection of these tracts at once show both orientational maxima. Figure

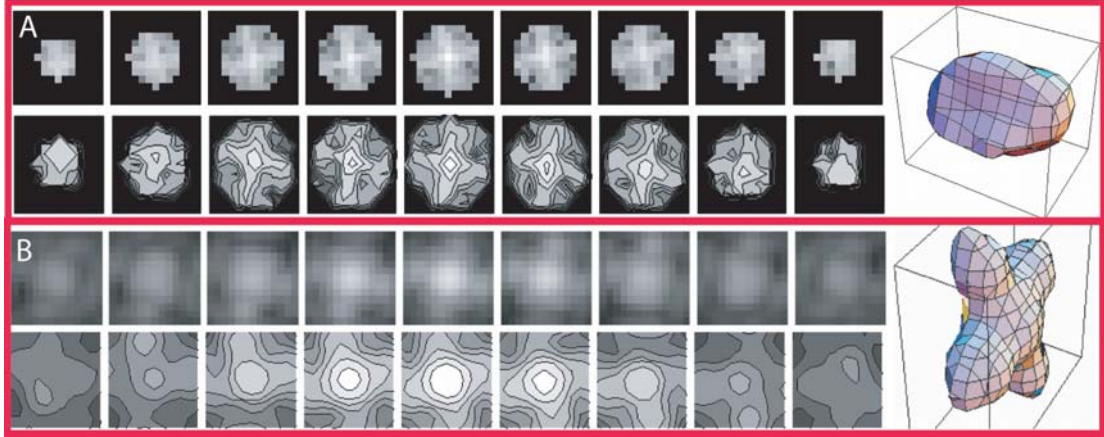


**Figure 4.2:** Spectral data for one voxel within the brainstem demonstrate heterogeneous diffusion anisotropy. Raw data  $|S_{\Delta}(\mathbf{q})|$  is shown in (A) as a set of contour plots for consecutive 2D planes in  $\mathbf{q}$ -space. These data show an intensity maximum with the shape of a tilted “X”, the two lobes of which suggest contributions of two orientational fiber populations within this voxel. In (B), the diffusion spectrum  $\bar{p}_{\Delta}(\mathbf{r})$  is reconstructed by discrete 3D FT of the raw data and is represented by 2D and 3D contour plots, the latter a locus of points  $\mathbf{r}$  such that  $\bar{p}_{\Delta}(\mathbf{r}) = \text{constant}$ . This 3D displacement spectrum shows two well-defined orientational maxima (courtesy of V.J. Wedeen).

4.3C-DSI shows a portion of the centrum semi-ovale including elements of the corona radiata, superior longitudinal fasciculus and corpus callosum, that are respectively of axial, antero-posterior, and medio-lateral orientations. Diffusion spectra demonstrate the corresponding orientational maxima, and in particular include voxels exhibiting 2- and 3-way coincidences of these tracts. Figure 4.3B-DTI and C-DTI that show the diffusion tensor image reconstructed from these same data. Note that in Figure 4.3C the diffusion tensor (C-DTI) of a voxel showing a symmetric 3-way (C-DSI) crossing corresponds to a diffusion tensor of low anisotropy (see yellow circle).

The orientational maxima of local cerebral diffusion can be used to identify in every voxel the axonal orientation of several fiber populations. In Figure 4.4 we imaged a parasagittal brain block and used sticks to represent those maxima. We can easily identify callosal fibers with the red sticks, the cortico-spinal tract in blue and the arcuate fasciculus with the green sticks. On the coronal slice we seen in the centrum semi-ovale red-blue crosses indicating the crossing of the cortico-spinal tract and the corpus callosum. On the axial slice, crossing sticks indicate the intermixing of callosal fibers with the arcuate fasciculus (red-green) as well with the corona-radiata (red-blue).

Application of diffusion spectrum MRI to muscular tissues is illustrated by ex-vivo studies of the tongue. The intrinsic muscles of the tongue a sheath of conventional skeletal muscle of longitudinal orientation, and a core of orthogonal interlaced fiber bundles of the transversus and verticalis muscles whose coupled contraction enables the tongue to stiffen, deviate, and protrude in opposition to the longitudinalis. This architecture is clearly delineated



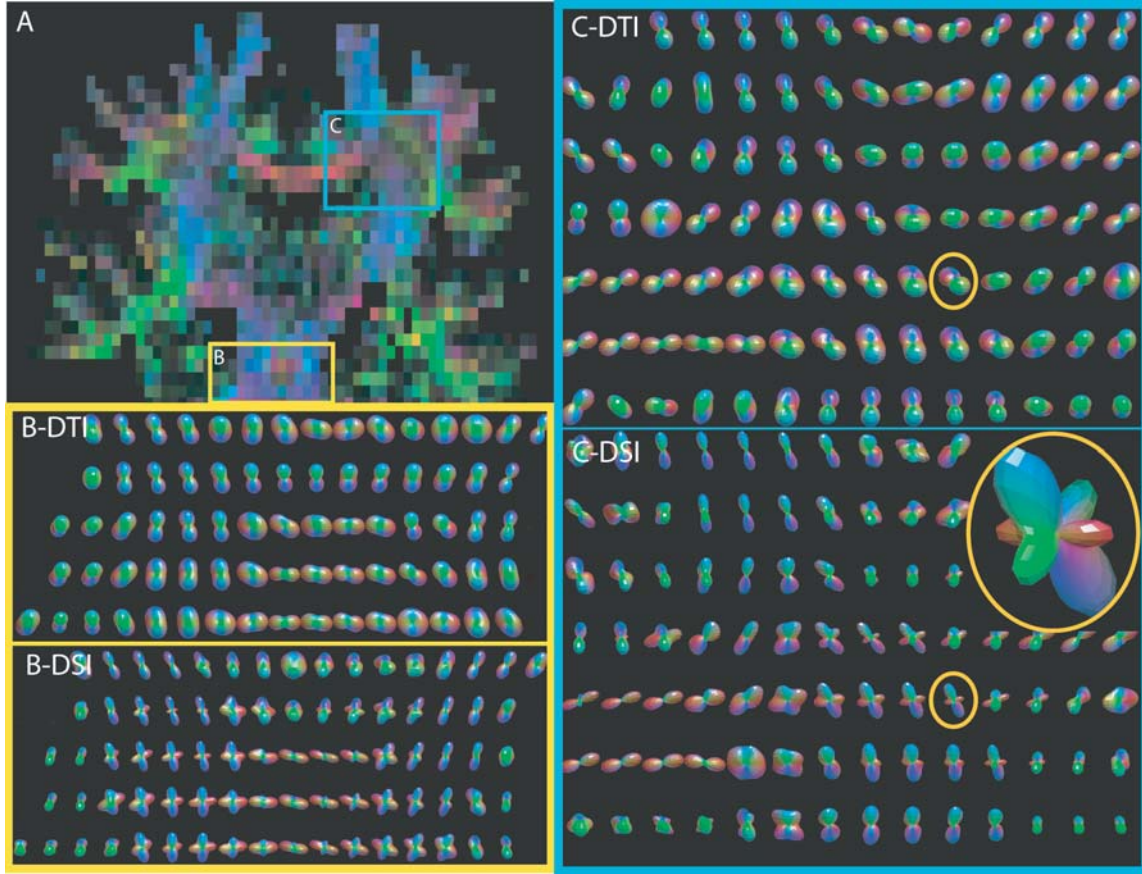


**Figure 4.3:** Cerebral diffusion spectrum MRI of normal human subjects. In (A), the complete coronal brain slice under study is depicted. Diffusion is represented with a tensor fit from the DSI data. The DT data is represented as a color map (Section 2.9.3). Image (B) and (C) are zooms on the brainstem and the centrum semi-ovale; the areas are represented with polar plots of the ODFs that are color-coded depending on diffusion orientation. (B-DTI) represents the brainstem as measured by DTI, while (B-DSI) is a representation of the DSI measurements. Here, the corticospinal tract contributes spectral maxima of axial orientation (blue lobes along the vertical axis) and the pontine decussation of the middle cerebellar peduncle contributes horizontally (red lobes crossing at center). Many local spectra show contributions of both structures. Image (C-DSI) shows the centrum semi-ovale measured by DSI. It contains elements of the corticospinal tract (blue), corpus callosum (red) and superior longitudinal fasciculus (green), including voxels with two- and three-way intersections of these components (yellow circle). Orientational correspondence between tensor and spectral data is best at locations with simple unimodal spectra while locations with multimodal diffusion spectra correspond to relatively isotropic diffusion tensors.



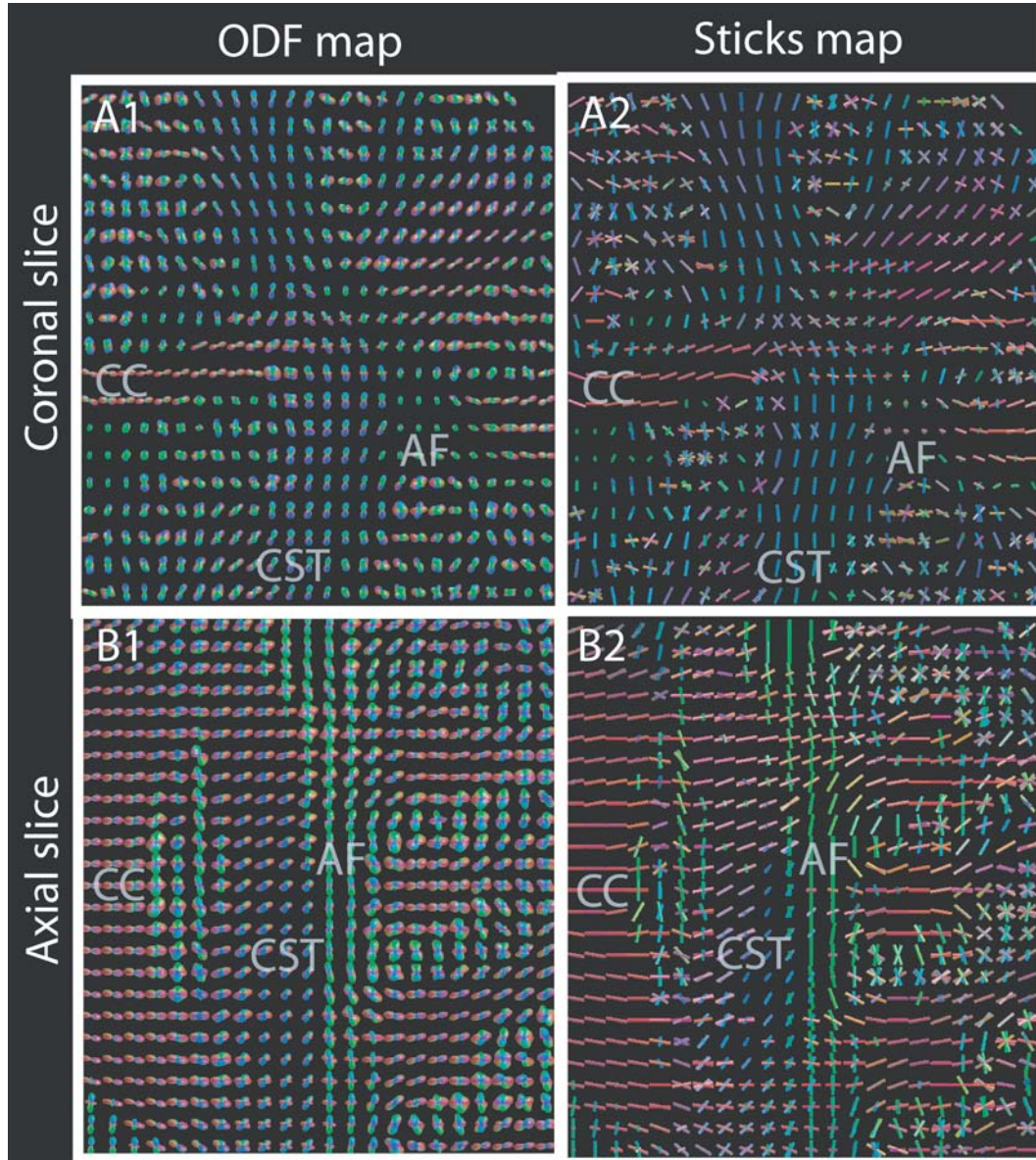


**Figure 4.4:** Brain map of orientational diffusion maxima. From the ODF map (A1 and B1), colored sticks (A2 and B2) are used to represent the local maxima of diffusion in every voxel. They are used to identify the local axonal orientation of several fiber populations. We can see callosal fibers in red (CC), the cortico-spinal tract in blue (CST) and the arcuate fasciculus in green (AF). The coronal slice highlights the crossing between the corpus callosum and the cortico-spinal tract, whereas the axial slice show the intermixing between the callosal fibers with the arcuate fasciculus (red-green) and with the corona-radiata (red-blue).

in diffusion spectrum MRI of a bovine tongue (Figure 4.5). While spectra at superficial locations show single longitudinally-oriented maxima, corresponding to the longitudinalis muscle, core voxels usually show two approximately orthogonal maxima corresponding to the transversus and verticalis muscles.

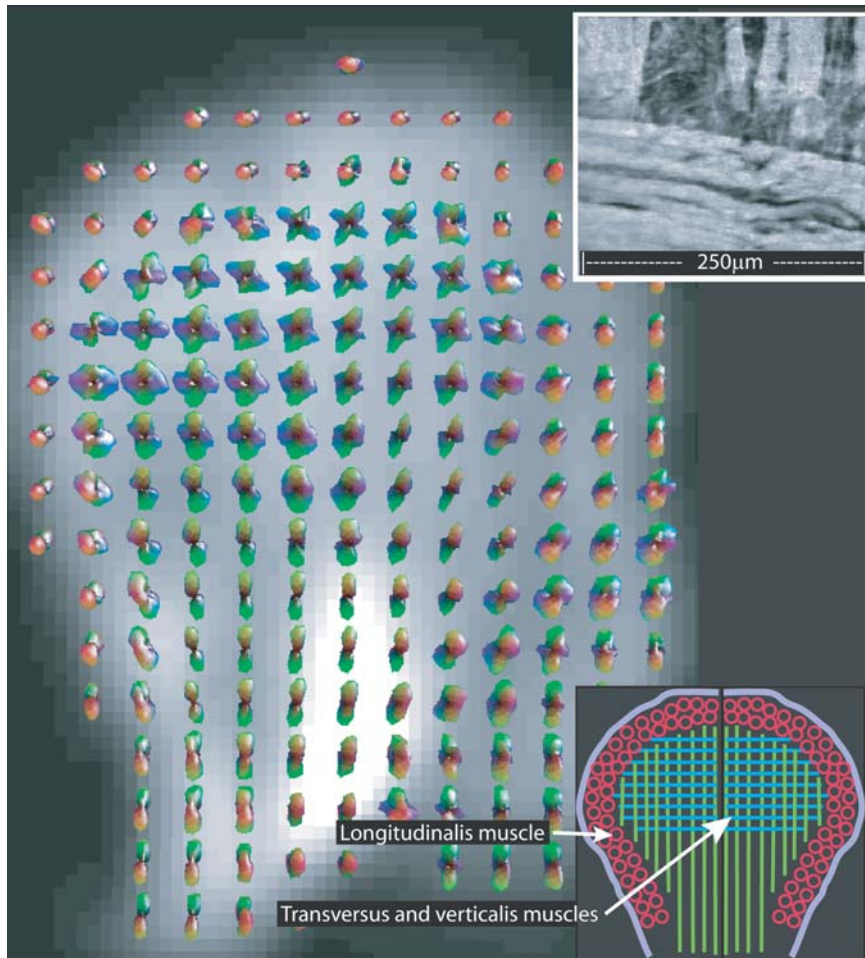


**Figure 4.5:** MRI of complex muscle. In this image we see a diffusion spectrum MRI of the bovine tongue, a coronal slice with 4 mm resolution, represented as polar plots of the ODFs. The longitudinalis muscle seen at the superior surface of the tongue shows a single through-plane orientation (red). The core of the tongue shows the intersecting elements of the transversus (blue) and verticalis muscles (green), which often coexist within one voxel. On the top right, an electron micrograph that illustrates the intersecting fascicles at the micrometric level (courtesy of V.J. Wedeen, V. Napiedow and R. Gilbert).

## 4.5 Discussion

### 4.5.1 A General Approach for Biological Samples

Away from the simplistic homogenous and unrestricted diffusion model as well as far from the fully restricted diffusion model, the present approach encompasses the general situation expected in vivo in which microenvironments of distinct anisotropic diffusivities exchange spins across a continuum of timescales. In other words, depending on the allowed diffusion time  $\Delta$ , the water molecules have more or less time to explore the tissue environment, influencing accordingly the diffusion spectrum. Let us consider a simple model made of a connected porous system, following the image given by Callaghan (p. 390 [29]). Intuitively, when the diffusion time is such that the average diffusion distance is much smaller than the restriction geometry, the diffusion spectrum is an isotropic Gaussian function. At intermediate time scales, spins are given a chance to explore fully the local compartment without exchanging significantly between adjacent pores. Hence, the diffusion spectrum captures the additive effects of the pore shape autocorrelations. At longer time scales spin exchange equilibrates successively with more distant compartments that generate successive cross-correlation terms between pores. If these compartments have different shapes and/or orientations, then the appearance of cross terms will result in a blurrier diffusion spectrum. This suggests that there must exist an optimal diffusion time for which the diffusion spectrum is orientationally the sharpest.

### 4.5.2 Diffusion Spectrum and Fiber Orientation

The analysis of tissue fiber architecture with DSI is based on a familiar principle that water diffusion in biological materials is least restricted in directions parallel to fibers [14]. When considering voxels of single fiber population, the signal  $S(\mathbf{q})$  in 3D  $\mathbf{q}$ -space is bright over a 2D disc, perpendicular to the fibers direction. After 3D FT, the resulting diffusion spectrum concentrates along a line corresponding to the fiber direction. With two crossing fiber populations, we move from two intersecting discs in  $\mathbf{q}$ -space to two lines of maximum intensity in the reciprocal space. In the context of mapping fiber orientation the 3D FT of the MR signal has two obvious consequences. First it enhances the SNR by projecting the samples in a disc into a line, concentrating the energy of the data in a smaller volume fraction of a 3D space. It is just as in spectroscopy where the FT concentrates the (long time) FID in a (band limited) spectral peak. Second, whereas in the multi-component case, the minima and maxima of two crossing discs in  $\mathbf{q}$ -space are meaningless, after 3D Fourier transform those maxima correspond to clear fiber orientations (Figures 4.1 and 4.2). Like DT imaging, DSI associates fiber orientations with directions of maximum diffusion but now admits the possibility of multiple directions at each location. Histologically, neural tract and muscle intersections such as the examples (Figures 4.3, 4.4 and 4.5) above consist of interdigitating multi-cellular fascicles of tens to hundreds of microns in diameter. While diffusion DT imaging of such architectures would essentially need to resolve individual fascicles and therefore need micrometric resolution, DSI overcomes this limitation by defining



orientational coherence without individually resolving constituent fascicles. Such DSI requires only sufficient spatial resolution as to limit intra-voxel dispersion of fiber orientations belonging to a neural tract, produced by bend, splay and twist.

### 4.5.3 DSI vs Other Diffusion MRI Techniques

DT-MRI is a widely used imaging technique that is based on a Gaussianity hypothesis. As we are now able to sample without any a priori the diffusion function, it is worthwhile to understand the relationship between these techniques. We have mentioned above that the MR signal  $S_\Delta(\mathbf{q})$  can be seen as the characteristic function of the random variable  $\mathbf{r}$ , that describes the average spin displacement in a voxel [129]. The first few terms of its 3D Taylor expansion around zero are:

$$\ln[S_\Delta(\mathbf{q})/S_0] = 0 + i\mathbf{q}^T E(\mathbf{r}) - \frac{1}{2}\mathbf{q}^T [E(\mathbf{r}\mathbf{r}^T) - E(\mathbf{r})E(\mathbf{r})^T]\mathbf{q} + O(|\mathbf{q}|^3), \quad (4.4)$$

where  $E(\cdot)$  means expectation and  $[E(\mathbf{r}\mathbf{r}^T) - E(\mathbf{r})E(\mathbf{r})^T]$  is the covariance matrix. As seen previously, we can take into account that the signal is a centered and even function (i.e. odd terms are zero). To move to the DT model, we see from the above expression that we need to neglect the terms of order higher than 2. This can be done if (i) either the wave vector  $\mathbf{q}$  is small (i.e.  $\mathbf{q}^T E(\mathbf{r}\mathbf{r}^T)\mathbf{q} \ll 1$ ) or (ii) diffusion is Gaussian (moments of order higher than 2 are zero). We then can rewrite (4.4) in the following form:

$$S_\Delta(\mathbf{q})/S_0 = e^{-\frac{1}{2}\mathbf{q}^T E(\mathbf{r}\mathbf{r}^T)\mathbf{q}} \quad (4.5)$$

$$= e^{-\Delta\mathbf{q}^T \mathbf{D}\mathbf{q}}, \quad (4.6)$$

Where the diffusion tensor  $\mathbf{D}$  is defined by the Einstein relation ( $E(\mathbf{r}\mathbf{r}^T) = 2\Delta\mathbf{D}$ ) and we are back to the classical DT-MRI formula [97]. In the brain tissue, the first condition is probably close to be satisfied when b-values are less than 1000 s/mm<sup>2</sup>, and the second in regions that exhibit single fiber orientation. Indeed, the Taylor expansion suggests a simple way to measure non-Gaussianity by considering the multivariate kurtosis ( $\beta_2$ ), function of the fourth order moment, of the diffusion function. Interestingly the image of  $-\beta_2$  of a brain slice (Figure 4.6A) looks very similar to the DT-MRI based fractional anisotropy (FA) map (Figure 4.6B, correlation coefficient,  $r = 0.6$ ). This relation provides us with a new interpretation of the meaning of FA. High FA can be interpreted as brain areas where the anisotropic Gaussian model is a good approximation and suggests unimodal fiber orientations. Whereas low FA occurs precisely where kurtosis is high and corresponds to regions of complex fiber architecture. We therefore need to interpret with care DT-MRI images where neither of the above conditions is satisfied.

It is also worthwhile noticing that in Equation 4.4 the moments can be expressed in terms of diffusion tensors of corresponding order, thus bringing up the generalized diffusion tensor formalism developed by Liu et al. [104].

Recently methods called "high angular resolution" have emerged. They all reside on the same principle, which consists of acquiring a large number of diffusion weighted samples of constant b-values uniformly distributed over a spherical shell. The ODFs are then

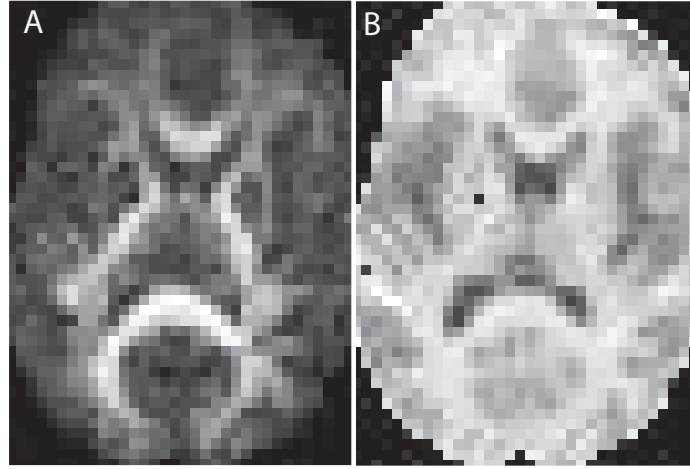


**Figure 4.6:** In Figure A), the FA map of a brain slice computed by reconstruction of the DT from the DSI data. Figure B) represents minus the kurtosis computed on the diffusion spectrum. Noticeable correlation between both images ( $r = 0.6$ ).

reconstructed by various algorithms. Optimization schemes are used like in [82, 152] or direct reconstructions like in q-ball imaging [151]. Put in the context of q-space imaging we notice that — in the same way as DTI and its associated Gaussian model can be seen as a low pass approximation of the evolved diffusion function — sampling a sphere of constant b-value at high angular resolution is equivalent to high pass filtering the diffusion spectrum. The problem then resides in recovering the exact ODF from a band limited signal, which requires clever a priori information.

Y. Cohen et al. [6, 38] studied simple tubular tissue geometries by sampling in q-space a line perpendicular to the main tissue axis. It allowed them to retrieve information about the diameter of the tubular shape by studying the diffraction patterns or by computing the 1D FT of the acquired 1 dimensional MR signal. Again in the context of DSI, one dimensional q-space imaging can be understood as a projection imaging technique as the 1D FT along a line in q-space is the projection of the 3D diffusion spectrum on that same line. Like all projection imaging techniques, the mapping between the 3D shape and its 1D projection is not necessarily one to one (e.g. bi-exponential decay could be related to two compartments of different diameters but also of different orientation or permeability), reason why this type of imaging, if easy to handle in simple geometries, might raise intractable interpretation problems if done on tissues with intra-voxel orientational heterogeneity like the brain.

## 4.6 Conclusion

We have described a new diffusion MRI technique called DSI. It is a truly six dimensional imaging technique that makes fiber orientation imaging a conventional MRI technique, in the sense that it is faced to the standard MRI limitation like SNR and "angular" resolution and is based on minor assumptions. We have showed that DSI has the capacity to unravel

structural information of tissue architecture as complex as micrometric interdigitating muscle fibers and crossing axonal fibers in the central nervous system, this without the need for a priori information or modeling.

## Part II

# Tractography: Between Contrast Mechanism and Axonal Modeling





---

# Statistical Fibre Tracking and Virtual Dissection from DTI

---

# 5

*Devenir adulte (...) C'est apprendre à  
vivre dans le doute et l'incertitude.*

H. Reeves

## 5.1 Introduction

Recent developments in diffusion MRI have put this imaging modality to the forefront of interest among the neuroscientific community. As we have seen in previous chapters, the success of diffusion imaging is related to the fact that during their random, diffusion-driven displacements, water molecules probe tissue structure at a microscopic scale well beyond the usual imaging resolution [102]. It has been shown that, in the brain, ordered axonal structure, cell membrane and myelin sheath strongly influence water diffusion [15, 16] and that there is a direct link between water diffusion and axonal orientation and integrity [40, 164] (see Section 2.5). In fact when DTI is performed within a compact tract with parallel running axonal trajectories like the cortico-spinal tract, the Diffusion Tensor (DT) is strongly anisotropic and its principal eigenvector corresponds to the direction of the fibre tract.

These observations were used by several researchers to develop fibre tracking algorithms that all have the same aim: inferring from a DT field the axonal or at least bundles of fibres trajectories — the diameter of an axon being well beyond the resolution of a current MRI scan. Impressive results have been achieved and a wide spectrum of applications is to foresee. A better understanding of diffusion properties in many brain related diseases, e.g. multiple sclerosis [50, 106], dyslexia [89], Alzheimer's disease [21, 130], schizophrenia [52, 103], brain tumours [49, 114], periventricular leukomalacia [76] as well as spinal cord injury [107] should benefit from those developments. The understanding of normal brain

function needs not only the description of activated cortical areas, like provided by fMRI, but also a detailed description of the underlying neuronal circuitry.

Most of the algorithms used to infer bundles of fibres from DT imaging are based on a discrete resolution of the integral curves of the vector field corresponding to the reduction of the diffusion tensor to its largest eigenvector (see for example [12, 39, 86, 112, 143] and [113] for review). Motivated by the fact that those deterministic integral path approaches have difficulties handling regions of low anisotropy and noise, this work investigates brain circuitry with a random-walk-based algorithm that objectively takes into account the probabilistic relation between the DT and fiber tract orientation.

## 5.2 Material and Methods

### 5.2.1 MRI Data Acquisition

The images used for this study were acquired with a 1.5 T clinical MRI scanner (Magnetom Symphony; Siemens, Erlangen, Germany). The data were produced with a diffusion-weighted single-shot EPI sequence using the standard Siemens Diffusion Tensor Imaging Package for Symphony. We acquired 44 axial slices in a 128 by 128 matrix size covering the whole brain. The voxel size was 1.64 by 1.64 mm with a slice thickness of 3.00 mm without gap. Timing parameters were a TR of 1000 s and a TE of 89 s. Diffusion weighting was performed along 6 independent axes according to Basser's polyhedral tessellation [11]. We used a b-value of 1000 s/mm<sup>2</sup> at a maximum gradient field of 30 mT/m. A normalizing T<sub>2</sub> image without diffusion weighting was also acquired. In order to increase the signal-to-noise ratio the measures were averaged 4 times. An anatomical T<sub>1</sub> magnetization prepared 3D rapid acquisition gradient echo (MPRAGE) was also performed during the same session. The whole examination lasted about one hour. Images were obtained from two healthy volunteers (one male and one female, both between 25 and 30 years old). Informed consent from both subjects was obtained in accordance with institutional guidelines.

### 5.2.2 Data Pre-processing

The DT was computed for each voxel by linear combination of the log-ratio images (Section 2.9.2). The data were then linearly interpolated in order to obtain a volume with a 3D regular grid of 1.64 mm by side (matrix of 128 by 128 by 79). We computed then some useful scalar images like the fractional anisotropy (FA) map and a color map (Section 2.9.2).

An important condition for any fibre tracking algorithm to work properly is to use a good mask on the tensor data. This mask prevents tracking in aberrant areas like the ventricles or outside the brain. It forbids also areas where the tensor data is uncertain for proper tracking of white matter bundles e.g. the cortex. Most authors used a binary thresholded FA map as stopping criteria, sometimes combined with a coherence measure of the principal eigenvector [12, 86, 112, 143]. We adopted a similar strategy but used a combination of the normalizing T<sub>2</sub>-weighted image and the FA map to build our mask. We used the T<sub>2</sub> water enhancing property to delineate the ventricles. The FA map was median

filtered to eliminate the slight salt and pepper effect and get homogeneous white matter regions, and then thresholded at 0.2. Both binary thresholded images were then multiplied in order to achieve precise white matter segmentation. The  $T_2$  contribution to the mask was a separation of the ventricles from the white matter and the FA mask segmented the white-grey matter border. Using a relatively low FA threshold and median filtering the FA map avoided to reject white matter voxels of low anisotropy due to fibre crossing or noise.

### 5.2.3 Statistical Axonal Trajectories

Water particles animated by thermal heat experience random motion. This Brownian movement can be described by a random walk model. It means that the particle trajectory is made of a succession of jumps that are the realization of a random variable. In an infinite homogeneous medium the distribution of the random variable is an isotropic three dimensional Gaussian function whose variance is proportional to the diffusion coefficient (Chapter 2). Living tissue or more specifically the human brain is far from a homogeneous medium. It is highly structured and highly compartmented for water particles. Under those circumstances the diffusion function deviates from an isotropic Gaussian and becomes a complicated function of position and diffusion time [160]. Considering the limitations inherent to a clinical scanner, limited acquisition time and resolution, the DT model is a reasonable compromise to reflect reality.

In a voxel where all the axons travel in a unique direction the measured DT exhibits strong anisotropy and the first eigenvector is aligned with the axonal trajectory. But as it was stressed by Pierpaoli et al. [124] and confirmed by von dem Hagen and Henkelman [156] experiments, a voxel that contains several populations of axons with different directions has a tensor which shape will change according to the proportion of each fibre population, moving toward a donut-like or spherical shape. In this situation the principal eigenvector loses its signification and tracking becomes more hazardous. The principal eigenvector is also very sensitive to noise, especially in areas of low anisotropy [85]. The family of tracking algorithms that we could globally describe as deterministic reduce the tensor- to a vector-field [12, 39, 86, 112, 143] and consequently do not take into account the uncertainty of the fibre direction. To address this issue we developed a statistical fibre tracking algorithm based on two hypotheses:

- considering a voxel, the probability of a fibre to propagate in a given direction is proportional to the corresponding diffusion coefficient. This assumption can be justified by the works of von dem Hagen and Henkelman [156] showing the positive correlation between the diffusion coefficient and the fibre orientation probability.
- Axonal trajectories or more cautiously trajectories of axonal bundles follow regular curves.

Based on these two ideas we constructed a random walk model of a particle diffusing in a non homogeneous medium, here a DT field,  $\mathbf{D}^\alpha$ , with a curve regularizing constraint emphasizing co-linearity:

$$\mathbf{x}_{i+1} = \mathbf{x}_i + \eta \boldsymbol{\Omega}_i, \quad (5.1)$$

$$\boldsymbol{\Omega}_i = \begin{cases} \frac{\lambda \mathbf{d}_i + \boldsymbol{\Omega}_{i-1}}{\|\lambda \mathbf{d}_i + \boldsymbol{\Omega}_{i-1}\|} \\ \boldsymbol{\Omega}_i \cdot \boldsymbol{\Omega}_{i-1} > 0, \end{cases} \quad (5.2)$$

$$\mathbf{d}_i = \mathbf{D}_i^\alpha \mathbf{r}_i, \text{ with } \mathbf{r}_i \text{ a random vector uniformly distributed over a unit sphere.} \quad (5.3)$$

The trajectory of a particle in a 3D Euclidean space is given by its time varying position vector  $\mathbf{x}_i$ , where  $i$  is the discrete time step ( $0 < i < I$ ). The curve that the particle propagation generates grows along a unit vector  $\boldsymbol{\Omega}_i$ , that is a random direction vector modelling the statistical nature of the diffusion process and the curve regularizing constraint.  $\boldsymbol{\Omega}_i$  is a weighted sum of the random vector  $\mathbf{d}_i$ , defined on the unit sphere and distributed according to the local diffusive properties\* and the previous displacement vector  $\boldsymbol{\Omega}_{i-1}$ , enhancing co-linearity.  $\boldsymbol{\Omega}_i \cdot \boldsymbol{\Omega}_{i-1} > 0$  is just an additional constraint to avoid backward jumps.  $\eta$  is the step size (here  $\eta = 0.75$ ) whereas  $\alpha$  is an anisotropy enhancing exponent.  $\alpha$  is a power to the diffusion matrix  $\mathbf{D}$ . If  $\alpha$  is put to 1 the algorithm gives a lot of weight to possible fibre trajectories deviating from the main direction whereas if  $\alpha$  is large the distribution is tightened around the main eigenvector in which case the propagation rule comes close to a classic main eigenvector-based fibre tracking. We propose a value of 2 for  $\alpha$  as a good compromise between alternative path exploration and near main diffusion direction propagation.  $\lambda$  is a constant tuning the relative importance of the random diffusion component versus the curve regularizing term. As  $\lambda$  approaches zero, the global regular shape of the curve will be favoured, whereas if set to a large number more weight is given to the local DT (here  $\lambda = 1$ ).

In order to map the connectivity of the entire brain random curves were initiated on a bootstrap of the white matter. This means that a given proportion of the mask voxels, e.g. 40%, were selected randomly to be an initiation point for curves. From those voxels  $n$  curves (e.g. 10) were grown in both directions. The curve elongation stopped when a maximum of  $I$  steps were performed (e.g. 100, depending of size of the step) or the border of the mask was reached. The result was a statistical estimate of the entire brain connectivity, modelled by a "huge spaghetti plate" of about 100'000 curves. This operation, which needs to be done only once for one DT-MRI dataset, took several hours on our machine with unoptimized Matlab code.

#### 5.2.4 Tract Selection or Virtual Dissection

In order to visualize anatomical connections in the form of separate identifiable tracts or bundles, a virtual dissection in this modelled brain had to be performed. This was done in

---

\*Here  $\mathbf{d}_i$  is a single contraction between the nearest neighbour DT,  $\mathbf{D}_i^\alpha$ , and a random vector uniformly distributed over a unit sphere,  $\mathbf{r}_i$ .

two main steps: first a selection by knowledge-based Region Of Interest (ROI) placement and secondly selection by fibre validity classification.

As Mori et al. [115] in a deterministic framework, we defined here a ROI as a volume that selects fibres. The manner those ROI were placed needed some attention. Because our approach toward fibre tracking was stochastic, there was a potential risk to map aberrant connections, although those should be very few as compared with real tracts. Therefore to avoid a possible bias in the results, we adopted the following general approach:

1. The placement of a first ROI is chosen according to the structure that shall be investigated, guided by the knowledge coming from post-mortem anatomical studies.
2. The general structure of the tract appears, though it might be mixed up with other pathways. Their origin, termination and trajectories can be appreciated.
3. The different tracts selected are identified by confrontation with the post-mortem studies.
4. If necessary a second or a third ROI is selected, in order to separate the tract of interest from the others.

Axonal trajectories were modeled as a result of a stochastic process, thus imbedding in the algorithm the orientational uncertainty related to the DT[124, 156]. Among the very large number of curves generated some accurately match reality whereas others are aberrant. If along an axonal trajectory the tangential diffusion can locally drop due to fibre crossing or fanning in a voxel, we expect, the tangential diffusion coefficient averaged along the axonal trajectory to be large. Therefore trajectories that follow directions of high diffusion should be more likely than those which do not. To select a posteriori the "good" trajectories, we assigned to each curve a Validity Index (VI), which is the result of an integration of the tangential diffusion coefficient along the trajectory and normalized to the length:

$$VI = \frac{\sum_{i=1}^I \eta \Omega_i^T \mathbf{D}_i \Omega_i}{\sum_{i=1}^I \eta \|\Omega_i\|} = \frac{1}{I} \sum_{i=1}^I \Omega_i^T \mathbf{D}_i \Omega_i, \quad (5.4)$$

where  $\Omega_i^T \mathbf{D}_i \Omega_i$  is the double contraction of the DT,  $\mathbf{D}_i$ , with the unit displacement vector,  $\Omega_i$ . This contraction is the diffusion coefficient in the displacement direction. For tracts that were selected by one or several ROI, the histogram of the fibre population VI could be plotted. It followed usually a bell shaped distribution. Fibres below a certain quantile (here 20%) were then discarded so that only the most credible fibres with a high VI were retained.

In Figure 5.1 we took the example of the occipito-frontal fascicle, an important association bundle [118] for illustrating the technique. A first yellow ROI was placed in the caudal part of the brain (Figure 5.1c). A large population of fibres was selected among which the occipito-frontal projections as well as fibres of the superior and inferior longitudinal fascicles and fibres belonging to the corona radiata and posterior cortico-thalamic projections (not visible here in those sagittal figures). Willing to visualize only the occipito-frontal

connections, a second yellow ROI was then placed in the frontal brain (Figure 5.1d). In some situation, instead of choosing a second ROI it was more appropriate, because less susceptible to bias the result, to cut out fibres that pass out of a region. We illustrated it here in Figure 5.1e with a blue box. The final step of our virtual dissection was to eliminate unlikely fibres that are defined as having a VI inferior to the 20<sup>th</sup> quantile (Figure 5.1f).

We used actually in this paper three type of ROI that have been colour coded in the following way: 1) yellow region selected fibres that pass through the box, 2) fibres passing in a red box were cut out and 3) fibres that passed out of a blue box were also discarded.

### 5.2.5 Various Connectivity Maps

The classical way of fibre tract representation is a simple trajectory plot. We also adapted Koch et al. [92] statistical density maps to our algorithm. From the computed axonal trajectories we summed in each voxel the number of curves that passed through. This measure gave us for each voxel a qualitative measure of the probability that a given voxel was connected with the ROI or an empirical measure of the relative amount of fibres of the given tract that passed through that voxel (Figure 5.1g and h). We used these two ways of representing connectivity because they are both useful and complementary.

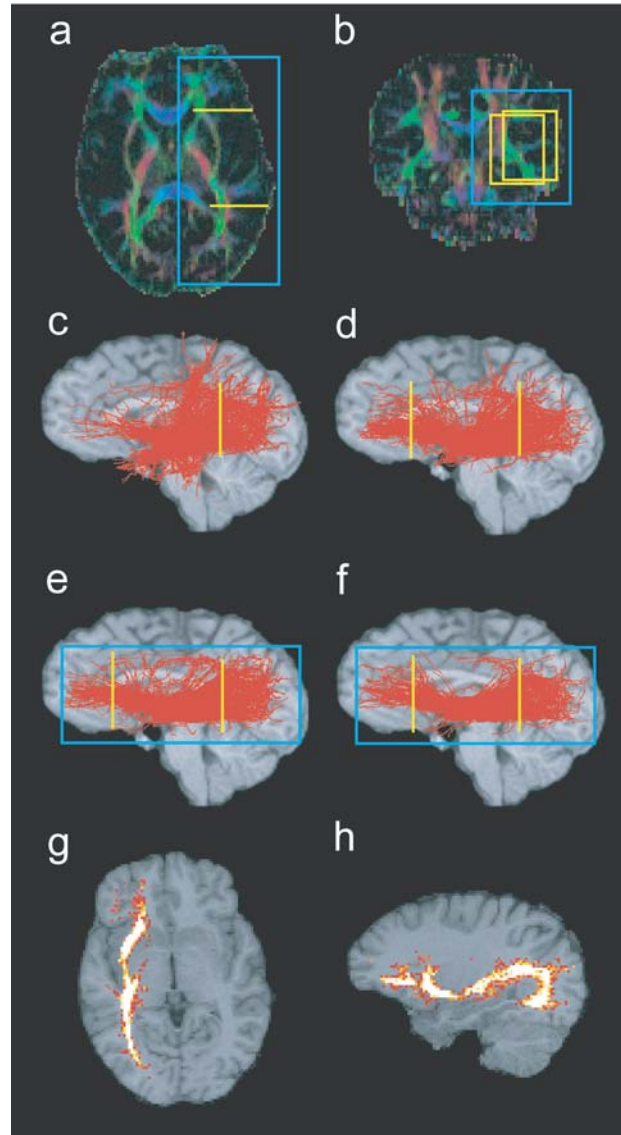


**Figure 5.1:** Virtual dissection of the occipito-frontal fascicle and various connectivity maps as an example of the methodology. a) and b) colour maps with ROIs. c) fibres passing a posteriorly placed yellow ROI. d) fibres selected in c and also passing in the second anterior yellow ROI. e) fibres selected in ROI d and that do not pass outside the blue frame. f) fibres selected in e that have a VI above the 20<sup>th</sup> quantile. g) and h) statistical density maps of the fibres selected in f.

### 5.3 Results

The evaluation phase of this research work was performed on two healthy volunteers. It allowed assessing the capacity of our tracking algorithm to infer axonal connectivity by comparing the results to post-mortem based neuroanatomical knowledge, using Nieuwen-

huys et al. [118] atlas. We applied the above mentioned methodology in order to perform a virtual dissection of several well known anatomical systems. This collection of connectivity maps can also be considered to be the beginning of an in-vivo brain connectivity atlas. The illustrations are always organized in a similar manner. Two colour maps are used to present the location of the ROI. Some images present the tract of interest on three-dimensional views whereas a few are projections on an anatomical  $T_1$ -weighted slice and some others are statistical density maps. We did systematically a bilateral investigation using perfectly symmetric ROI so that side comparison was possible.

### 5.3.1 Cortico-Bulbar and Cortico-Spinal Tracts

The cortico-spinal tract is a large, well characterized and highly anisotropic tract. It has therefore been used by several authors for evaluating their tracking algorithm [12, 65, 86, 93, 125, 140, 143]. The anatomical position of these fibres as well as the position of the cortico-bulbar tracts is in the brain stem well described in the literature, for comprehensive summary see Nieuwenhuys et al. [118]. And at that level the different bundles separate well. With different locations of the ROIs we have achieved the dissection of different tracts. For the whole analysis of this subsection we have excluded fibres coming from the cerebellum on their way to the brain stem.

Figure 5.2a shows fibre tract selection by an axial ROI in the ventro-medial part of the cerebral peduncles. The fibres thus selected originate mainly in the frontal cortex and are classically described as the fronto-pontine tract. If the ROI was placed more laterally in the ventro-lateral part of the cerebral peduncle, the selected fibres corresponded to the pyramidal tract, originating mainly in the region of the central sulcus and travelling down the brain stem (Figure 5.2b). Placing the ROI at the dorso-lateral border of the cerebral peduncle revealed what can be regarded as the parieto-temporo-pontine tract (Figure 5.2c).



### 5.3.2 Cortico-Thalamic Projections

The thalamus sends and receives axons from the different cortical areas. The thalamo-cortical connections can be roughly separated in three groups, the anterior, superior and posterior projections.

For selecting the anterior projections we placed two ROIs in the frontal plane, one in the anterior part of the thalamus and the other larger ROI in the frontal lobe white matter, anterior to the genu of the corpus callosum (Figure 5.3a). Fibres that ran caudally beyond the thalamus were eliminated. In Figure 5.3b we visualized the superior projections by placing an axial ROI in the upper part of the thalamus, fibres running further down were discarded. A similar approach was adopted for the posterior projections by placing ROIs in the frontal plane, one in the posterior part of the thalamus and an other large window in the white matter at the level of the temporo-occipital junction (Figure 5.3c). Fibres running rostrally beyond the thalamus were eliminated.

### 5.3.3 Corpus Callosum and Limbic System

In order to identify fibres passing through the corpus callosum we placed a large ROI encompassing the whole corpus callosum at the mid sagittal plane (Figure 5.3d).

Some of the major pathways constituting the limbic system are known to be the fornix and the cingulate bundle. The horizontal portion of the fornix was isolated by placing a ROI in a frontal plane para-sagittally beneath the body of the corpus callosum. But both anterior and posterior columns together with the temporal extension could not be identified. This could be due to an insufficient spatial resolution of our DT acquisition technique. The cingulum was identified by using two ROIs placed in a frontal plane, 2 cm apart within the white matter of the cingulate gyrus (Figure 5.3e).

### 5.3.4 Cortical Association Bundles

Cortico-cortical connections are widespread and they form only loose association bundles that are variable in size and shape. Using our method we visualized four of those major association bundles.

Figure 5.4a shows the inferior occipito-frontal fascicle as it was isolated with two ROIs. The first was placed in the posterior parietal and the second in the frontal lobe. In order to isolate the inferior longitudinal fascicle we used also two selection ROIs. The posterior was, as for the inferior occipito-frontal fascicle, in the posterior parietal lobe, whereas the second in the temporal lobe (Figure 5.4b). For identification of the uncinate fascicle we placed a first ROI in the anterior part of part of the temporal lobe and a second one in the frontal lobe (Figure 5.4c). The superior longitudinal fascicle was selected by two ROI placed below the motor and the posterior parietal cortices in frontal planes (Figure 5.4d). This tract shows interestingly a clear left-right asymmetry.

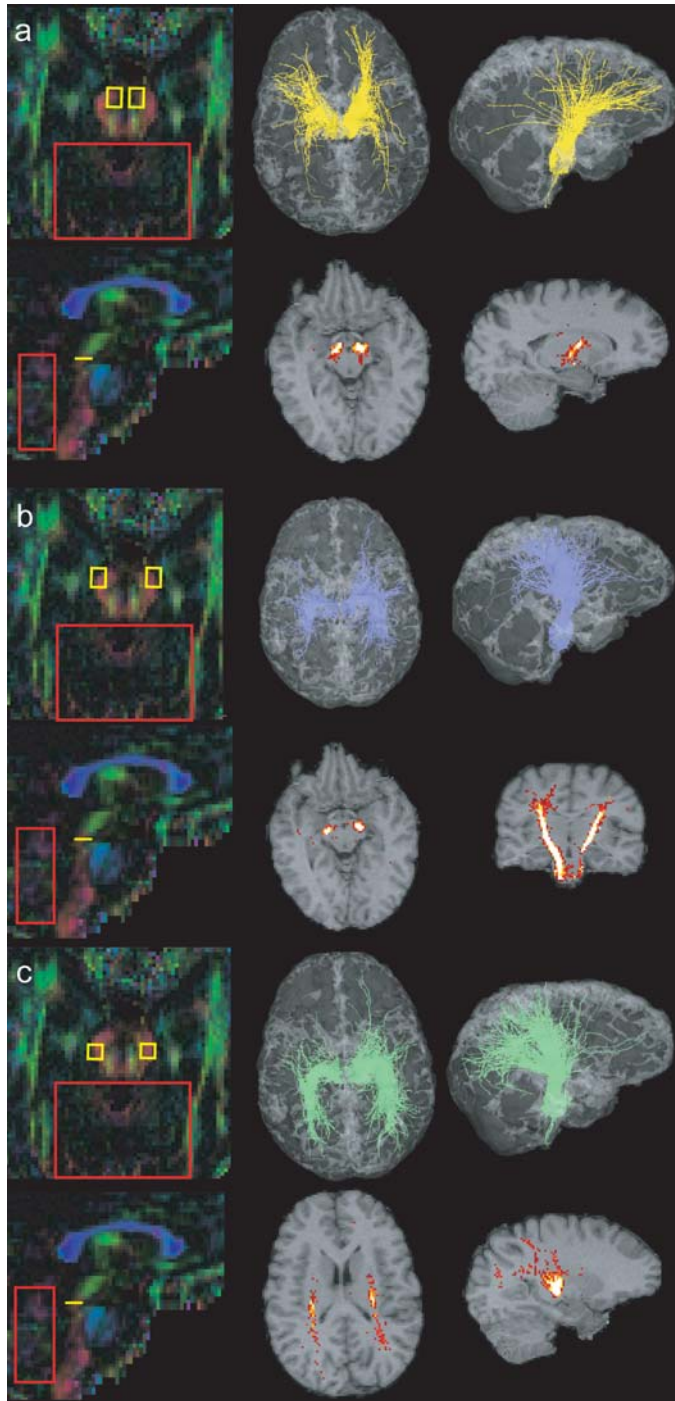


**Figure 5.2:** Cortico-bulbar and -spinal tracts. ROIs on colour maps, 3D views and statistical density maps. a) fronto-pontine tract (yellow), b) cortico-spinal tract (blue), c) parieto-temporo-pontine tract (green).

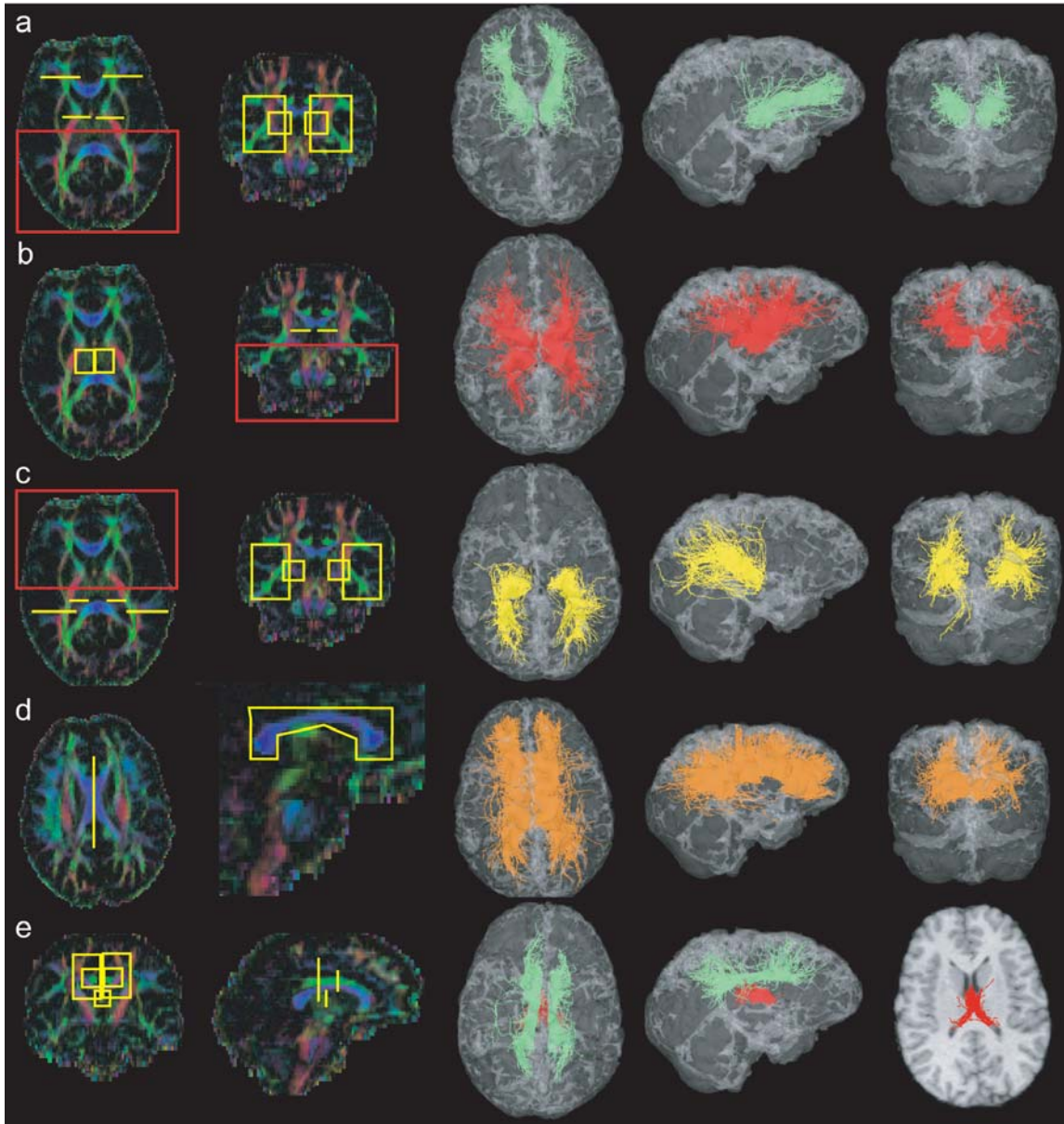


**Figure 5.3:** Cortico-thalamic, corpus callosum and limbic system projections. ROIs on colour maps and 3D views. a) thalamic frontal projections (green), b) thalamic superior projections (red), c) thalamic posterior projections (yellow), d) corpus callosum projections (orange), e) cingulum (green) and fornix (red). The lower right image is a projection of the fornix onto an axial slice.

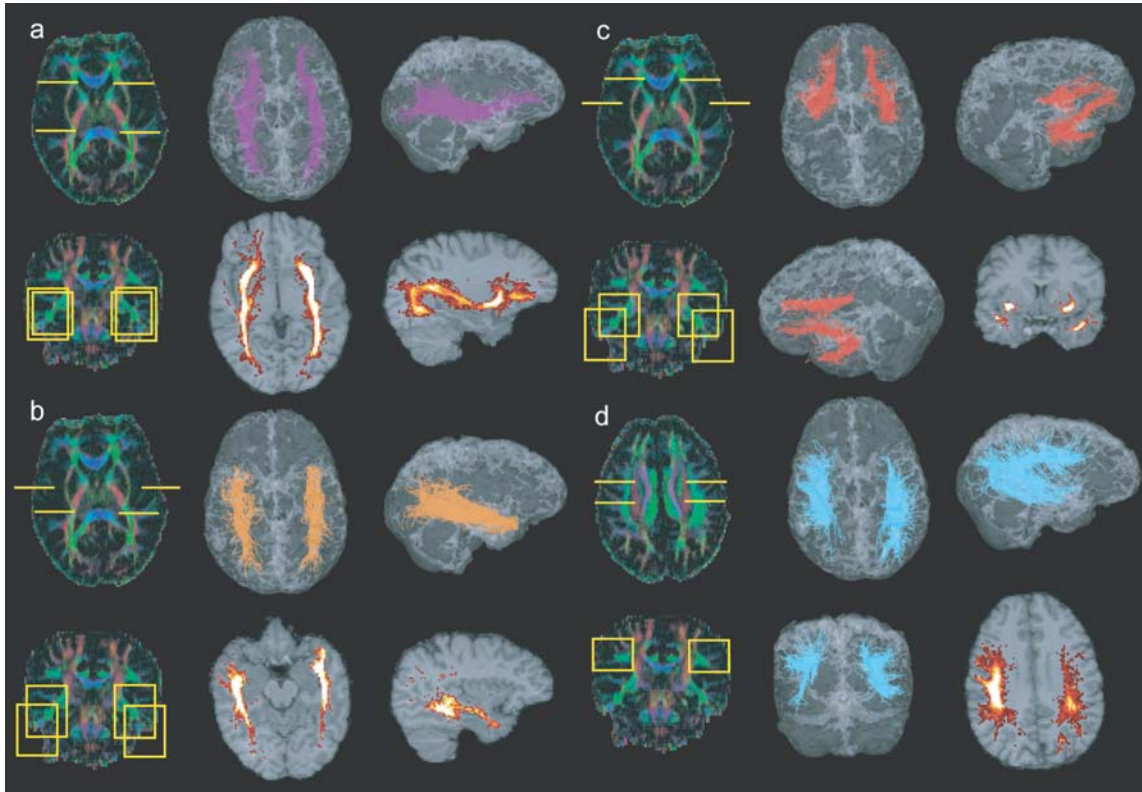


**Figure 5.4:** Cortical association bundles. ROIs on colour maps, 3D views and statistical density maps. a) inferior occipito-frontal fascicle (violet), b) inferior longitudinal fascicle (orange), c) uncinate fascicle (red), d) superior longitudinal fascicle (cyan).

### 5.3.5 Cerebellar Peduncles and Medial Lemniscus

Here we investigated the relationship between the cerebellum and the brain stem. The three cerebellar peduncles were successively identified by appropriate placement of ROIs. In Figure 5.5a we selected the right and left inferior cerebellar peduncles by means of two ROIs, one in the brain stem and one in the cerebellum. The mid cerebellar peduncle was selected by means of one ROI placed across the pons for selecting the fibres that travel in this region laterally and a second ROI was placed on the cerebellum it self (Figure 5.5b). The upper cerebellar peduncle was more difficult to isolate and we used the fact that these fibres decussates at the level of the cerebral peduncle to place a ROI in the sagittal plane. Two other ROIs were positioned in an axial plane on each side of the mid line (Figure 5.5c). Despite cautious ROI placement this tract show an asymmetry in the amount of fibres passing either left or right.

Finally looking at a colour map at the level of the pons we could easily identify the medial lemniscus that was then selected with another ROI. Those fibres are known to terminate in the thalamus (Figure 5.5d) and to visualize this fibre population we selected the fibres that did not continue beyond it.



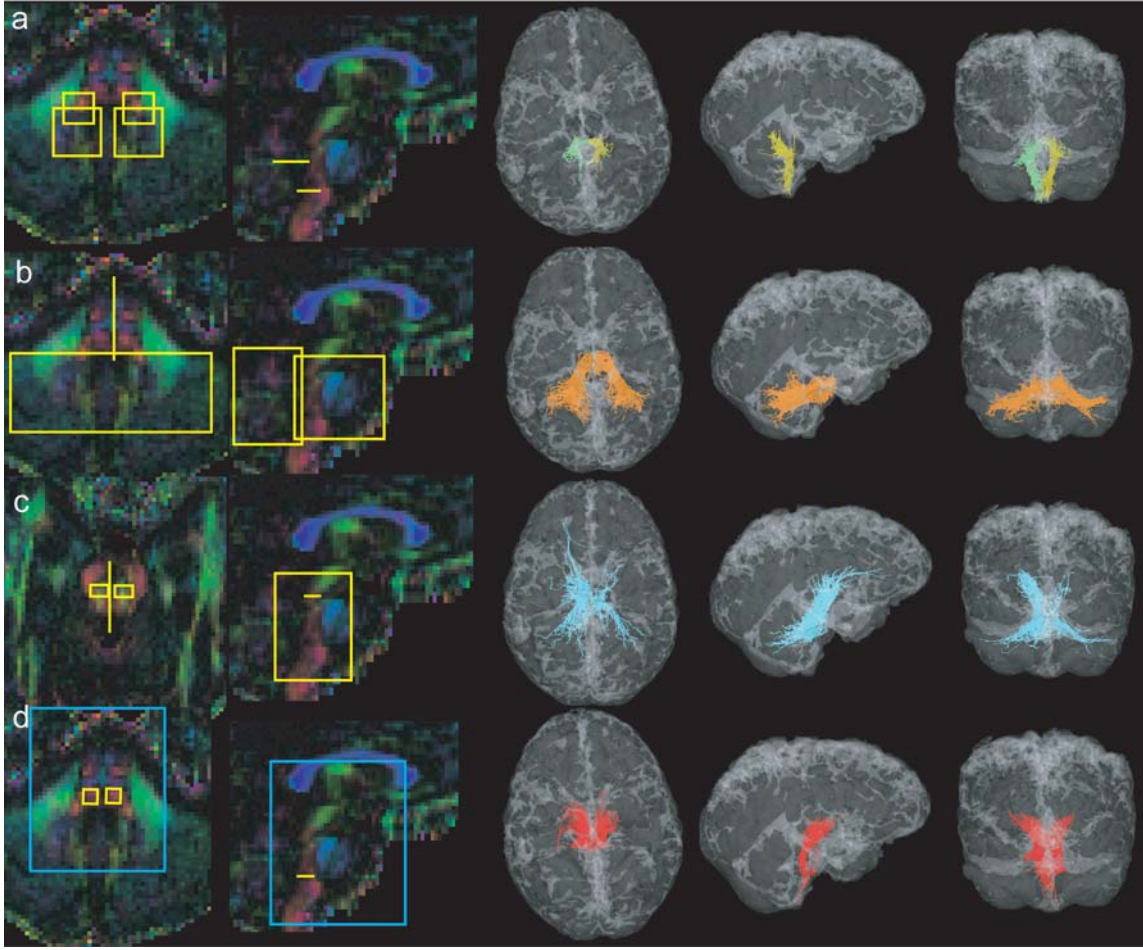


**Figure 5.5:** Cerebellar peduncles and medial lemniscus. ROIs on colour maps, 3D views. a) inferior cerebellar peduncle (green and yellow), b) mid cerebellar peduncle (orange), c) superior cerebellar peduncle (cyan) d) medial lemniscus (red).

## 5.4 Discussion

We developed here a new approach to map brain connectivity that was statistical in nature and based on a global approach toward fibre tracking. This led to the identification of several fibre tracts (Figure 5.6) that all showed accurate correlation with current post-mortem-based neuroanatomical knowledge [118]. Furthermore previous studies based on other fibre tracking methods described analogous trajectories for many of those tracts, - the pyramidal tract by [12, 65, 86, 125, 140, 143], the thalamic projections and the cortical association bundles by [115], the brain stem by Stieltjes et al. [140], and the corpus callosum by Bassar et al. [12], Poupon et al. [125], Tench et al. [143] -, thereby validating our results. The presented data constitute an in-vivo brain connectivity atlas.

Both Koch et al. [92] and our results suggest that statistical fibre tracking is a valuable way for mapping brain connectivity. But it is necessary to notice the clear differences

with the classical deterministic fibre tracking algorithms. And they should be taken into account when interpreting the results. Current deterministic tracking algorithms follow the main eigenvector of the diffusion tensor [12, 39, 86, 112, 143], reducing the available information. Thus only regions of large and homogeneous fibre bundles can be reconstructed accurately, those that have not a much smaller diameter than the size of a voxel. The identified trajectories are smooth and accurate under the assumption that the signal to noise ratio is sufficiently high for limiting the deviation of the tensor field from reality and therefore introducing instability of the discretized differential equation. These problems were investigated by Lazar et al. [96] as well as by Gossel et al. [65]. Whereas Lazar maps streamlines that are deflected by the local diffusion tensor, Gossel considers fibre tracking in a noisy main eigenvector field as an optimal filtering problem. Gossel's implementation based on a Kalman filter generates curves that follow a corrected main eigenvector in order to minimize the mean square error between the estimated and the underlying ideal tract. On the other hand, the statistical approach, as presented here, makes use of the whole diffusion information available in order to explore many potential connections. We see here three advantages:

1. the probabilistic relation between diffusion and axonal orientation is explicitly taken into account,
2. the sensitivity to noise is decreased in regions of low anisotropy and
3. the possibility of fibre crossing and divergence is introduced.

However, an uncertainty concerning the trajectory of individual fibres appears. Thus, each curve should not be interpreted as a precise mapping of a real axonal trajectory. Selected fibres should be considered together and areas of high fibre density as very likely trajectories whereas projections of few fibres may not correspond to an anatomical entity. In that sense the statistical density mapping seem a complementary tool to the trajectory maps in the context of statistical fibre tracking in order to evaluate the validity of the fibres passing by a given region.

In the presented implementation several improvements appear also when compared with Koch et al. [92]. Our random walk is continuous as opposed to voxel to voxel jumps. We map individual trajectories and not only statistical density maps. The major drawback of Koch's algorithm which is the dependence of the intensity of the connectivity measure on the distance of the initialization point has been solved in our method by multiple initialization all over the brain. This appears to be a critical point for all streamline type algorithms, as they produce different results depending where along a given fiber tract the line generation has been initiated. By the initiation all over the brain all potential solutions are produced, hence bias in favor to one or the other region is reduced.

Our approach, "whole brain simulation" and then virtual dissection, showed striking similarity with known anatomy [118]. Worth to notice are also very obvious left-right asymmetries of the superior longitudinal tract (Figure 5.4d) and the upper cerebellar peduncle (Figure 5.5c). If inadvertent asymmetric ROI selection and the statistical nature of

the algorithm might be a partial explanation, clearly, anatomical difference between both sides is a predominant component, e.g. proportion of grey and white matter [68]. These observations is be the starting point of asymmetry and male/female dysmorphism study presented in Chapter 8.

Using knowledge-based ROI for tract selection is not, at least in the context of statistical fibre tracking, an ideal solution. There remains a risk of biasing the results if the windows are not placed fairly. Therefore in the future new solution for ROI placement should be found. Another remaining problem for deterministic as well as statistical fibre tracking is the limited resolution of the imaging scanner and the incapacity of a tensor to model properly multiple fibre tracts in one voxel. High angular resolution imaging (HARDI) [55, 160] seems to be a promising tool for overcoming this limitation. Our algorithm can be easily adapted to such data since the distribution of the displacement vector  $\Omega_i$  has just to be shaped by this higher order function instead of the tensor.

Finally, fibre tracking is a complex task and different approaches can be valuable. Here, based on a random walk model, we modelled in one shot the global white matter connectivity of healthy volunteers. This model was then virtually dissected in order to identify many different fibre tracts. This collection can be seen as far as we know as a first realization of an in-vivo brain connectivity atlas.

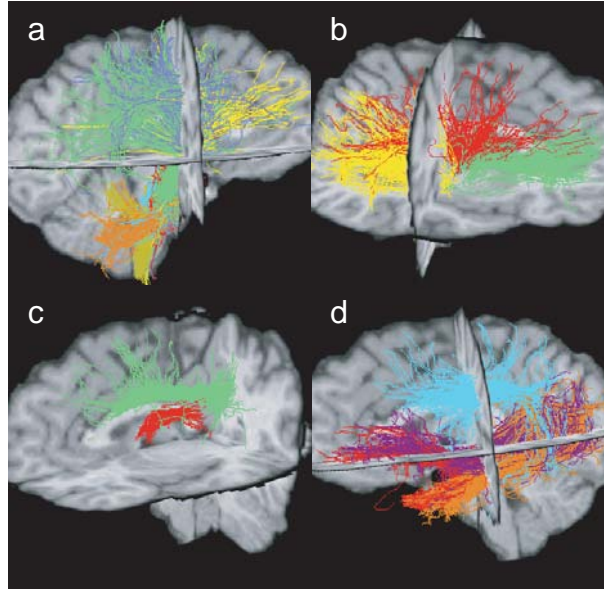


**Figure 5.6:** 3-dimensional view of several systems: a) cortico-bulbar and -spinal tracts, cerebellar peduncles, b) cortico-thalamic projections, c) limbic system, d) association bundles.





---

# DSI Tractography in Complex Cerebral White Matter

---

# 6

*I think the next century will be the century  
of complexity.*

S. Hawking

## 6.1 Introduction

Until recently the study of WM axonal architecture was the neuropathologist's private domain, who by using time consuming and work intensive histological coloring techniques managed to visualize a few long range connections (e.g. [36, 37, 41]). The advent of diffusion MRI and tractography algorithms has given a new breath to the field by allowing in-vivo and non-invasive studies of long range connectivity to take place and this with quite simple tools. Technically speaking, various DTI based tractography techniques have been developed over the last few year to tackle the problem (for review see [113]). However a consensus has also emerged that DTI tractography produces artifactual results in critical brain regions. Indeed as DTI measures a low pass approximation, i.e. Gaussian approximation, of the real diffusion function (Section 4.5) in a given voxel, it cannot capture intra-voxel complex architectures and their corresponding multiple diffusion maxima (see Section 4.4). Accordingly the typical crossings that occur in the pons —where axons of the cerebellar peduncles intermix quasi orthogonally with the cortico-spinal tract or posterior columns — and in the centrum semi-ovale — where major crossings occur between callosal fibers, corona-radiata and arcuate fasciculus — cannot be resolved. Pons and centrum semi-ovale are only the most obvious members of brain White Matter (WM) regions where complex intra-voxel fibertract-intermixing occurs.

As we have introduced in Section 4.5 DSI, a diffusion MRI method, that samples without major a priori the diffusion function and accordingly has sufficient angular resolution to map

diffusion of non-Gaussian behavior, hence to see intra-voxel diffusion heterogeneity, caused by crossing fiber tracts.

The present aim is to study how tractography on DSI data resolves the nontrivial fiber architecture. As such we take the brainstem and the centrum-semi ovale as first test case for our algorithm.

## 6.2 Methods

### 6.2.1 MR Acquisition

The diffusion weighted images are acquired on two healthy volunteers with a classical DSI scheme as described in Chapter 4, using 515 diffusion encoding directions. For the first dataset, MR diffusion weighted images of a hemi-brain were obtained with a 3T Allegra scanner (Siemens, Erlangen, Germany). We used a twice-refocused spin echo EPI sequence [128] with  $TR/TE/\Delta/\delta = 3000/154/66/60$  ms,  $b\text{-max} = 17000 \text{ mm}^2/\text{s}$  to acquire 20 slices of a  $64 \times 64$  matrix with a spatial resolution of  $3 \times 3 \times 3 \text{ mm}^3$ . For the second dataset, diffusion weighted images of the brainstem were acquired with a single shot EPI sequence on a Intera 3T Philips scanner with the following timing parameters:  $TR/TE/\Delta/\delta = 3000/100/47.6/35$  ms and  $b\text{-max} = 12000 \text{ mm}^2/\text{s}$ . The acquisition block was made of 24 slices of a  $128 \times 128$  matrix with a spatial resolution of  $2.4 \times 2.4 \times 2.4 \text{ mm}^3$ .

### 6.2.2 Tractography

For DTI tractography the standard procedure is to reduce the diffusion tensor data to a single vector indicating the direction of most important diffusion which corresponds to the main eigenvector of the tensor. Trajectories are then computed by an iterative procedure that follows the field of main diffusion eigenvectors (e.g. [12, 112]).

For DSI tractography, we follow a very similar scheme as in DTI tractography, but we need to take into account the multiple diffusion maxima available in each voxel, so that the matrix diagonalization procedure present in DTI is replaced by a search for local maxima. We use the same notation as in the algorithm presented in Chapter 5, where the discrete trajectory of a particle in 3D space is given by its time varying position vector  $\mathbf{x}_i \in \mathbb{R}^3$ , where  $i$  is the discrete time step that varies from  $-I$  to  $+I$ . The particle generates its trajectory by forward and backward propagation away from the seed point and grows in both directions along a unit vector  $\boldsymbol{\Omega}_i$ , which is the local maximum of the ODF in position  $\mathbf{x}_i$  most collinear to the particle trajectory at time  $i$ . Such trajectories are computed for a large set of seed points that are scattered uniformly over the brain WM (see Algorithm 6.1).

This procedure provides us with a set of lines that can be interpreted as an estimate of the brain axonal trajectories. The data is analyzed, as in Chapter 5, by placing Regions of Interest (ROI) such that all lines not running through the specified ROIs are shielded away.

---

```

1:  $\eta := 0.5$ 
2:  $\mathbf{x}_0 := \text{WMvoxel}$ 
3:  $\boldsymbol{\Omega}_0 := \arg \max_{\mathbf{u}: \|\mathbf{u}\|=1} \{\text{ODF}_{\mathbf{x}_0}(\mathbf{u})\}$ 
4: %backward propagation
5:  $\mathbf{x}_{-1} := \mathbf{x}_0 - \eta \boldsymbol{\Omega}_0$ 
6:  $i = -1$ 
7: while  $\mathbf{x}_i$  in WM do
8:    $\mathcal{D}(\mathbf{x}_i) := \{\mathbf{u} : \text{ODF}_{\mathbf{x}_i}(\mathbf{u}) = \text{local maximum}\}$ 
9:    $\boldsymbol{\Omega}_i := \arg \max_{\mathbf{u} \in \mathcal{D}(\mathbf{x}_i)} \{\mathbf{u} \cdot \boldsymbol{\Omega}_{i+1}\}$ 
10:   $\mathbf{x}_{i-1} := \mathbf{x}_i + \eta \boldsymbol{\Omega}_i$ 
11:   $i = i - 1$ 
12: end while
13: %forward propagation
14:  $\mathbf{x}_1 := \mathbf{x}_0 + \eta \boldsymbol{\Omega}_0$ 
15: while  $\mathbf{x}_i$  in WM do
16:   $i = i + 1$ 
17:   $\mathcal{D}(\mathbf{x}_i) := \{\mathbf{u} : \text{ODF}_{\mathbf{x}_0}(\mathbf{u}) = \text{local maximum}\}$ 
18:   $\boldsymbol{\Omega}_i := \arg \max_{\mathbf{u} \in \mathcal{D}(\mathbf{x}_i)} \{\mathbf{u} \cdot \boldsymbol{\Omega}_{i-1}\}$ 
19:   $\mathbf{x}_{i+1} := \mathbf{x}_i + \eta \boldsymbol{\Omega}_i$ 
20:   $i = +1$ 
21: end while

```

**6.1:** Tractography algorithm for DSI data.  $\eta$  is the step size, chosen to be  $0.5 \times \text{voxel width}$ . The set of time indexed positions  $\mathbf{x}_i$  define the particle trajectory.  $\text{ODF}_{\mathbf{x}_i}$  is the ODF at position  $\mathbf{x}_i$ . The time indices  $i$  are negative for the backward propagation and positive for forward propagation.  $\mathbf{u}$  is a unit vector.  $\mathcal{D}(\mathbf{x}_i)$  is the set of local maxima of the ODF at position  $\mathbf{x}_i$ .  $\boldsymbol{\Omega}_i$  is the trajectory propagation vector.

## 6.3 Results

We studied two brain regions: the pons and the centrum semi-ovale. They are both anatomically well described in the literature [118] and famous for their known complex fiber architecture as both present areas of fiber-crossings.

### 6.3.1 Study of the Pons

In Figure 6.1, we study the relationship between major tracts in the brainstem: the cerebellar peduncles, the medial lemnisci and the cortico-spinal tracts. In order to capture those structures we combined criteria of inclusion and exclusion related to three ROIs. ROI C is a box on the Cerebellum, ROI M a box placed in the Mid-brain and ROI S is a box centered on the most cranial part of the Spinal cord. In Figure 6.1, lines running through ROI M and S highlight the cortico-spinal tract (red) and medial lemnisci (yellow). Superior cerebellar peduncles are identified by lines passing through ROI C and M (white). Mid-cerebellar pe-

duncle is revealed with trajectories running only through ROI C (green), inferior cerebellar peduncle by ROI C and S (cyan). We notice, as we readily know from postmortem anatomy ([118]) that peduncles intermix with cranio-caudal tracts like cortico-spinal tract and medial lemnisci at the level of the pons and mid-brain (Figure 6.2A and B). It is particularly striking for the mid-cerebellar peduncle that has synaptic connections at the level of the pons, precisely in areas where the cortico-spinal tract travels cranio-caudally (Figure 6.2C).

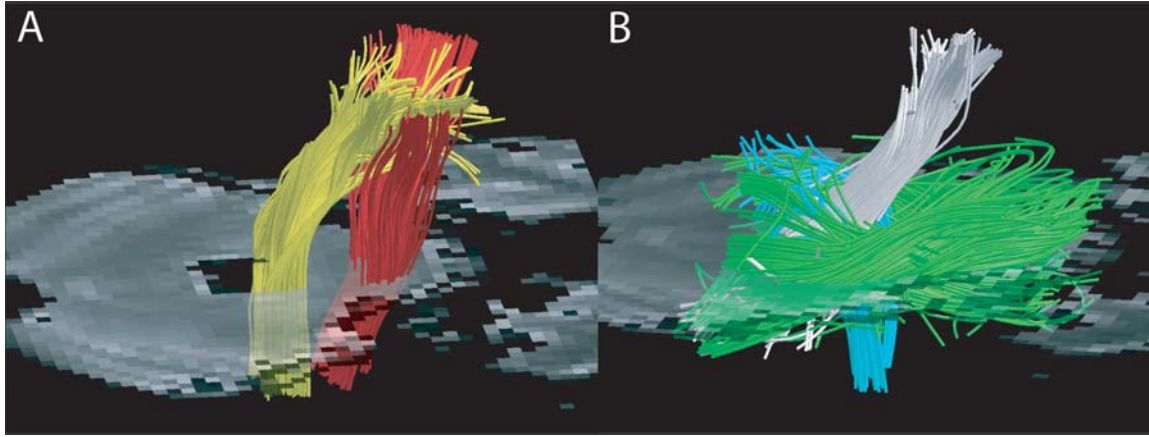


**Figure 6.1:** Major axonal pathways at the level of the pons revealed by DSI tractography. A) Medial lemnisci (yellow) and cortico-spinal tract (red). B) Superior (white), mid (green) and inferior (cyan) cerebellar peduncles

### 6.3.2 Study of the Centrum Semi-Ovale

In Figure 6.3A, the cortico-spinal tract has been mapped by placing two ROIs: one along the motor strip and one in the pons. According to known anatomy ([118]), the lines displayed in red represent the part of the pyramidal tract that starts in the apical part of the precentral gyrus and middle part of the paracentral lobule and correspond to the motor function of the trunk and legs. Whereas the lines in orange, taking their origin between the superior and inferior genu of the central sulcus (i.e. of the precentral gyrus), correspond to the motor fibers for the arm and hand. The callosal fibers (Figure 6.3B in green) passing in the region of the centrum semi-ovale are visualized by placing a ROI in the parietal cortex and one in the mid-sagittal plane centered on the corpus callosum. One can see that the fibers of the corpus callosum are widely distributed throughout the parietal cortex from the apex down to its lower limit at the lateral sulcus. The superior longitudinal fasciculus (Figure 6.3C in blue) has also been rendered in order to show the complex intermixing of several fiber populations that occur in the centrum semi-ovale (Figure 6.3D).

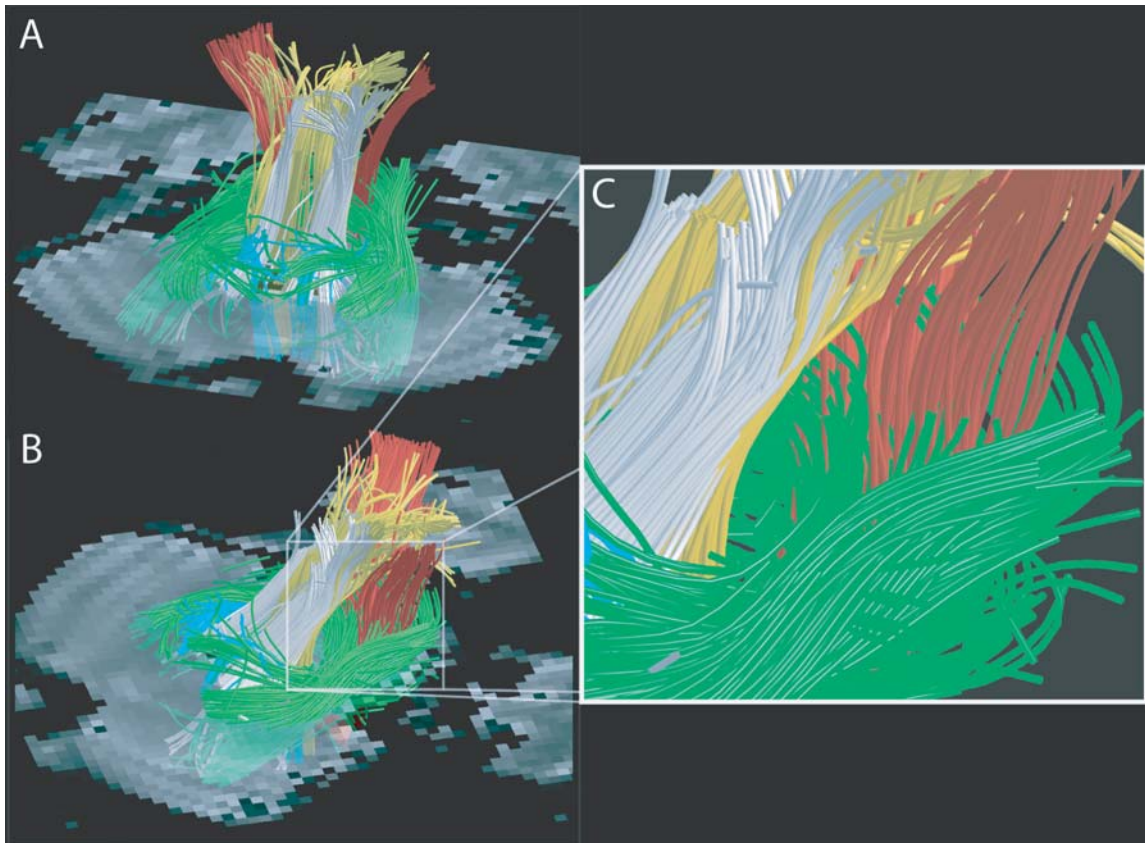


**Figure 6.2:** Complex fiber architecture in the pons mapped by DSI tractography. A) and B) display the global relationship of major tracts in the pons as the Medial lemnisci (yellow), cortico-spinal tract (red), Superior (white), mid (green) and inferior (cyan) cerebellar peduncles. C) Zoom on the pons where cortico-spinal tract and mid cerebellar peduncle cross.



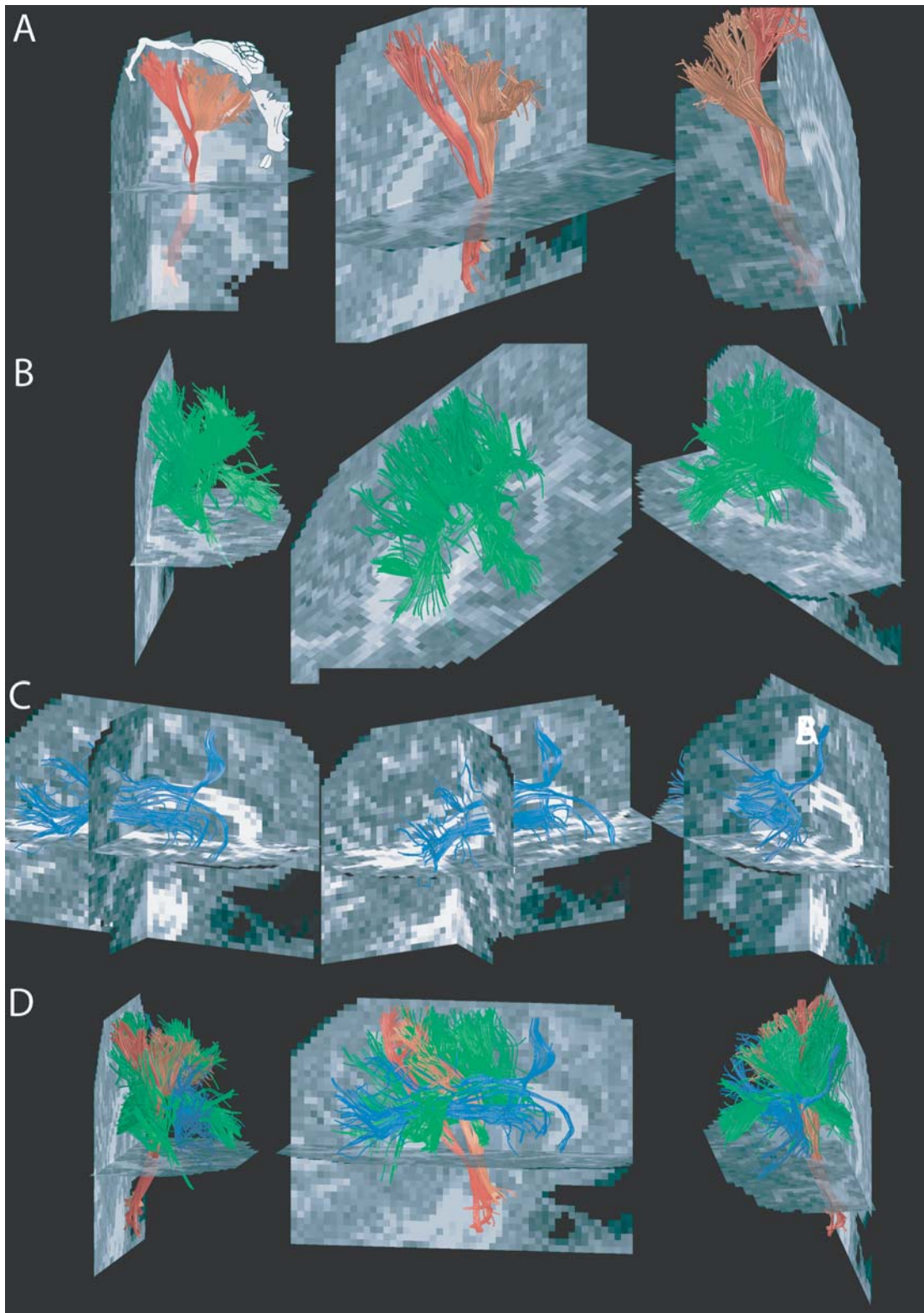


**Figure 6.3:** Complex fiber architecture in the centrum semi-ovale mapped by DSI tractography. A) The lines corresponding to the cortico-spinal tract are in red for the motor function of the trunk and legs and orange, for the arm and hand. B) In green, mid corpus callosum with its apical (dark green) and lateral (light green) projections. C) Superior longitudinal fasciculus in blue.

## 6.4 Discussion

Diffusion MRI tractography turns out to be a more difficult problem than first expected. Around last century change, as the first papers on DTI tractography were published (examples: [12, 39, 86, 112, 143] and example of review [113]), there was a great and legitimate enthusiasm about the foreseen ability of MR to map axonal trajectories in-vivo. But quickly important artifacts, as presented in the introduction, were recognized, tempering the initial expectations. Although many elaborate variants of the basic path integral algorithms [65, 69, 92, 96, 125] have been developed, one is forced to admit that, if the data do not provide sufficient information for a precise reconstruction, the task remains very challenging and up to now not fully solved.

The presented procedure aims at improving tractography by using better raw data than DTI (Chapter 4.4). To show that DSI based tractography is less subject to artifacts we have investigated with a simple algorithm critical regions. As such we used as test case the two most prominent areas where major fiber bundles cross, the brainstem and the centrum semi-ovale and showed that DSI tractography enables to reconstruct accurately the related fiber bundles.

Still limitations of DTI as well DSI exist and should be well understood. As readily mentioned in Chapter 4, in order for DTI tractography to be able to map accurately axonal trajectories it would potentially need to resolve individual fascicles of axons and therefore need micrometric resolution. DSI overcomes this limitation, by resolving variously oriented fascicles in within a voxel, and therefore requires "only" sufficient spatial resolution as to limit intra-voxel dispersion of fiber orientations produced by bend, splay and twist. However, because neural tracts consist of multi-cellular fascicles of tens of microns in diameter that may have very irregular trajectories and strong interdigitation, at some stage both techniques are limited by SNR.

Consequently the user of those techniques must be aware of multiple artifacts and must be educated to interpret the data in a critical sense with the help of its neuro-anatomical knowledge. Maybe semantics should also be adapted to clearly state the difference between true axonal trajectories and the measured, computer generated, fibers or lines. This would emphasize that on one hand there is biological tissue and on the other something that should be interpreted as a new type of diffusion contrast (like are the ADC or the FA). Indeed these computer generated lines capture nothing more than coherent diffusion, in the same sense than streamlines capture coherent flux of a fluid velocity map.

When considering the results showed at the level of the brainstem one might argue that, though being quite illustrative of the intra-voxel fiber-crossing problem, the practical implications are probably limited. However this affirmation can no longer hold for the centrum semi-ovale, which is an immensely important region, not only because axonal projections of major functional systems, like language networks (see Chapter 8), motor and sensory pathways of the limbs, and inter-hemispheric networks, lie in that zone, but also because precisely the centrum semi-ovale is a common location of pathology, like stroke and neoplasm [155]. Therefore it is of major interest for neurosurgery and neuro-diagnostics to

make precise maps of this region available.

Despite the recognized artifacts and resolution limitations, DSI tractography, as well as other diffusion MRI tractography techniques, are foreseen to contribute significantly to the extension of our knowledge not only on normal WM axonal architecture, but also on the global connectivity pattern of the human brain. It is a unique technique that allows us, in one shot and in-vivo, to measure brain WM connections in a comprehensive fashion by performing whole brain simulations. Unfortunately DSI acquisition is for the moment very time consuming, which would limit its clinical use to only local brain studies, for example on the cortico-spinal tract before surgery.

One can also recognize the use of DSI tractography as a validation tool of sophisticated and well engineered DTI tractography tools as it is able to "see" where DTI is blind and as it is able to identify the locations where DTI data must be interpreted with care. These regions are typically those where the diffusion function is multimodal and its kurtosis high (Section 4.5).

Finally, this tractography algorithm was specifically tested on DSI data, but might also be used on other types of high angular resolution diffusion MR images, like q-ball [151] or PAS [82] as long as a ODF map is available.

## 6.5 Conclusion

We have investigated the reconstruction quality of a simple tractography algorithm designed for DSI data. We used as test, the two most prominent brain regions of crossing fiber bundles, the brainstem and the centrum semi-ovale. Whereas standard DTI tractography tools fail in those regions we show that DSI based tractography enables accurate reconstruction of the complex fiber intermixing. We discussed its potential applications for the study of the global connectivity pattern of the brain as well as in neuro-diagnostics and neurosurgery. Potential limitations and artifacts were also considered.



---

# Tractography by Segmentation in Position Orientation Space

---

# 7

*Within every man and woman a secret is hidden, and as a photographer it is my task to reveal it if I can.*

Karsh of Ottawa

## 7.1 Introduction

Classically, the question of finding fibers in the brain, based in diffusion weighted MR images, is addressed by building lines of coherent diffusion that are interpreted as axonal trajectories (see Section 6.4). It is usually achieved by solving some path integral in a field of principal diffusion vectors for various initial starting positions or seeds. If the anatomy of a tract or bundle of fibers needs to be described, it is then displayed as a set of those lines that share some geometrical property, like having similar orientation [26] or being closely located [83]. But, a fiber tract is not only a set of axons, it can also be seen as a single object with a given shape and volume in which diffusion is coherent. For example, the arcuate fasciculus is a semi-toric or crescent shaped object with a volume that depends on gender, handedness and the hemisphere considered (Chapter 8). One might directly be interested in quantifying such geometrical characteristics or one would like to quantify diffusion anisotropy or magnetization transfert in a specific and local tract pathology [50, 52, 89, 103, 106].

Object identification in images is a classical and well studied subject in image processing. Objects are usually defined as connected regions defined by homogeneity criteria such as homogenous intensity. This basic idea has been applied to DTI data by Zhukov et al. [170] in order to separate the WM from the remaining GM and CSF, however as orientational information of the DT is not used, no specific tract can be identified with such method. More

recently Jonasson et al. [84] have incorporated orientational information of DTI data to sub-segment brain WM into main cores of non-overlapping fiber tracts by a three-dimensional geometric flow algorithm. Consequently the brain could be segmented into separate fiber regions, which is a first step in WM region identification. But at the same time the method is unable to represent WM regions of crossing tracts. The typical example is the cortico-spinal tract and corpus callosum, obviously two separate objects, that at the level of the centrum semi-ovale, overlay in three-dimensional space. The limitations are twofold. First DTI does not provide sufficient angular resolution to resolve crossing fiber populations and secondly formulating the segmentation problem in 3D Euclidian space is unnatural as the objects looked for are entangled in such a representation. In other words, 3D Euclidian space does not possess the adequate topology to address this issue.

We have seen that the advent of high angular resolution diffusion MRI data enables tractography to handle naturally fiber trajectories in regions of fiber-crossing. The reason being that at every 3D-voxel one can associate several diffusion orientational maxima. High angular resolution diffusion MRI allows also, as we are going to show, to reformulate tractography as a segmentation problem in a five-dimensional position-orientation space. Accordingly it can be addressed with classical image segmentation approaches, where fiber tracts are represented as disjoint clusters. We will see how this formulation disentangles crossing fiber tracts quite naturally.

In the next section, we propose to mathematically define the Position-Orientation Space (POS) in order to give a precise definition of a neighborhood in this space. It will be used in the segmentation task based on a Markov Random Field (MRF) model in Section 7.2.2.

## 7.2 Theory

### 7.2.1 What is Position-Orientation Space?

In high angular resolution diffusion MRI, as for example DSI [160], diffusion in every voxel is represented with an ODF (definition in Section 4.3). The ODF is a function that measures an intensity of diffusion for any direction of space. Accordingly, the image, i.e. diffusion MRI data, can be seen as a function not only of the usual position vector  $\mathbf{r}$  in 3D Euclidean space, but also of the diffusion direction, which can be defined by a unit vector  $\mathbf{u}$  representing a position on the two-dimensional sphere. Naturally, it arises a space of *position* and *orientation* of variables  $(\mathbf{r}, \mathbf{u})$ , that we call POS.

It is trivial to mention that this newly defined space is not Euclidian, but it is less trivial to define its topology, which is what we have to study first. Instead of studying POS in its continuous formulation and then discretize at the level of the implementation, we take the option of specifying at first POS as a discrete space. This choice keeps the formalism closer to the implementation and has the advantage of fitting directly the segmentation paradigm we have chosen, which is inherently discrete. Its continuous equivalent can however be obtained with a similar construction.

We start by considering a set  $\mathcal{S}$  of sites  $s$  such that:

$$\mathcal{S} = \left\{ s = (\mathbf{r}, \mathbf{u}) : \mathbf{r} \in \mathbb{Z}^3, \mathbf{u} \in \{N \text{ elements uniformly distributed over the 2D unit hemi-sphere}\} \right\}. \quad (7.1)$$

We define the function:

$$\delta(s, s') = \sqrt{\|\mathbf{r} - \mathbf{r}'\|^2 + \gamma(\arccos|\mathbf{u} \cdot \mathbf{u}'|)^2}, \quad (7.2)$$

where  $\gamma$  is a constant that weights the angular distance as compared to the Euclidean distance. In the sequel we choose arbitrarily  $\gamma = 18/\pi$ , which makes a unit of angular distance equal to  $10^\circ$ .

We notice that the function  $\delta(\cdot, \cdot)$  is a metric since it satisfies the three basic properties of symmetry and identity condition and the triangle inequality [116]. Hence, the metric  $\delta$  induces a topology on the metric space  $\mathcal{S}$ , whose closed sets over all subsets can be realized as the intersection of closed balls defined as:

$$\mathcal{B}_\rho(s) = \{s' : \delta(s, s') \leq \rho\}, \quad (7.3)$$

with  $s \in \mathcal{S}$  and  $\rho \in \mathbb{R}^+$ .

From now on we define a *neighborhood* in the metric space  $\mathcal{S}$  that will be used in the segmentation model presented in Section 7.2.2. The neighborhood of a site  $s \in \mathcal{S}$  is chosen as follows:

$$\mathcal{N}_s = \mathcal{B}_1(s) \setminus \{s\}. \quad (7.4)$$

The set  $\mathcal{N} = \{\mathcal{N}_s\}_{s \in \mathcal{S}}$  defines a *neighborhood system* for  $\mathcal{S}$  since it satisfies the two properties [61, 62]:

1.  $s \notin \mathcal{N}_s, \forall s \in \mathcal{S}$ ,
2.  $s \in \mathcal{N}_{s'} \Leftrightarrow s' \in \mathcal{N}_s, \forall (s, s') \in \mathcal{S}^2$ .

In order to get some intuition on this POS, let us consider the problem in two dimensions instead of three, hence defining a 3D POS instead of the actual 5D POS. As depicted in Figure 7.1A, we consider two fibertracts (yellow and red) that cross at  $\approx 30^\circ$  in the x-y plane. The underlying diffusion pattern is represented by the ODF map in the same plane. We see that in the crossing areas the ODFs exhibit two directional maxima tangent to both fiber tracts. In Figure 7.1B, where we have isolated both individual tracts, we readily see that they overlap in the middle of the image. We now add a third dimension, which we call  $\theta = \arccos|\mathbf{u} \cdot (1, 0)|$  that codes for the angular variable of the ODF with reference to the x axis. Intuitively, we define this space as the 3D POS. The ODFs of Figure 7.1A are then mapped as a scalar field  $d(x, y, \theta)$  of diffusion intensity on 3D POS. The green interfaces of Figure 7.1D represent isosurfaces\* of the scalar field. Whereas both tracts where overlying structures in two dimensions (Figure 7.1 A-B), we see that in 3D POS they

---

\*isosurface  $\triangleq \{s \in \mathcal{S} : d(s) = \text{constant}\}$

nicely disentangle. At this stage we would just like to raise to the reader's attention that for representation purposes the 3D POS *looks* Euclidean, but by no means it is, as there is periodicity along  $\theta$ .

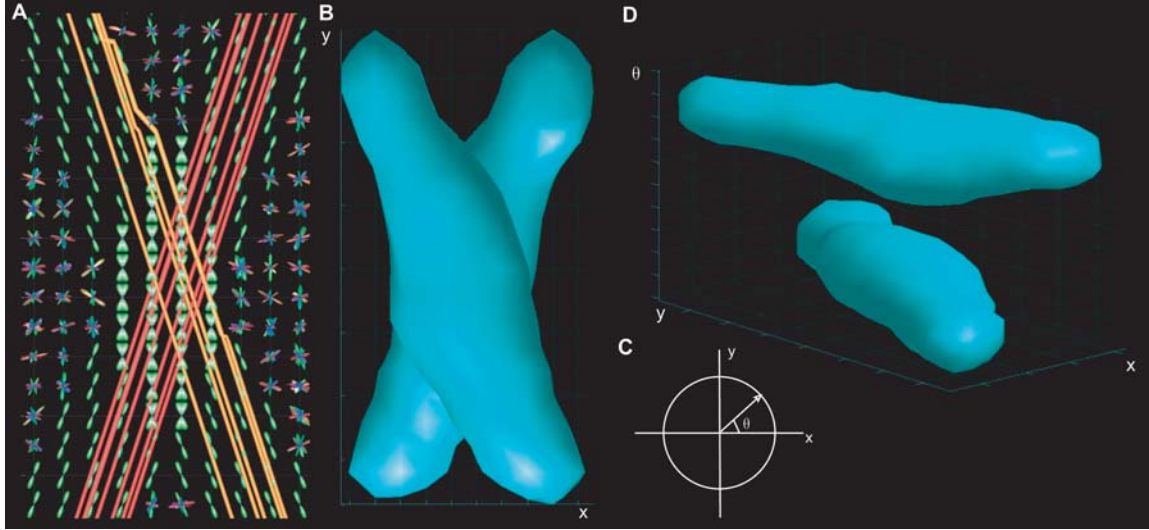


**Figure 7.1:** Model of crossing fiber tracts in two dimensions. A) ODF map of 2 crossing fiber tracts at  $\approx 30^\circ$  in the plane. B) In two dimensions the region of fiber-crossing is shared by both tracts, the two objects, are entangled. C)  $\theta$  defines the orientation of the diffusion by which the ODF is parameterized. The ODF is maximum for an angle that corresponds to the fiber tangent. D) 3D POS, where the third dimension codes for the angular orientation of diffusion. Accordingly the ODF map is mapped into a scalar field  $d(x, y, \theta)$ . The tract representation in this space is captured by a green isosurface. We readily see that as both tracts do not have their maximal diffusion in the same orientation and therefore disentangle in POS.

### 7.2.2 Segmentation of POS in Two Classes

In POS tracts lie in regions where the scalar field  $d(\mathbf{r}, \mathbf{u})$  takes high values, whereas areas where no fibers are present exhibit low diffusivity. The aim of the segmentation task is to label every POS-pixel as "1" if it corresponds to a position inside a tract or with "0" if it lies outside. Now we are able to make the link with classical image segmentation formulations. The Markovian approach in image denoising and segmentation, first introduced by Geman and Geman [61, 62], is powerful and now a widely accepted paradigm. It has the immense advantage of providing lots of flexibility while keeping implementation simple. Practically, we derive our formulation from the Markov Random Field Maximum A Posteriori (MRF-MAP) classification algorithm proposed by Zhang et al. [169] that was designed to segment T1 weighted MRI images. We reformulate the neighborhood system in accordance to the peculiar topology of POS and the energy functions in order to fit our image model.

Let us consider the discrete scalar field reconstructed from the MRI data:

$$\begin{aligned}\mathcal{S} &\longrightarrow \mathcal{D} \\ (\mathbf{r}, \mathbf{u}) &\longmapsto d(\mathbf{r}, \mathbf{u}),\end{aligned}$$

as a realization  $\mathbf{y}$  of some random field  $\mathbf{Y}$  which models the random variable generating the MRI derived data.  $\mathbf{Y}$  is the *observed random field*, and it takes its values in the configuration space:

$$\mathcal{Y} = \{\mathbf{y} = (y_1, \dots, y_{|S|}) : y_s \in \mathcal{D}, s \in S\} \quad (7.5)$$

Where  $\mathcal{D} = \{0, 1, \dots, D\}$  is the phase space of the diffusion scalar field \*.

We furthermore consider a random field  $\mathbf{X}$  taking its values in the configuration space:

$$\mathcal{X} = \{\mathbf{x} = (x_1, \dots, x_{|S|}) : x_s \in \mathcal{L}, s \in S\}, \quad (7.6)$$

with  $\mathcal{L} = \{0, 1\}$ . Each configuration  $\mathbf{x}$  represents an indicator map of fibertracts, where positions with fibertract take value "1" and position free of tract value "0". We call  $\mathbf{X}$  the *hidden random field* as it is not directly observable, but as we will see can be guessed from a realization of the observed field  $\mathbf{Y}$ .

Obviously  $\mathbf{X}$  is not independent of  $\mathbf{Y}$  and  $X_s$  is not independent of its neighborhood, let us formalize these concepts. We consider that there is a local spatial correlation in  $\mathbf{X}$ , property that can be modelled by a Markov Random Field (MRF). Accordingly, a neighborhood system must be defined. We naturally use the system that we defined in Section 7.2.1 to generate the POS:  $\mathcal{N}$ . It follows that the local characteristic of  $\mathbf{X}$  can be expressed as:  $p(x_s | x_{S \setminus s}) = p(x_s | x_{\mathcal{N}_s})$ . Furthermore, we specify the relation between  $\mathbf{X}$  and  $\mathbf{Y}$  by assuming that these random fields are related in the following fashion:

$$p(\mathbf{y} | \mathbf{x}) = \prod_{s \in S} p(y_s | x_s), \quad (7.7)$$

which states that conditionally to a given configuration  $\mathbf{x} \in \mathcal{X}$  the random variables  $Y_s$  are independent.

The image classification problem we consider involves assigning to each POS-pixel a class label belonging to the set  $\mathcal{L}$ . We look for the true but unknown configuration  $\mathbf{x}$  that has generated the observation  $\mathbf{y}$ .  $\mathbf{x}$  can be estimated by maximizing the probability  $p(\mathbf{x} | \mathbf{y})$ . According to the Maximum A Posteriori (MAP) criterion, this objective can be formalized with the following optimization task, by supposing  $p(\mathbf{y})$  constant:

$$\hat{\mathbf{x}} = \arg \max_{\mathbf{x} \in \mathcal{X}} \{p(\mathbf{y} | \mathbf{x})p(\mathbf{x})\}, \quad (7.8)$$

where  $\hat{\mathbf{x}}$  is the best estimate given the observation  $\mathbf{y}$ .

According to the Gibbs-Markov equivalence (p. 260 [23]) and more particularly to the Hammersley-Clifford theorem [71], the distribution of a MRF can be expressed as a Gibbs distribution. Hence

---

\*we assume  $d(\mathbf{r}, \mathbf{u})$  to be a discrete valued function

$$p(\mathbf{x}) = \frac{1}{Z} e^{-U(\mathbf{x})}, \quad (7.9)$$

where the energy function  $U$  derives from a Gibbs potential (p. 258 [23]) and  $Z$  is a normalizing constant called the partition function.

Furthermore because of the conditional independence stated above Eq. (7.7), it is always possible to write  $p(\mathbf{y}|\mathbf{x})$  as a Gibbs distribution:

$$p(\mathbf{y}|\mathbf{x}) = \frac{1}{Z'} e^{-U(\mathbf{y}|\mathbf{x})}. \quad (7.10)$$

Consequently this is equivalent to minimizing the negative log-likelihood of the Eq. (7.8):

$$\hat{\mathbf{x}} = \arg \min_{\mathbf{x} \in \mathcal{X}} \{U(\mathbf{y}|\mathbf{x}) + U(\mathbf{x})\}. \quad (7.11)$$

Gibbsian distributions give us considerable flexibility for shaping the probabilistic relationships between the individual components of random fields. As such we choose convenient and easy to implement potentials in the definition of the energy functions.

We model the conditional energy as

$$U(\mathbf{y}|\mathbf{x}) = \alpha \sum_{s \in \mathcal{S}} U_s(y_s|x_s) \quad (7.12)$$

$$= \alpha \sum_{s \in \mathcal{S}} \{(y_s - t)\mathbf{1}_{[x_s=0]} + (t - y_s)\mathbf{1}_{[x_s=1]}\}, \quad (7.13)$$

where  $0 < t < 1$  is a threshold that is experimentally chosen,  $\mathbf{1}_{[\cdot]}$  is the indicator function, taking value 1 if the statement in brackets is satisfied and 0 otherwise;  $\alpha$  is a tuning parameter that is chosen to be 1. These potentials  $U_s(y_s|x_s)$  are made to favor the state "fibertract = 1" in regions of high diffusivity and reversely favor the state "no-fibertract = 0" in regions of low diffusivity.

For the prior energy function we chose potential functions that favor homogeneous regions:

$$U(\mathbf{x}) = \beta \sum_{s \in \mathcal{S}} U_s(x_s|x_{\mathcal{N}_s}) \quad (7.14)$$

$$= \beta \sum_{s \in \mathcal{S}} \left\{ \frac{1}{|\mathcal{N}_s|} \sum_{r \in \mathcal{N}_s} \mathbf{1}_{[x_r \neq x_s]} \right\}, \quad (7.15)$$

where  $\beta$  is a tuning parameter set to 1 and  $|\mathcal{N}_s|$  the cardinality of the neighborhood of  $s$ , defined in Section 7.4.

Although mathematically simple this type of MAP problem can be computationally difficult because of combinatorial explosion. We use the Iterative Conditional Modes (ICM), algorithm proposed by Besag [17], that uses a "greedy" strategy by performing local minimization iteratively and is known to converge after only a few iterations.

### 7.2.3 Fibertract Labelling

By definition two separate fibertracts are two clusters in the optimized configuration  $\hat{\mathbf{x}}$  that are disjoint with respect to the neighborhood system. Therefore to finalize the segmentation, we use an iterative algorithm that scans  $\hat{\mathbf{x}}$  and labels the separate clusters uniquely.

## 7.3 Material

The diffusion weighted images are acquired with a classical DSI scheme as described in Chapter 4. The acquisition was performed on a 3T Philipps scanner with the following timing parameters:  $TR/TE/\Delta/\delta = 3000/154/47.6/35$  ms and  $b\text{-max} = 12000\text{mm}^2/\text{s}$ . We imaged 2 healthy volunteers. On the first we did a brainstem study where we acquired a block of  $128 \times 128 \times 24$  voxels at a spatial resolution of  $2.4 \times 2.4 \times 2.4 \text{ mm}^3$ . On the second volunteer we acquired 5 coronal brain slices of  $128 \times 128$  voxel with a resolution of  $2 \times 2 \times 3 \text{ mm}^3$ . In every voxel the data was reconstructed according to Chapter 4 by taking in every voxel the FT of the modulus of the q-space signal. An ODF map is built by radial projection of the diffusion spectrum.

## 7.4 Results

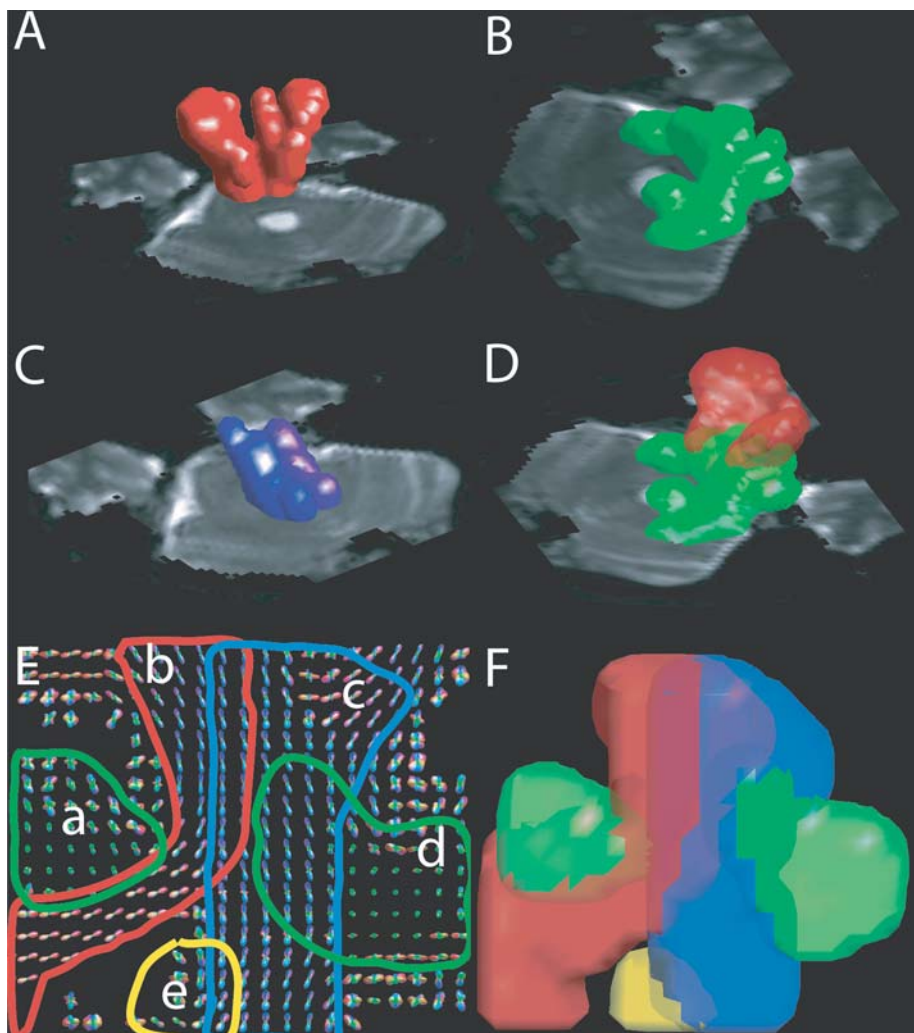
Figure 7.2 A-D displays results based on the brainstem acquisition. On Figure 7.2A we can see the segmented corticospinal tract (CST) in red. Figure 7.2B shows the mid-cerebellar peduncle (MCP) and Figure 7.2C both superior cerebellar peduncles (SCP). In Figure 7.2D we see how the CST and MCP cross in the pons and how they share partly the same volume in 3D space. Figure 7.2E-F correspond to the coronal acquisition centered on the centrum semiovale. Figure 7.2E is an ODF map in this area on which manually we have drawn lines around objects of interest. a) is the cingulum (green), b) the callosal fibers (red), c) the CST (blue), d) the arcuate fasciculus (green) and e) is a part of the thalamus (yellow).

Figure 7.2F is the segmentation result of the centrum semi-ovale and we can appreciate how the different structures have been identified. We see again how different structures share partly the same 3D volume as their surrounding surfaces overlap. For example, it is clear that the arcuate fasciculus crosses the CST (i.e. blue and green surface). The same observation is valid for the cingulum and the callosal fibers (red and green surface) as well as CST and callosal fibers.

## 7.5 Conclusion

We have seen that fibertract identification can be formulated as a classical image segmentation problem; however because of the topological structure of the objects of interest it is necessary to perform the segmentation in a space that provides sufficient freedom in order to separate them. At first sight, the naturally occurring POS seems optimal for this task and the results show how nicely one can identify crossing fibertracts. However, the





**Figure 7.2:** Position Orientation Space segmentation in-vivo. A-D) The brainstem stem has been segmented in A) the cortico-spinal tract (red), B) the mid-cerebellar peduncle (green), C) the superior cerebellar peduncle (blue). D) displays the overlap of the cortico-spinal tract and mid-cerebellar peduncle at the level of the pons, region where precisely these two fiber-tracts cross. E-F) The cingulum, the arcuate fasciculus (green), the cortico-spinal tract (blue), the corpus callosum (red) and a part of the thalamus (yellow), schematically drawn on a coronal slice E) have been segmented and displayed in F).



---

method readily raises an other difficulty which does not seem to be readily solved by POS; kissing fibers overlap in this space as well. Considering its limits, the proposed method is a convenient tool for partitioning the brain WM in anatomically interpretable components, which might prove to be useful to analyze shapes and volumes of such objects. It will also allow to perform quantitative measurements, like fractional anisotropy (examples: [49, 50, 89, 106, 114, 147]), magnetization transfer (example: [51]), in meaningful regions of interest .



## Part III

# Human Brain Neuronal Network Topology



---

# Hand Preference and Gender Shape the Architecture of Language Networks

---



*À chacun son cerveau.*

F. Ansermet and P. Magistretti

## 8.1 Introduction

Language comprehension and production rely critically on left hemispheric networks, including Broca's area, which contributes to language production and is located in the opercular part of the inferior frontal gyrus (oIFG), and Wernicke's area, which contributes to language comprehension and is located in the planum temporale and the posterior part of the superior temporal gyrus (pSTG) [43, 63, 108]. Activation studies suggest that left hemispheric dominance for language processing is less strong in women than in men [81, 133] and in left- (LH) than right-handers (RH) [127, 153].

Matching the functional asymmetry, Broca's [47, 54] and Wernicke's areas (e.g. [58]) were found to be larger on the left side. Sex and handedness appear to influence the degree of anatomical asymmetry; in Wernicke's area it was reported to be smaller in LH than in RH [53, 111, 137] and in women than in men [64].

Relatively little is known about the organization of speech areas. They are believed to be part of a wide-spread neural network, but only small parts of its connectivity have been demonstrated anatomically [41]. The intrinsic organization of speech areas has been investigated histologically. The morphology of the main cortical output neurons, the pyramids [80, 132] and the spacing of long-range intrinsic connections [60] was found to be somewhat different between Wernicke's area and its right homologue. Broca's area was found to have a greater neuronal density than its homologue, especially in men [4]. These differences are

likely to be accompanied by differences in long distance connectivity, which has, however, never been systematically investigated.

We report here on the connectivity of Broca’s and Wernicke’s areas and their right hemisphere homologues, as visualized with DT-MRI tractography [69] in RH and LH men and women.

## 8.2 Methods

We investigated 32 subjects: 16 men (mean age  $\pm$ SD:  $34.0 \pm 7.9$ ) with 8 RH and 8 LH and 16 women (mean age  $\pm$  SD:  $29.2 \pm 6.2$ ) with 8 RH and 8 LH. Handedness was defined according to the Edinburgh-Oldfield inventory [119], ranging from -10 to +10, with positive and negative scores representing RH and LH respectively. Mean handedness score and SD for the respective groups were: RH women =  $9.4 \pm 1.2$ , RH men =  $7.0 \pm 2.1$ , LH women =  $-6.5 \pm 3.2$  and LH men =  $-6.4 \pm 2.6$ . This research was conducted in agreement with the Code of Ethics of the World Medical Association (Declaration of Helsinki) and informed consent was obtained from all subjects before performing the study, in accordance with institutional guidelines. For each of the 32 subjects, we acquired at 1.5T:

1. two fMRI studies acquired with a single shot gradient-echo EPI sequence (TR = 15 s for the sentence comprehension task and 5 s for the word generation task, 16 slices, slice thickness 5 mm, gap 1 mm, TE = 66 ms, FoV = 270x270 mm<sup>2</sup>, matrix size 128x128, flip angle 90°),
2. a DT-MRI dataset based on a single-shot EPI sequence (TR/TE = 1000/89 ms, 44 contiguous slices of 3 mm of thickness, FoV = 210x210 mm<sup>2</sup>, matrix size 128x128) acquired along 6 diffusion sensitizing directions with a b-value=1000 s/mm<sup>2</sup>, and
3. a sagittal T1-weighted 3D gradient-echo sequence (128 contiguous slices, slice thickness 1.25 mm, FoV = 250x250 mm, matrix size 256x 256).

The two fMRI studies consisted in a sentence comprehension paradigm (subjects were asked to detect errors while listening to a random sequence of grammatically correct or incorrect sentences), and in a silent word generation paradigm. Both studies were organized according to a block design. These two functional studies were used to map in each subject areas related to speech processing, and in particular pSTG and oIFG. fMRI data analysis was performed with SPM2 (The Wellcome Department of Cognitive Neurology, London, UK).

DT-MRI datasets were used as input for a fibertracking method, described in detail in Chapter 5. We remember that the tracking algorithm generates a set of lines or fibers that are driven by the local diffusion properties and a regularity constraint. Such extensively initiated fibers over all the white matter (as defined by a threshold fractional anisotropy map at 0.2) are grown until reaching the white matter mask boundary. The large set of fibers (several hundred thousands) thus generated provides an estimate of axonal trajectories throughout the brain.

The fibertracts of interest were selected through a pair of ROIs (Figure 8.1), which in this study were based on the fMRI activations. The four local maxima in the t-score activation maps of the corresponding language comprehension and production fMRIs were automatically identified and named target points. They gave us the position of the left and right pSTG and oIFG. In a few cases, where there was no right oIFG activation, the target point was placed according to the contra-lateral activation and placed in the homologous cortical location. We used these four target points as starting points for a geodesic region growing algorithm that evolves in the white matter mask. The four regions thus defined were our ROIs. They follow local white matter configuration and have equal volumes. The fiber selection was done by retaining the fibers that had one extremity in each chosen ROI.

White matter volume  $V_{WM}$  was estimated by measuring the volume of the fibertracking mask, which is a fractional anisotropy map thresholded at 0.2. The mid-sagittal callosal surface  $S_{CC}$  is measured in the mid-sagittal plane of the same mask. The statistics were always performed with either a one-way or two-way ANalysis Of VAriance test (ANOVA). The significance threshold for null hypothesis rejection was set to  $\alpha = 0.05$ .

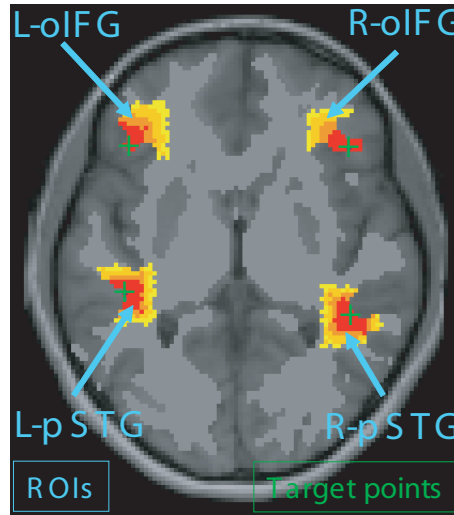


**Figure 8.1:** Schema of the ROIs. The green crosses represent the target points which are identified by the local maximum of the related fMRI activation. The red to yellow regions define the ROIs that have been generated by a geodesic region-growing algorithm; all four ROIs have the same volume.

### 8.3 Results

We visualized by DT-MRI tractography the axonal connectivity between Wernicke's and Broca's areas and their right hemisphere homologues, i.e. between left and right pSTG and oIFG (Figure 8.2). In each individual subject, Wernicke's area was identified by its fMRI activation in a sentence recognition paradigm, and its right hemisphere homologue either as a smaller activation focus in the same task or as the homotopic location. Broca's area

and its homologue were identified in a similar fashion by their activation in a silent word generation paradigm. Isovolumic Regions Of Interest (ROI) adapted to the cortical shape were defined in these four locations and axonal connectivity between pairs of ROIs was quantified using a probabilistic whole brain fibertracking method [69] (see Fig. 8.3).

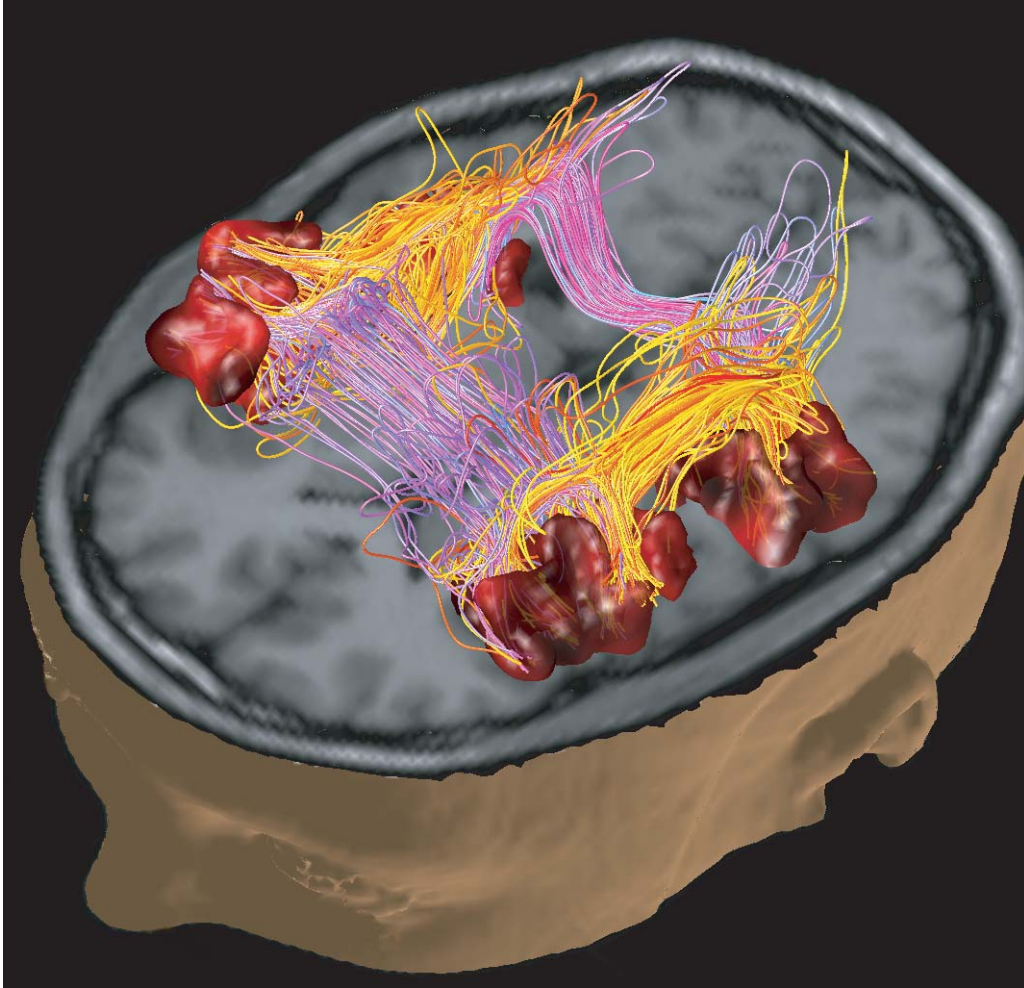


**Figure 8.2:** 3D rendering of language network. The red surfaces mark the cortical gray matter adjacent to the 4 ROIs located in the left and right pSTG and oIFG. These ROIs, of identical white matter volume, have been generated by a geodesic region growing algorithm so that they follow the brain conformation. They are initialized at the local maximum of the fMRI activations related to language comprehension or production (see text). Yellow-red denotes intrahemispheric connections, magenta-blue inter-hemispheric. The latter crossed in the body of the corpus callosum when linking both oIFG, or in the isthmus for the pSTG.

### 8.3.1 Intra-hemispheric connectivity

The intra-hemispheric connections between pSTG and oIFG formed a loose bundle, that we call the pSTG-oIFG bundle, which was very reminiscent of the arcuate fasciculus revealed



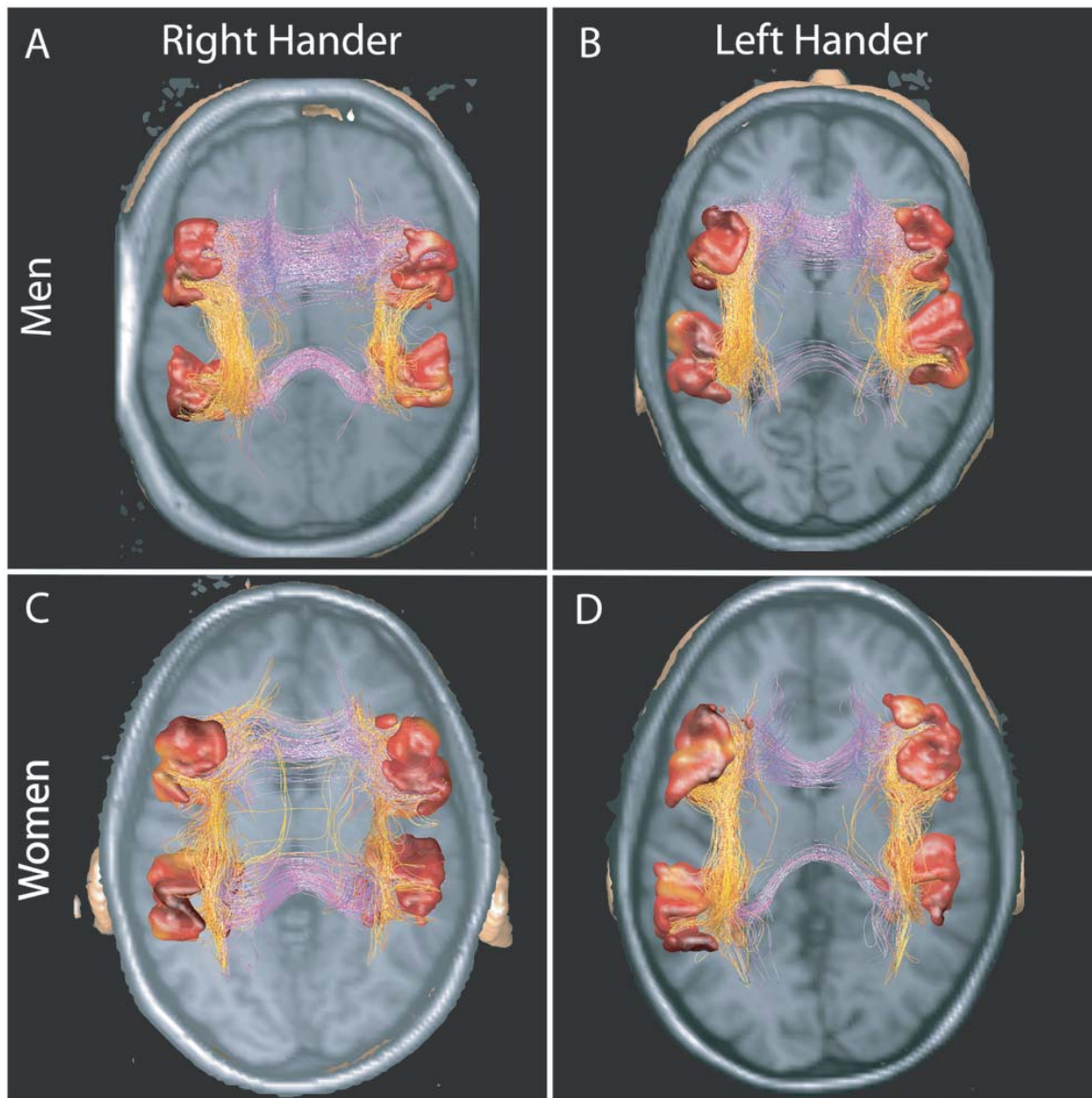


**Figure 8.3:** Superior view of a T1-weighted horizontal MRI slice. The red surfaces mark the cortical gray matter adjacent to the 4 fMRI identified ROIs located in the left and right pSTG and oIFG. Yellow-red denotes intrahemispheric connections, magenta-blue inter-hemispheric. The latter crossed in the body of the corpus callosum when linking both oIFG, or in the isthmus for the pSTG. (A) RH men presented typically a marked asymmetry in the pSTG-oIFG bundle, with more fibers in the left hemisphere. Posterior inter-hemispheric connections were numerous. (B) LH men presented typically little asymmetry in the pSTG-oIFG bundle. The posterior inter-hemispheric connections were sparse. (C) RH and (d) LH women had similar connectivity patterns, i.e. strong intra- and inter-hemispheric connectivity.

by tracing studies in non-human primates [122].

In many, but not all subjects, the pSTG-oIFG bundle tended to have more fibers on the left than on the right side. Connective Lateralization Index was defined as:  $cLI = \log[(1 + Q)/(1 - Q)]$  which is the Fisher Z-transform of the quotient  $Q = (N_L - N_R)/(N_L + N_R)$ ,  $N$  being the number of fibers that run between pSTG and oIFG, left ( $L$ ) and right ( $R$ ). A positive value for cLI means a lateralization towards the left (i.e. the pSTG-oIFG connectivity is stronger left than right), negative values meaning the opposite and zero being ambilaterality. By means of this measure, we investigated the effect of handedness and gender on the lateralization of the pSTG-oIFG bundle. One way analysis of variance (ANOVA) showed that RH men were significantly more lateralized towards the left than LH men ( $F(1, 14) = 6.9504, p < 0.05$ ). Women presented little asymmetry in the pSTG-oIFG connection density, which was not statistically significant between RH and LH ( $F(1, 14) = 0.5545, p > 0.05$ ). A two-way ANOVA combining the handedness and gender showed a significant interaction between both effects ( $F(1, 28) = 6.5561, p < 0.05$ ).

The size of the pSTG-oIFG bundle was compared between subjects after normalization with respect to the total white matter volume. We define the normalized Connection Density A as:  $nCD_A = \log[\gamma N/V_{WM}]$ , which is the log transform of the number of fibers that run between two ipsilateral ROIs ( $N$ ), normalized by the White Matter volume ( $V_{WM}$ ).  $\gamma$  is a constant. The effect of handedness and hemisphere was assessed with a two-way ANOVA by computing the  $nCD_A$  of left and right pSTG-oIFG bundles in RH and LH. Men exhibit a statistically significant handedness effect ( $F(1, 28) = 5.3066, p < 0.05$ ) as well as interaction ( $F(1, 28) = 5.4562, p < 0.05$ ), shown in Figure 8.4. No such effect was visible in the group of women (Figure 8.4).

### 8.3.2 Inter-hemispheric connectivity

Inter-hemispheric connections between the left and right pSTG formed a relatively loose bundle and crossed the midsagittal plane at the level of the isthmus and anterior splenium; those between the left and right oIFG crossed at the level of the body of the corpus callosum (Fig. 8.3).

For interindividual comparison we used a log transform of the number of fibers ( $N$ ) that run between left and right pSTG or left and right oIFG normalized by callosal surface ( $nCD_B = \log[\gamma N/S_{CC}]$ ) to account for the putative relation between the mid-sagittal callosal area vs. handedness and gender [105].

Figure 8.6a) displays the inter-hemispheric oIFG connections that did not present any significant effect in terms of handedness or gender. Stronger variation was present for the pSTG inter-hemispheric connectivity; in particular, sex ( $F(1, 28) = 9.3247, p < 0.005$ ) and handedness ( $F(1, 28) = 5.8583, p < 0.05$ ) effects of a two-way ANOVA were statistically significant. A striking difference was the sparseness of interhemispheric pSTG connections in LH men (Fig. 8.6b).

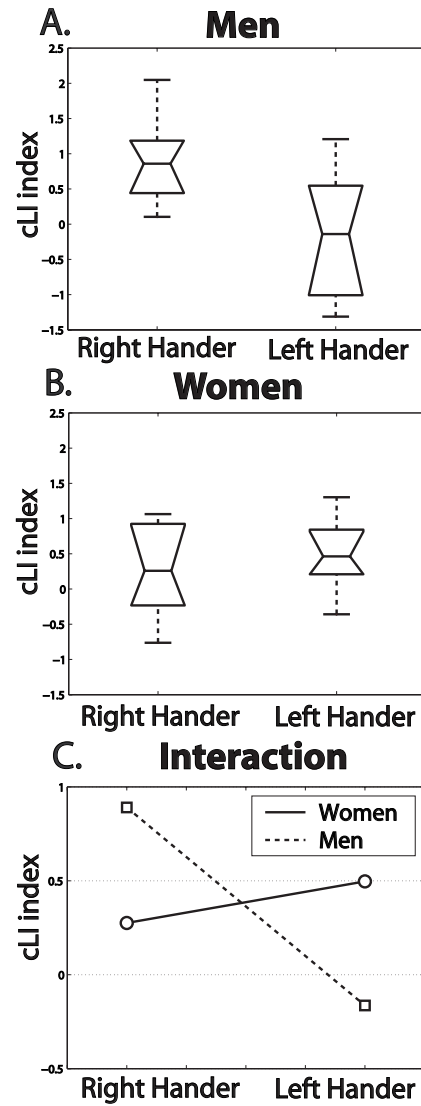


**Figure 8.4:** Lateralization of the pSTG-oIFG bundle, i.e. respective density of connections as measured by the cLI index; box plot and interaction plot. (A) RH men are significantly more lateralized towards the left hemisphere than the LH men. (B) RH women can not be differentiated from the LH women. (C) Significant interaction between sex and handedness.

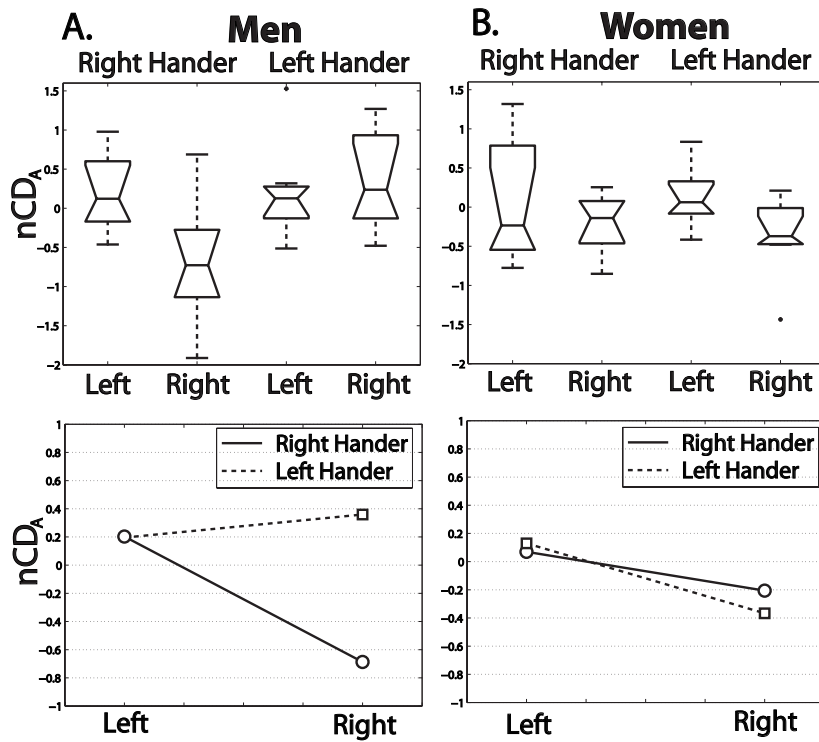


**Figure 8.5:** Connection density of the pSTG-oIFG bundle measured by the nCD<sub>A</sub> index, box plots and interaction plot. (A) Among men there is a significant handedness effect combined with an interaction between side and handedness that is due to a small right bundle in right handers. (B) Neither handedness nor side effects are significant in women.

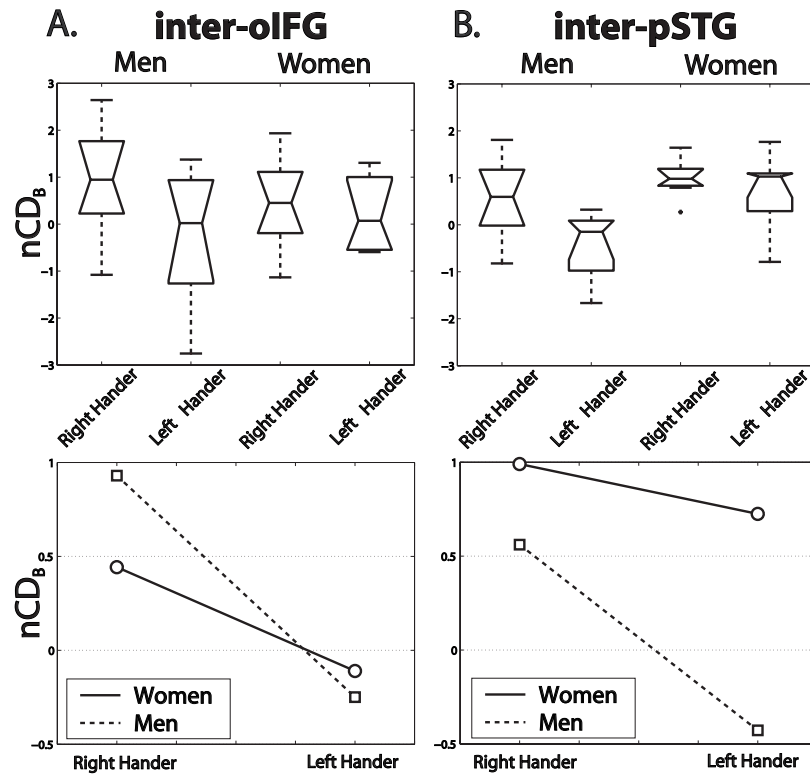


**Figure 8.6:** Inter-hemispheric connectivity ( $nCD_B$ ), box plots and interaction plots (see text). (A) Inter-oIFG connection density does not show any difference between men and women, RH and LH. (B) Inter-pSTG connection density exhibits a significant handedness and sex effect. The connections of the LH men are particularly sparse.

## 8.4 Discussion

Direct connections between Wernicke’s and Broca’s areas as well as between Broca’s or Wernicke’s area and their homologue have been postulated on the basis of tracing studies in non-human primates [122], but never directly demonstrated in man. We have found, in RH men, stronger connections between Wernicke’s and Broca’s areas than between their homologues in the right hemisphere. This is in agreement with previous studies, which demonstrated greater diffusion tensor anisotropy in the region of the left arcuate fasciculus in populations constituted predominantly by RH men [27, 30]. This strong interconnectivity between Wernicke’s and Broca’s areas speaks in favor of an integrated language network, as suggested by frequent co-activation of these areas in a variety of language tasks [63].

Women and LH men tended to have equally strong intrahemispheric connections between Wernicke’s and Broca’s areas as between their homologues, suggesting an extension of the integrated language network to the right hemisphere. Such an interpretation is supported by activation studies, which showed that language tasks yielded more right hemisphere activation in LH men [153] or groups of women and LH men [127] than in RH men. The tendency towards functional similarity of Broca’s and Wernicke’s areas and their homologues is also reflected in the lesser anatomical asymmetry reported in left handers [53, 111, 137].

Language networks that are confined to a single (left) hemisphere or distributed over the two hemispheres are likely to require different amounts of interhemispheric connectivity. The exclusively left hemisphere network needs to have access to information that is received and processed initially in the right hemisphere, such as sensory information concerning the left auditory and visual hemispace or the left hand. In agreement with this, Wernicke’s and Broca’s areas have been shown to receive homotopic (this paper) and heterotopic interhemispheric connections [41]. The bihemispheric network needs connections between speech areas on either side and, possibly, connections from non-speech areas in one hemisphere to the speech areas in the other hemisphere.

The amount of interhemispheric connectivity required by an exclusively left hemisphere network vs. bihemispheric network has been estimated differently by different authors. Based on tracing experiments in male rats, Galaburda and colleagues postulated that increased asymmetry of a region is accompanied by a smaller density of interhemispheric connections [59]. In humans, such a relationship was proposed for Wernicke’s area based on circumstantial evidence: the part of the corpus callosum in which the fibers from Wernicke’s area were believed to cross (isthmus; [2]) was smaller in subjects with greater asymmetry and, within this callosal part, there were fewer small diameter axons (the origin and termination of which was, however, not known; [166]). Further, but controversial, support came from studies of left-handers, who tend to have less asymmetrical speech areas; a few studies reported a larger posterior corpus callosum in left- than in right-handers, while more numerous studies denied it (for review see [13]). A recent, very thorough anatomical MRI study concluded that the relationship between cerebral asymmetries and callosal size and shape is far from clear [105].

Our results suggest that callosal connectivity of less asymmetrical speech areas is im-

plemented differently in men than in women. Speech comprehension area-related callosal connections tended to be less dense in left- than right-handed men. This goes against the rat model of hemispheric asymmetry and callosal connectivity [59] and does not fit the circumstantial evidence from human studies. The latter used global measures of callosal subparts [2] or axonal density of unknown origin [167], while we have visualized callosal connections belonging specifically to speech areas. Thus, the more bihemispherically distributed language network in LH men appears to require less callosal connectivity. It may rely on higher levels of language-related processing within the right hemisphere, so that callosal connections of the speech areas convey only information concerning the highest levels of speech processing and do not provide transfer of basic information.

In comparison to RH men, RH and LH women tend to be less lateralized for language [81, 133]. The density of their speech-related callosal connections is, however, similar to that of RH men, and furthermore, there is no measurable difference in this respect between RH and LH women. Their more bihemispherically distributed language network appears to be organized differently than in LH men, with notably more dense interhemispheric connections. These differences in callosal connectivity between less lateralized speech networks in women and in LH men may be the result of differential axonal elimination and maturation during development [79, 131].





---

# Does Human Brain Axonal Connectivity Form a Small World Network?

---

# 9

*...everything in the world must have design  
or the human mind rejects it. But in ad-  
dition it must have purpose or the human  
conscience shies away from it.*

J. Steinbeck

## 9.1 Introduction

Biological neuronal networks, and in particular the human brain, are remarkable natural systems capable of complicated patterns of behavior. The great diversity and adaptability, which characterizes evolved organisms, seems to be possible thanks to a meticulous combination of an enormous computational capacity, given by a huge amount of neuronal components, and a well designed communication network [95].

To understand the mechanisms behind higher level brain functions, the detailed study of their individual components clearly seems insufficient [91]. It is a necessity to consider global properties of such complex systems [145]. The backbone of complexity in the nervous system is composed by the large scale architectural characteristics of the neuronal network that constraints the communicative relationship between neuronal components. Recent works suggest that, driven by evolution, the structure of neuronal networks is governed by basic principles of constraint minimization, in the sense that brain geometry is organized such as to reduce wiring cost, minimize global energy consumption while keeping a maximal communication bandwidth [90]. Such simple design rules are shared with human made networks like electronic devices, electric power grids or even more dynamic systems like the

World Wide Web. As a consequence one naturally needs to ask how does the architecture of neuronal networks, and in the present study the human brain, looks like.

Classically, connection topology in a network is either considered completely regular, which is the case when the individual components are placed on a lattice and have connections with their local neighbors, or completely random in which case the connection between any two nodes is given by a probability independent of the geometrical distance. However many technological, social or biological networks don't fit any of the above mentioned network models but are represented by intermediate topologies that are characterized by high clustering as in regular lattices, yet exhibit small average path length, a feature shared with random graphs. With reference to the small world phenomenon described by the sociologist Stanley Milgram in the 1960s (in the context of an experiment on the structure of social networks [109]), Watts and Strogatz [158] called this type of networks small world graphs. They also showed that short average path length and high clustering coefficient was a property shared by very diverse networks as social networks, the United States power grid and the nervous system of *C. elegans*.

Because the nervous system of *C. elegans* is made of only 302 neurons, the exact mapping of its neuronal network can be unraveled with classical tools available to the biologist [162]. Its topology has been studied in detail and it has been shown that it is arranged in 11 clusters called ganglia in a manner that total wiring length is minimal [35]. In mammals, where  $1 \text{ mm}^3$  of cortex contains  $10^5$  neurons,  $10^8$  synapses and 4 km of axons [22], similar combined detailed and exhaustive approaches is clearly not feasible.

However we have seen in previous Chapters 5 and 6 that diffusion MRI tractography has the capacity to infer long-range WM axonal connectivity. Although being a kind of low pass "image" of the real, microscopic, neuronal network, it provides us, non-invasively, with exquisite information of the global topology of neuronal projections in the human brain. As readily guessed by Watts and Strogatz [158], we report on the small world architecture of the human brain long-range axonal network.

## 9.2 Methods

### 9.2.1 Constructing the Brain Connectivity Graph

We perform a brain study covering both hemispheres from the apex down to the inferior margin of the temporal lobes on a healthy volunteer. On an Intera 3T Philips scanner, we use a diffusion weighted single shot EPI sequence with the following timing parameters:  $TR/TE/\Delta/\delta = 3000/100/47.6/35 \text{ ms}$  and  $b\text{-max} = 12000 \text{ mm}^2/\text{s}$ . Q-space is sampled and the data reconstructed according to a standard DSIScheme (see Appendix). The acquisition block was made of 32 slices of a  $128 \times 128$  matrix with a spatial resolution of  $2 \times 2 \times 3 \text{ mm}^3$ .

In order to study brain long-range axonal network we perform on the reconstructed DSIData whole brain fiber tracking as previously described in Chapter 6. This procedure provides us with a set of lines that we consider as an estimate of the brain axonal WM trajectories (Figure 9.1).

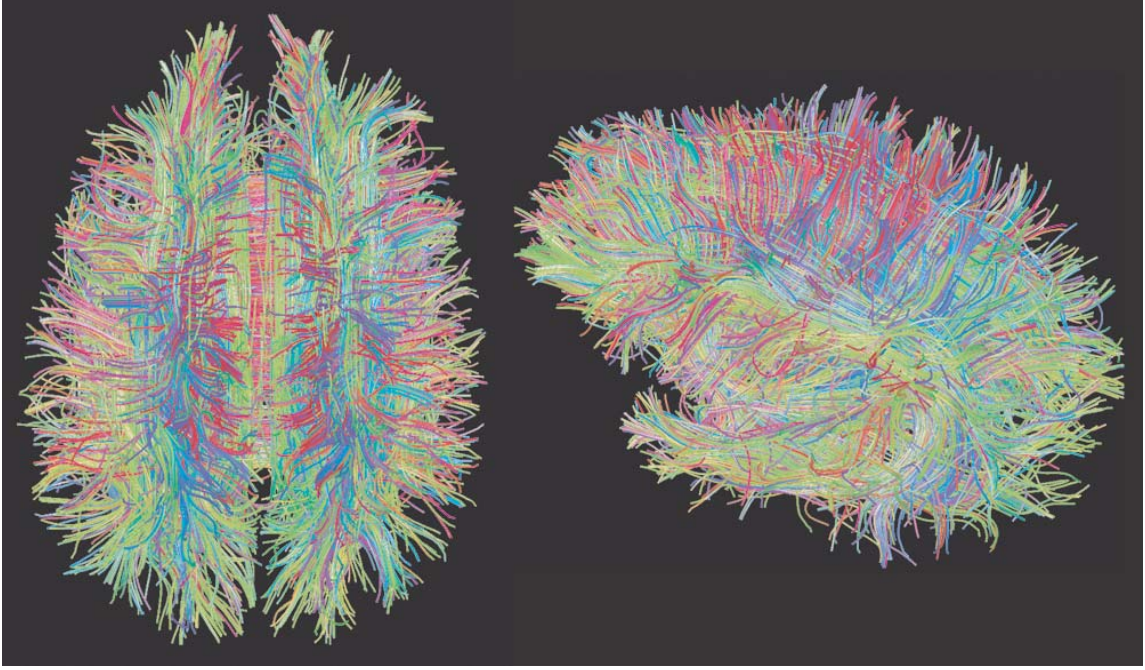


**Figure 9.1:** Estimate of whole brain axonal trajectories, superior and left oblique view. Green codes for antero-posterior, red for transverse and blue for cranio-caudal average fiber orientation.

As opposed to Chapter 6 where ROIs were placed manually in order to dissect out fiber tracts of interest, in the present experiment we choose the ROIs differently. We match a Talairach atlas [141] with the acquired brain image and use as ROIs the boxes defined by the integer Talairach coordinates, or its refined version where each Talairach box is subdivided into 8. This corresponds to ROIs respectively of size  $16 \times 19 \times 8 \text{ mm}^3$  and  $8 \times 9 \times 4 \text{ mm}^3$ . For atlas coordinates E the ROIs are slightly smaller as defined by Talairach. Furthermore we identify the brain GM by using a T1w based segmentation algorithm [169] and actually consider as ROIs only the Talairach boxes that contain GM. This construction is motivated by the fact that Talairach boxes have well described locations and that axons can only start and end in the GM.

We construct a graph  $\mathcal{G}_{\text{brain}}$  where the vertices represent the set of ROIs defined above. An edge between two vertices is drawn if there is at least one fiber that has its origin and termination in the pair of corresponding ROIs. This graph represents brain long-range axonal connectivity between small cortical areas and we study two versions of it,  $\mathcal{G}_{\text{brain}}(748)$  where each of the 748 vertices is a standard Talairach box (Figure 9.2A) and  $\mathcal{G}_{\text{brain}}(4522)$  being the fine grain version of it (Figure 9.2B).

Any graph can be represented by an adjacency matrix  $\mathbf{A} = (a_{ij})_{ij}$ , where any matrix entry  $a_{ij}$  is 0 if there exist no edge between vertex  $i$  and  $j$  and 1 if there is. As our model does not take into account orientation, the adjacency matrix is symmetric.

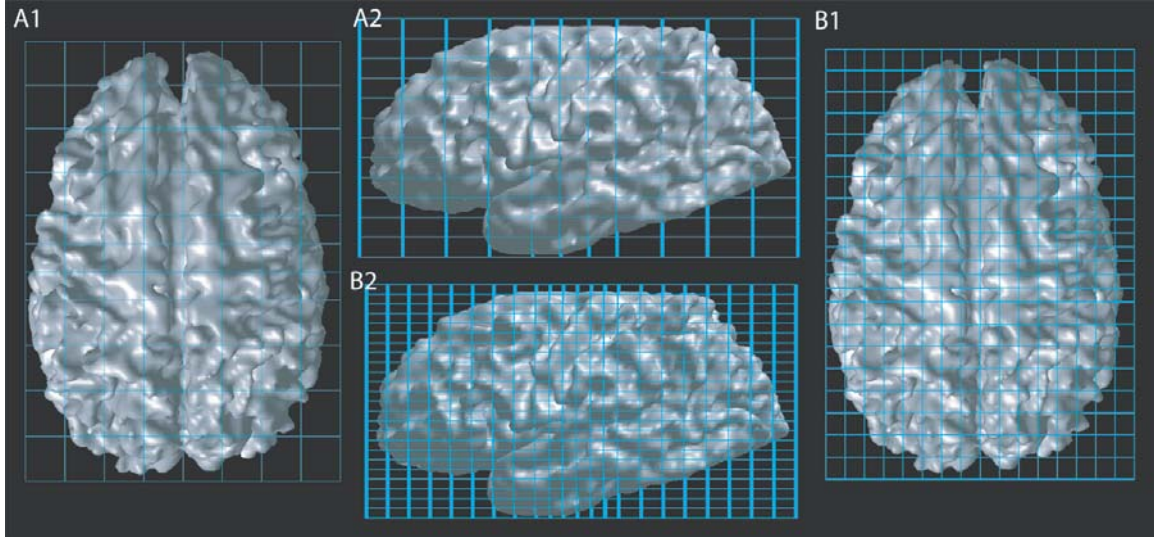


**Figure 9.2:** Definition of the ROIs. A Talairach atlas is matched with the brain image. A) The coarse ROIs defined by integer Talairach coordinates. B) The fine ROIs are defined by subdividing each coarse ROI (in figure A) into 8 sub-entities.

### 9.2.2 Construction of an Equivalent Random Graph

Given  $n$  and  $p$ , we define a random graph  $\mathcal{G}_{\text{rand}}(n, p)$  as a graph with labeled vertex set  $\{1, \dots, n\}$ , where each pair of vertices has an edge independently with probability  $p$  [19, 20]. We use this definition to construct a random graph of equal number of vertices as  $\mathcal{G}_{\text{brain}}$ , the above defined long-range axonal connectivity graph. The edge probability is empirically set as the ratio between the average vertex degree  $\bar{k}_{\text{brain}}$  of  $\mathcal{G}_{\text{brain}}$  and the number of vertices minus one in  $\mathcal{G}_{\text{brain}}$ :  $p = \frac{\bar{k}_{\text{actual}}}{n-1}$ .

### 9.2.3 Various Graph Measures

In order to characterize the topology of the graph under study, we concentrate on 3 measures that we describe here. The average path length  $L$  is defined as the number of edges in the shortest path between two vertices, averaged over the set of all pairs of vertices, according to [42], we have:

$$L = \frac{1}{n(n-1)/2} \sum_i \sum_{j:j>i} \min_l \{l : (\mathbf{A}^l)_{ij} \neq 0\}. \quad (9.1)$$

The clustering coefficient  $C$  is defined as follows. Suppose that a vertex  $i$  has  $k_i$  neighbors; then at most  $k_i(k_i - 1)/2$  edges can exist between them (this occurs when every neighbor of  $i$  is connected to every other neighbor of  $i$ ). Let  $C_i$  denote the fraction of these allowable edges that actually exist, then  $C$  is the average of  $C_i$  over all  $i$ , following [42] it can be computed as:

$$C = \frac{1}{9} \frac{\sum_i (\mathbf{A}^3)_{ii}}{\sum_{i \neq j} (\mathbf{A}^2)_{ij}} \quad (9.2)$$

Watts and Strogatz [158] have a nice and intuitive way to explain these two statistics. Consider a friendship network, then  $L$  is the average number of friendships in the shortest chain connecting two people;  $C_i$  reflects the extent to which friends of  $i$  are also friends of each other; and thus  $C$  measures the cliquishness of a typical friendship circle.

It remains to define the vertex degree distribution  $P(k)$ , which is the probability for one of its vertex to have  $k$  edges. The above defined  $\mathcal{G}_{\text{rand}}(n, p)$  has a binomial degree distribution  $\text{Bin}(n, p)$ . Given a graph, it can be estimated by plotting the histogram of the degree of each vertex:  $k_i = \sum_j a_{ij}$ .

### 9.3 Results

Figure 9.3 displays a schematic plot of the spectrally reordered adjacency matrix  $\mathbf{A}$  of graph  $\mathcal{G}_{\text{brain}}(4522)^*$ . First we notice that the matrix is sparse and that the reordering is efficient in the sense that most non zero entries are agglutinated around the diagonal. This suggests that there is local clustering of vertices. However there are still a number of non-zeros entries at some distance of the diagonals, which play the role of in-between cluster links. As a whole, this suggests that the graph has a small world topology.

More formally we test for small world topology (according to [158]) by computing the average path length  $L$  and the clustering coefficient  $C$  for the graph of brain connections and compare it with the mean of those statistics for several (here 3) instances of the equivalent random graph  $\mathcal{G}_{\text{rand}}(n, p)$ . We do it actually for  $n = 748$  and  $n = 4522$  as explained above.

Vertex number	$\bar{k}$	$L_{\text{brain}}$	$L_{\text{rand}}$	$C_{\text{brain}}$	$C_{\text{rand}}$
748	51.5	2.3383	1.9575	0.0308	0.0079
4522	25.3	3.3364	2.893	0.0114	0.00068

**Table 9.1:** Average path lengths and clustering coefficients in measure brain network and equivalent random graph. The average path length and clustering coefficient are computed in the measured brain network. These statistics are compared with instances of random graphs of identical average vertex number and degree.

We see in Table 9.1 that for both measured graph sizes,  $n = 748$  and  $n = 4522$ , the average path length of brain connectivity is of the same order than the random instances, whereas the clustering coefficient is higher for the brain. More importantly it seems that with increasing refinement of the measures the small world characteristics enhance, as the ratio  $L_{\text{brain}}/L_{\text{rand}}$  remains stable whereas the ratio  $C_{\text{brain}}/C_{\text{rand}}$  increases significantly. We also notice that the average degree  $\bar{k}$  decreases as  $n$  increases, which in our opinion should

---

\*Spectral reordering is a technique that reorders the entries of a matrix such that most non zeros elements are centered around the diagonal [72].



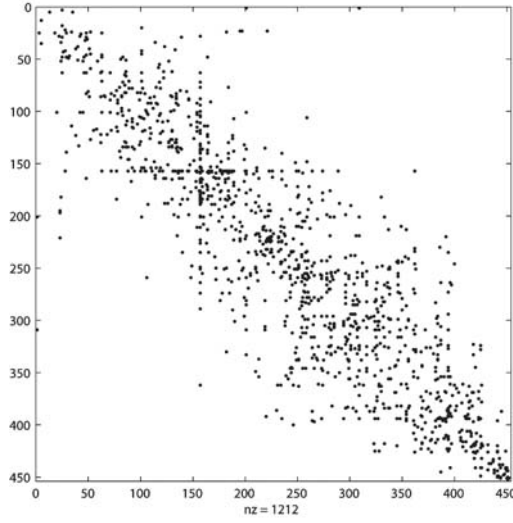


**Figure 9.3:** Reordered adjacency matrix plot. The adjacency matrix of  $\mathcal{G}_{\text{brain}}(4522)$  is reordered such that most non-zero entries are centered around the diagonal (see spectral reordering algorithm in [72]). The result is displayed by a plot of approximately  $1/10^{\text{th}}$  of the rows and columns. Most non-zero entries (dot) accumulate around the diagonal building clusters of intense connectivity, whereas a few inter-cluster edges are depicted by off diagonal elements. Together, these features are typical for small-world graphs.

not be interpreted as it might be an artifact as the number of total fibers is the same in both experiments. Hence, the average number of fibers starting or ending a ROIs decreases with its size.

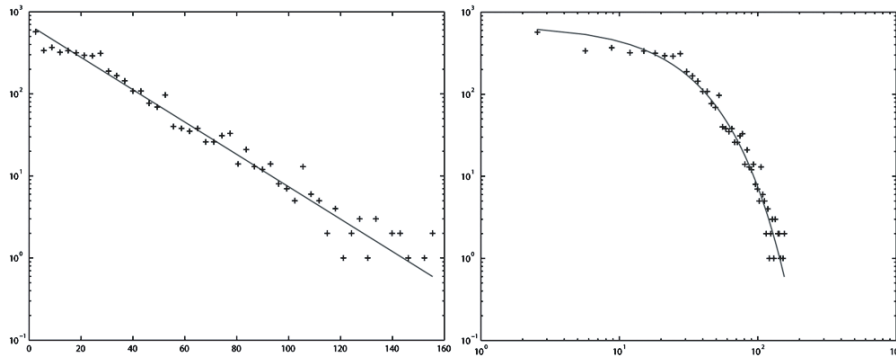


**Figure 9.4:** Empirical vertex degree distribution on  $\mathcal{G}_{\text{brain}}(4522)$ . LEFT) linear-log plot of the degree distribution (+) and exponential fit (line). RIGHT) log-log plot of the same degree distribution (+) and exponential fit (line). The vertex degree distribution is compatible with an exponentially decaying function, thus suggesting a single scale topology.

We also evaluate the empirical vertex degree distribution  $P(k)$  in a linear-log and a log-log plot. As depicted in Figure 9.4, the data seem to be compatible with a distribution of exponential decay, suggesting a single-scale behavior [3].

## 9.4 Discussion

Diffusion MRI tractography is classically used to identify the 3 dimensional trajectory of a specific axonal bundle. This can be used to study the inter- or intra-individual variations of single and readily known fiber tracts. This approach has certainly nice applications in neurosurgical planning, where the knowledge of the exact position of tumor-deviated tracts, like the cortico-spinal tract or the optical radiation, is of crucial importance. Potentialities are also given in diagnostic neurology or in basic neuro-anatomy where for example one could study language related brain asymmetries related to gender and handedness [70]. However such local approaches can only be applied to readily known structures which constitute only a tiny proportion of the huge set of significant fiber bundles. Furthermore it does not address key issues on global brain connection characteristics which seem to be essential in order to unravel higher order functional systems like emotion and consciousness [91][145].

The current approach distinguishes itself from the above mentioned techniques as it aims to study the *global* connective relationships between neuronal components and not the precise trajectories of specific links in 3D Euclidean space. Accordingly we combine conceptual modeling of neuronal networks with new measurement tools provided by the fast development of diffusion MRI. The first is based on not so old random graph theory [19, 45, 46] and provides us with powerful analytical tools and a multitude of analogy with communication sciences whereas the second is a unique technique that allows to capture brain connectivity at large scale non invasively in the human brain.

We need however to consider that there is a discrepancy between the real brain neuronal network, made of  $10^{10}$  vertices (neurons) and several order more edges (connections), and the graph constructed by our measurements, which is of much lower dimensionality and should be seen as a low pass filter applied on the real neuronal network. It nevertheless provides us with exquisite information on the "coarse grain" topology of the network and may asymptotically reflect its real microscopic organization.

By examining many alternative arrangements of macaque pre-frontal cortex, Klychako et al. [90] showed that the layout of cortical areas is such that it minimizes the total lengths of the axons needed to join them. The works of Zhang et al. [168] indicate that through evolution the volume of the WM scales as the  $4/3$  power of the volume of the GM, which can be explained by a need for the brain to maintain a fixed bandwidth of long-distance communication. With these concepts in mind, our observation that long-range axonal connectivity in the human brain is very sparse, strongly clustered and of small average path length makes sense. Hence small-world topology is a good compromise between full connectivity, which would be very costly in terms of wiring, i.e. brain volume, and power supply [5], and regular grid topology that impairs massively long distance bandwidth. Furthermore, the combination of high local clustering, short average path length with efficient neural coding [134] allows distributed computing where only a small fraction of local intense computation needs to be transmitted on distant regions, which may be sufficient for synchronous brain activity [66].

Based on post-mortem tracing studies in rat and macaque monkey brain regions, Hilge-

tag et al. [73, 75] reconstructed axonal connectivity graphs and found similar small world topologies for these brain parts, which again confirm our findings.

We need also to consider the developmental aspects of neuronal networks. In the neural tube, after intense mitotic activity the immature neurons migrate away from the proliferative zone into the cortical differentiation zone. During this process, they extend several thin cellular processes away from their cell body, which includes an axon and multiple dendrites. These elongations grow and navigate the central nervous system guided by chemical attractors and repellants to form multiples connections with other neurons [33]. In network terminology, the developing brain would be described as growing network where new vertices are added (cell division and migration) and new edges thrown (axonal and dendritic tree growth) according to a preferential attachment rule (governed by chemo attractants). Interestingly, small world topologies frequently arise from evolving networks. Various models have been proposed and two of them seem well suited the present framework. Kaiser et al. [87] proposed to model the development of frontal macaque cortex through a spatially embedded growing graph where preferential attachment occurs as an exponentially decaying function of spatial distance and growth limited in space, whereas Amaral et al. [3] damps vertex degree growth through vertex aging and energy limitations. These two models of network growth take into account some features of the developing mammal brain and as a result exhibit topologies, in terms of average path length (low), clustering (high) or even vertex degree distribution (exponential), similar to those encountered in mammal [73] or as presently shown human brains, which provides interesting conclusion on the relationship between molecular (chemo attractants and repellants), cellular (migration, aging and apoptosis), energy-related as well as anatomic and spatial constraints on one side and their influence on large scale topology of neuronal network.



---

# Axonal Network Topology Reveals the Hierarchical Organization of the Human Brain

---

# 10

*From 1.5 kilograms of flaccid matter, convoluted folds, about 100 billion neuronal components, hundreds of trillions of interconnections, many thousand kilometers of cabling, and a short cultural history emerged calculus, Swan Lake, Kind of Blue, the Macintosh, and The Master and Margarita.*

C. Koch and G. Laurent

## 10.1 Introduction

In 1909, Brodmann published his work on human brain cortex cytoarchitectonics [24]. By the detailed analysis of the microscopic components he proposed to subdivide the human cortex into 47 areas, which he believed carry out different functional tasks. Later, Brodmann's intuition was confirmed by a large amount of functional studies, which demonstrated regional specialization or local clustering of brain function [144]. For example, visual inputs are processed in the occipital lobe, auditory stimuli in the parieto-temporal junction, while motor tasks are concentrated in the frontal lobe. This local functional clustering is believed to rely on a substrate of locally intense cortical-cortical connections [121]. On the other hand more distant functional correlations between cortical and sub-cortical structures have been established and raised the concept of hierarchical processing stream where progressive sensory integration or motor decomposition occurs. For example, local connections

within the inferior temporal cortex form relays through progressively higher visual association areas [154, 161]. Local connections also form the basis of sensory processing streams in other parts of cortex, including the somato-sensory areas of the parietal lobe [56, 117] and the visual areas of the posterior parietal cortex [48]. Even further there is evidence, that higher cognitive functions require the rapid integration of information across several sensory and behavioral domains through reentrant interactions among widely distributed brain regions [146]. The experiments described above indicate that the cortical areas must be interconnected with an elaborate set of projections, made of several successive layers of connections where most substantial connections link neighboring regions but non negligible long distance wiring contributes to global brain synchronization.

In order to test the suggested hierarchical organization in the human brain, we rely on the recent developments of diffusion MRI. We have seen in previous chapters that DSI based tractography is a powerful method for investigating WM long-range axonal brain connectivity (Chapter 6), furthermore we have shown in Chapter 9 that combined with graph theoretic approaches, it is possible to extract useful information about neuronal network topology. In the present work we show how in terms of axonal projections cortical brain areas exhibit a hierarchical organization.

## 10.2 Methods

We perform a brain study covering both hemispheres from the apex down to the inferior margin of the temporal lobes on a healthy volunteer. On an Intera 3T Philips scanner, we use a diffusion weighted single shot EPI sequence with the following timing parameters:  $TR/TE/\Delta/\delta = 3000/100/47.6/35$  ms and  $b\text{-max} = 12000 \text{ mm}^2/\text{s}$ . Q-space is sampled and the data reconstructed according to the standard DSI scheme (see Chapter 4). The acquisition block was made of 32 slices of a  $128 \times 128$  matrix with a spatial resolution of  $2 \times 2 \times 3 \text{ mm}^3$ .

In order to study brain long-range axonal network we perform on the reconstructed DSI data whole brain fiber tracking as previously described in Chapter 6. This procedure provides us with a set of lines that we consider as an estimate of the brain axonal trajectories. Like in Chapter 9, we match a Talairach atlas [141] with the acquired brain image and use as ROIs the boxes defined by the integer Talairach coordinates. We identify the brain GM by using a T1w based segmentation algorithm [169] and consider as ROIs only the Talairach boxes that contain GM. We construct a graph where the vertices are the set of ROIs defined above and draw a link between two vertices if there is at least one fiber that has its origin and termination in the pair of ROIs. This graph represents brain long-range axonal connectivity.

We use hierarchical clustering [88], which is a way to investigate grouping in a data set, simultaneously over a variety of scales, by creating a cluster tree. The tree is not a single set of clusters, but rather a multilevel hierarchy, where clusters at one level are joined as clusters at the next higher level. This allows us to analyze clustering over various scales.

First a distance measure must be set between each pair of vertices. For the current application we simply define the distance  $d(i, j)$  as the shortest path length on the graph

between nodes  $i$  and  $j$ . We start by combining the two single vertices that have smallest distance into a pair. Iteratively we link the newly formed clusters to each other and to other vertices to create bigger clusters until all the objects in the original data set are linked together in a hierarchical tree. The between cluster distance is chosen to be the average measure:

$$d(\mathcal{R}, \mathcal{S}) = \frac{1}{|\mathcal{R}||\mathcal{S}|} \sum_{i \in \mathcal{R}} \sum_{j \in \mathcal{S}} d(i, j), \quad (10.1)$$

where  $\mathcal{R}$  and  $\mathcal{S}$  are two disjoint sets of vertices. The created hierarchical tree can then be pruned in order to partition the data into significant clusters.

### 10.3 Results

The hierarchy defined by the above described algorithm can be nicely summarized in a dendrogram (Figure 10.1). We also illustrate this decomposition by a schematic tree with at each hierarchical subdivision a little brain image that shows the current separation (Figure 10.2). If we read it from top to bottom, we first notice that there are two main clusters. They are separated by a large linkage distance and clearly correspond to the left and right hemispheres (Figure 10.2).

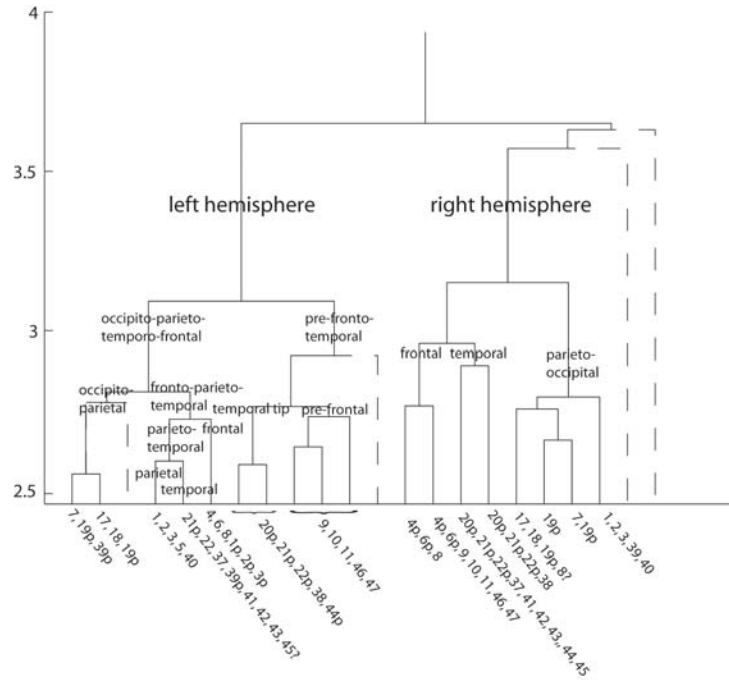


**Figure 10.1:** Dendrogram of cortico-cortical connections. Dendrogram constructed from the hierarchical clustering procedure. The "x-axis" shows the different brain areas referenced in Brodmann coordinates [24], whereas the "y-axis" plots the inter-cluster distance as defined in Eq. (10.1).

Considering the right hemisphere first, we notice next separation occurs between fronto-temporal and parieto-occipital cortices, which means that, in terms of WMaxonal connectivity, fronto-temporal as well as parieto-occipital intra-connectivity is intense as compared to the looser fronto-parietal, fronto-occipital or temporo-parieto-occipital links.

In the next hierarchical step frontal lobe separates from temporal lobe. Further down in the hierarchy, we see that temporal lobe is made of two clusters: the temporal tip on one side and of the resting caudal portion of the temporal lobe combined with tiny portion of the inferior frontal gyrus. On the other hand, frontal lobe is composed of a prefrontal and frontal cluster.

Parieto-occipital partition splits successively in two occipital and two parietal regions that are best described in terms of Brodmann areas. There is a cluster made of area 1,2,3,39 and 40, a cluster made of area 7 and partially 19, an other cluster localized in area 19 and an occipital cluster gathering areas 17, 18, partially 19 and maybe 8.

The hierarchy in the left hemisphere is clearly different and probably less intuitive at first sight. First, left hemisphere splits into a pre-fronto-temporal region, on one side, and into a region composed of the occipital and parietal cortices as well as the caudal part of the temporal cortex and frontal regions corresponding to functional motor and pre-motor cortices.

By further successive splitting, the hierarchy ends up into a pre-frontal and temporal subdivision on one hand and on a frontal "motoric" , two parietal, one occipital and one temporal (caudal part) cluster that combines as in the right hemisphere a tiny part of the inferior frontal gyrus.

Figure 10.3 illustrates intra- and inter-cluster fiber pathways. We can observe among the intra-cluster fibers of Figure 10.3A, a bundle relaying inferior frontal gyrus through the arcuate fasciculus. Figure 10.3B displays an example of inter-cluster projection between both occipital cortices.

## 10.4 Discussion

The identified groupings of cortical regions that largely agree with cytoarchitectonic [24] and, to a large extent, also with functional cortical subdivisions (Figure 10.2, [144]). At a certain "resolution" we segregate cortical lobes or lobes aggregates, whereas at an other level of finer "resolution" sub-lobar entities of functional significance appear. We can recognize a segregation into visual, auditory, motoric and somato-sensory as well as associative prefrontal and parietal areas.

Although we did not make a detailed analysis, the resulting asymmetric classification is not really surprising as it is well known that brains, in particular among right handed men, are asymmetric [70]. It is also worthwhile to observe that, in both hemispheres, the cortex in the parieto-temporal junction belongs to the same cluster as a part of the inferior frontal gyrus, as these regions are involved in the language networks [70].

The not perfect separation of both hemispheres at the first level of hierarchy can possibly be explained by the not perfect placement of the Talairach atlas, which might have

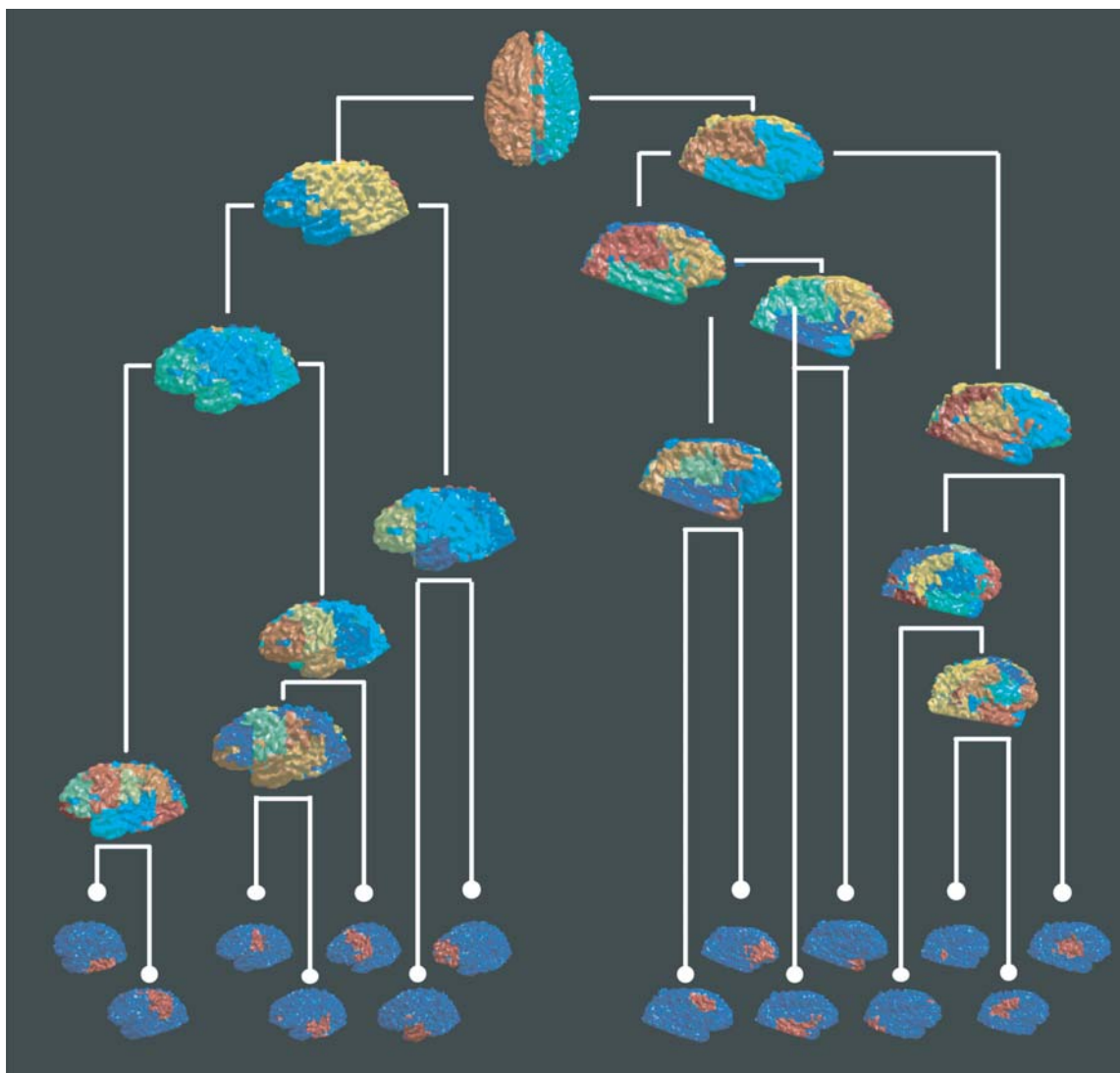


**Figure 10.2:** Schematic hierarchical tree of cortico-cortical connectivity. At each hierarchical subdivision a little brain image is displayed that shows the current cluster separation. The colors are random but chosen in order to maximize the contrast between the cortical region that currently split. At the end of the tree, each cortical area is displayed separately in red.

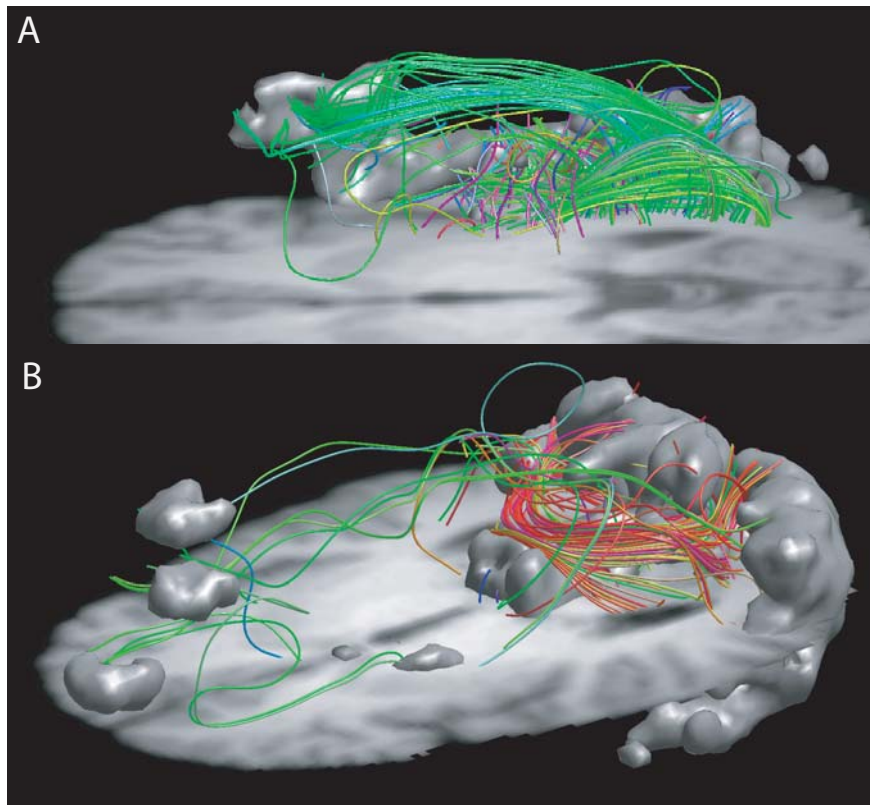


**Figure 10.3:** A) Intra-cluster connections in temporal region. B) Inter-cluster connections between left and right occipital lobes.

associated to the right hemisphere fibers that in fact lie in the left hemi-brain.

Generally speaking, these results confirm experiments made on local brain regions of macaque monkey and cat that showed a highly structured connectivity among brain areas. Carmichael et al. [32] demonstrated that in the frontal lobe most substantial connections are between neighboring areas, but that there are also areas of prominent connections between distant areas, while Fellman et al. [48] as well as Young [165] suggest distributed hierarchical organization of the primate cortex. Hilgetag et al. [73, 74, 75] confirmed the cluster-like and hierarchical organization of various sensory systems in macaque and cat cortices.

The presently shown structural clustering of neurons is probably related to their functional clustering [146] as long-range connections at the systems level may provide the structural scaffold for functional and effective connectivity [57]. Even more, there is evidence that higher cognitive functions and consciousness require rapid integration of information across several sensory and behavioral domains widely distributed brain regions [145] and are hierarchically organized [123, 139].





---

# Conclusion: Towards Brain Connectomics?

---

# 11

## 11.1 Achievements

Along the about hundred pages of this thesis, we have traveled through various topics, from basic diffusion MR physics to theoretical neuroscience. We have started, after a brief introduction on diffusion MRI, by addressing a fundamental and critical question of diffusion MRI. Indeed we showed, in Chapter 3 that under some weak assumptions diffusion contrast is positive, key issue for justifying emerging MRI techniques mapping non-Gaussian diffusion by measuring the only signal modulus. We then went through a thorough and comprehensive analysis of DSI, conducting several MR experiments, discussing its interpretation and its relation to other diffusion MRI techniques (Chapter 4). We then presented in Chapters 5 and 6 two tractography methods in order to infer brain connectivity from diffusion measurement. The first algorithm, designed for DTI, was an attempt to overcome the orientational uncertainty related to the DT approximation by a stochastic approach. These data were then used to introduce the concept of virtual dissection, method that allowed us to build a personalized atlas of fiber tracts in a single subject. The second tractography procedure was designed for high angular diffusion MRI data. It gave us the possibility to discuss the necessity for a diffusion MRI scheme to handle intra-voxel diffusion heterogeneity in order to map accurately important tracts. We also insisted on the importance of distinguishing the set of computer generated "fibers" or lines, which is a type of diffusion contrast and the cause of it, which is brain tissue. We have seen in Chapter 7 that the tract identification can be formalized as a segmentation task. Having bridged diffusion MRI with neuroscience thanks to tractography, we addressed various key neuro-anatomical questions. The power of group analysis allowed us in Chapter 8 to show the non trivial relationship between gender and handedness with the intra- and inter-hemispheric anatomical architecture of language networks. In Chapters 9 and 10 we left the classical hypothesis driven approach that consists of local and quantitative analysis of individual

connections to introduce a new paradigm for the study of brain connectivity. Convinced of the critical importance of large-scale connectivity architecture for the emergence of higher brain function, we proposed to study the global organization of the brain neuronal network. Combining the exquisite capacity of diffusion MRI tractography for mapping axonal trajectories with the well developed theory of graphs and large-scale networks, we constructed a new framework for studying the topology of human brain anatomical connectivity from in-vivo measurements. We reported on the small world structure of the long-range axonal network and suggested a hierarchical organization of the inter-cortical area connectivity.

## 11.2 Perspectives

### 11.2.1 Technical Improvements

From diffusion MRI to network topology, at each step, technical improvements are desirable.

- DSI should be faster, possibly by the use of heuristic reconstructions like q-ball [151] or PAS [82], in order to allow its use on patients. The optimal compromise between k-space and q-space, i.e. spatial and angular, resolution should be investigated.
- Tractography is still in its infancy. The currently available algorithms exploit very simple signal properties and still provide solutions with obvious artifacts.
- The network models presented are very coarse and should be refined. Inter-subject definition of cortical regions with a Talairach atlas is not optimal as it can be matched only poorly to the very variable cortical folding.

If the above enounced technofix stuff is certainly important for boosting our future discoveries, we must not forget to address a key conceptual issues, which is that brain neuronal communication must be investigated at various scales. Different scales require different tools. Diffusion MRI tractography provides global anatomic but macroscopic data, while detailed microscopic, but locally limited, morphology can be provided by histological tracing stains (e.g. [142]). Functional investigation is made possible with macroscopic fMRI, PET or EEG and with microscopic patch clamp techniques [67] for example. In this respect, the obvious future challenge will be to integrate this heterogeneous and enormous amount of data into a unified multi-level like description.

### 11.2.2 Defining the Brain Connectome

Over the last decade, we have seen flourish a large variety of new terms in the area of biomedical research, that are making reference to some large scale data. For example:

- Genome, which is all of the genetic information or hereditary material possessed by an organism [25].
- Proteome, the collection of functioning proteins synthesized by a living cell or tissue [25].

- Metabolome, the metabolic profile of a given cell, tissue, fluid, organ or organism.

These terms all have the suffix "-ome" attached to some biological entity for describing very large-scale data collection. "-ome" coming from the Latin "-oma" which means "body", is used in this context to denote a whole set of something [1].

In the last part of this thesis we have studied brain neuronal connections as a whole. Accordingly, it is clear that, like the genome, which is much more than just a juxtaposition of genes, the set of all neuronal connections in the brain is much more than the sum of their individual components. The genome is an entity it-self, as it is from the subtle gene interaction that life emerges. In a similar manner, one could consider the *brain connectome*, set of all neuronal connections, as one single entity, thus emphasizing the fact that the huge brain neuronal communication capacity and computational power critically relies on this subtle and incredibly complex connectivity architecture.

The graph representation and its associated adjacency matrix, induced from brain neuronal connections, seems a practical representation (Figure 11.1). Ideally, the true but clearly unreachable graph should be known and studied, where each neuron is represented by a labeled vertex and its connections with a set of weighted and oriented edges. Fortunately, its more realistic rough estimate, measured for example by diffusion MRI tractography, provides already an incredible amount of information that can be analyzed by readily available mathematical tools of graph and network theory, hence offering a large variety of fascinating research topics on brain neuronal communication and architecture for the coming years.

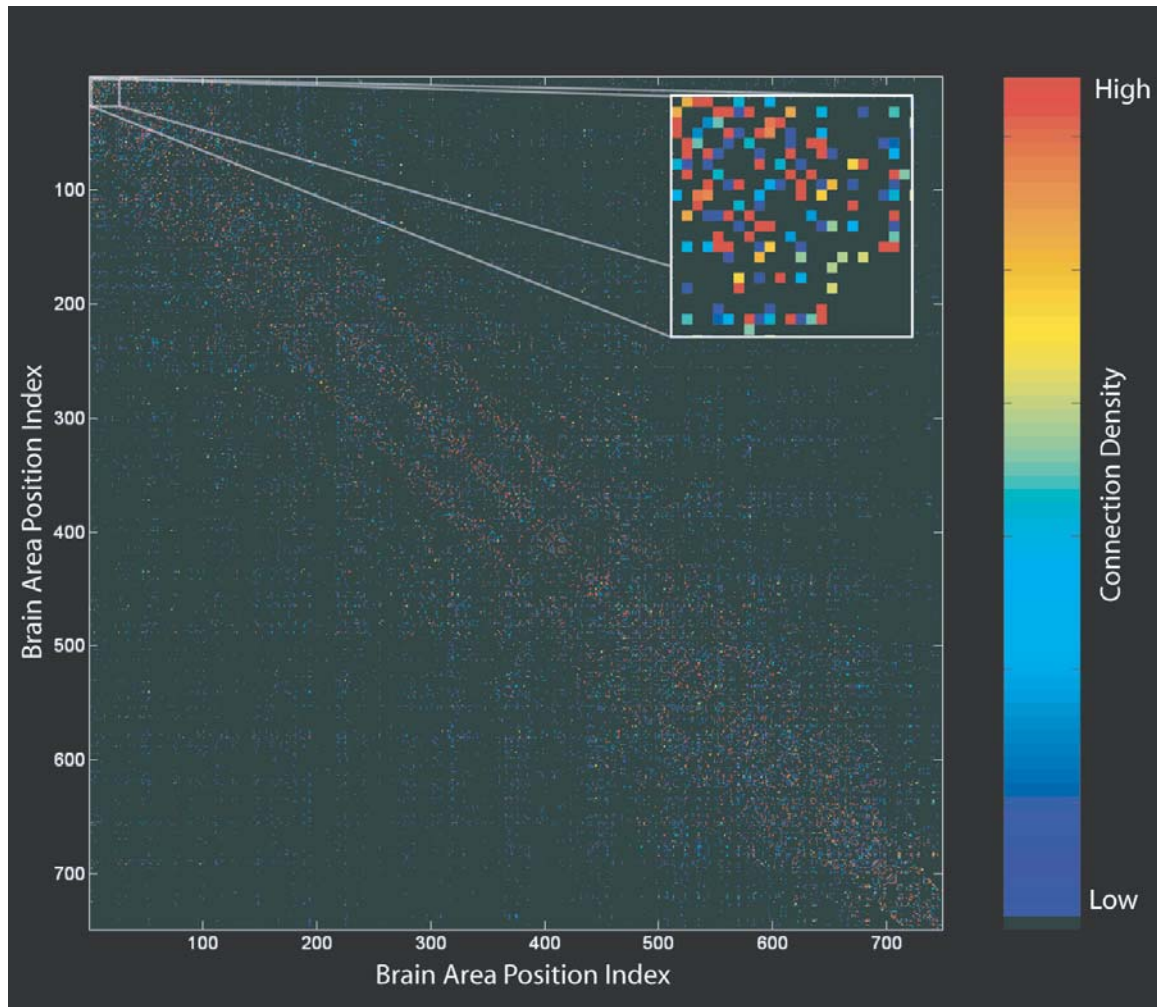


**Figure 11.1:** Brain connectome measured by diffusion MRI tractography. Each small cortex areas are labeled by a unique index equally spread along the matrix row and column. The connection density between two cortical locations  $i$  and  $j$  is color coded at matrix position  $ij$ .

---

# Bibliography

---

- [1] (2005). <http://www.answers.com/>.
- [2] F. Aboitiz, A. Scheibel, E. Zaidel (1992). Morphometry of the sylvian fissure and the corpus callosum, with emphasis on sex differences. *Brain* **115**(5):1521–41.
- [3] L. Amaral, A. Scala, M. Barthelemy, H. Stanley (2000). Classes of small-world networks. *Proc Natl Acad Sc USA* **97**(21):11149–11152.
- [4] K. Amunts et al. (1999). Broca’s region revisited: cytoarchitecture and intersubject variability. *J Comp Neurol* **412**(2):319–41.
- [5] D. Attwell, S. Laughlin (2001). An energy budget for signaling in the grey matter of the brain. *J Cereb Blood Flow Metab* **21**(10):1133–45.
- [6] L. Avram, Y. Assaf, Y. Cohen (2004). The effect of rotational angle and experimental parameters on the diffraction patterns and micro-structural information obtained from q-space diffusion nmr: implication for diffusion in white matter fibers. *J Magn Reson* **169**(1):30–8.
- [7] P. Basser, D. Jones (2002). Diffusion-tensor mri: theory, experimental design and data analysis - a technical review. *NMR Biomed* **15**(7-8):456–67.
- [8] P. Basser, J. Mattiello, D. LeBihan (1994). Estimation of the effective self-diffusion tensor from the nmr spin echo. *J Magn Reson B* **103**(3):247–54.
- [9] P. Basser, J. Mattiello, D. LeBihan (1994). Mr diffusion tensor spectroscopy and imaging. *Biophys J* **66**(1):259–67.
- [10] P. Basser, C. Pierpaoli (1996). Microstructural and physiological features of tissues elucidated by quantitative-diffusion-tensor mri. *J Magn Reson B* **111**(3):209–19.
- [11] P. Basser, C. Pierpaoli (1998). A simplified method to measure the diffusion tensor from seven mr images. *Magn Reson Med* **39**:928–934.
- [12] P. Basser et al. (2000). In vivo fiber tractography using dt-mri data. *Magn Reson Med* **44**(4):625–32.

- 
- [13] A. Beaton (1997). The relation of planum temporale asymmetry and morphology of the corpus callosum to handedness, gender, and dyslexia: a review of the evidence. *Brain Lang* **60**(2):255–322.
  - [14] C. Beaulieu (2002). The basis of anisotropic water diffusion in the nervous system - a technical review. *NMR Biomed* **15**(7-8):435–55.
  - [15] C. Beaulieu (2002). Relating micro-structural properties of neural fibres with anisotropic diffusion. In *Proc. Workshop on Diffusion MRI: Biophysical Issues*, pp. 79–82, ISMRM.
  - [16] C. Beaulieu, P. S. Allen (1994). Determinants of anisotropic water diffusion in nerves. *Magn Reson Med* **31**(4):394–400.
  - [17] J. Besag (1986). On the statistical-analysis of dirty pictures. *J Roy Stat Soc B* **48**(3):259–302.
  - [18] R. Blinc, J. Pirs, I. Zupancic (1973). Measurement of self-diffusion in liquid-crystals by a multiple-pulse nmr method. *Phys Rev Lett* **30**(12):546–549.
  - [19] B. Bollobâas (1985). *Random Graphs*. Academic Press, London a.o.
  - [20] B. Bollobâas (1998). *Modern Graph Theory*. Springer, New York.
  - [21] M. Bozzali et al. (2002). White matter damage in alzheimer’s disease assessed in vivo using diffusion tensor magnetic resonance imaging. *J Neurol Neurosurg Psychiatry* **72**(6):742–6.
  - [22] V. Braitenberg, A. Schütz (1998). *Cortex: Statistics and Geometry of Neuronal Connectivity*. Springer, Berlin, 2 edn.
  - [23] P. Brémaud (1999). *Markov Chains, Gibbs Fields, Monte Carlo Simulation and Queues*. Springer-Verlag.
  - [24] K. Brodmann (1985). *Vergleichende Lokalisationslehre der Grosshirnrinde in ihren Prinzipien dargestellt auf Grund des Zellenbaues*. Leipzig, reprint der originalausgabe von 1909, (1. aufl.) / mit einem nachwort und einem literaturverzeichnis von ernst winkelman, leipzig, und karl seidel, berlin edn. Von K. Brodmann 22 cm Ill. Originalimpressum: Leipzig : Verlag von Johann Ambrosius Barth , 1909.
  - [25] T. Brown (2002). *Genomes*. BIOS Scientific Publishers Ltd, Oxford, UK, 2nd edn.
  - [26] A. Brun et al. (2004). Clustering fiber tracts using normalized cuts. In *Seventh International Conference on Medical Image Computing and Computer-Assisted Intervention (MICCAI’04)*, Lecture Notes in Computer Science, pp. 368–375, Rennes - Saint Malo, France.

- 
- [27] C. Buchel et al. (2004). White matter asymmetry in the human brain: A diffusion tensor mri study. *Cereb Cortex* **14**(9):945–51.
- [28] R. Buxton (2002). *Introduction to functional magnetic resonance imaging principles and techniques*. Cambridge University Press, Cambridge.
- [29] P. Callaghan (1991). *Principles of Nuclear Magnetic Resonance Microscopy*. Oxford Science Publications.
- [30] Y. Cao et al. (2003). Asymmetry of subinsular anisotropy by in vivo diffusion tensor imaging. *Hum Brain Mapp* **20**(2):82–90.
- [31] A. Caprihan, L. Wang, E. Fukushima (1996). A multiple-narrow-pulse approximation for restricted diffusion in a time-varying field gradient. *J Magn Reson Ser A* **118**(1):Jan.
- [32] S. Carmichael, J. Price (1996). Connectional networks within the orbital and medial prefrontal cortex of macaque monkeys. *J Comp Neurol* **371**(2):179–207.
- [33] D. Charney (ed.) (2004). *Neurobiology of mental illness*. Oxford University Press, New York, 2nd edn.
- [34] T. Chenevert, J. Brunberg, J. Pipe (1990). Anisotropic diffusion in human white matter: demonstration with mr techniques in vivo. *Radiology* **177**(2):401–5.
- [35] C. Cherniak (1994). Component placement optimization in the brain. *J Neurosci* **14**(4):2418–27.
- [36] S. Clarke et al. (1995). The auditory pathway in cat corpus callosum. *Exp Brain Res* **104**(3):534–40.
- [37] S. Clarke et al. (1999). Thalamic projections of the fusiform gyrus in man. *Eur J Neurosci* **11**(5):1835–8.
- [38] Y. Cohen, Y. Assaf (2002). High b-value q-space analyzed diffusion-weighted mrs and mri in neuronal tissues - a technical review. *NMR Biomed* **15**(-1):516–42.
- [39] T. Conturo et al. (1999). Tracking neuronal fiber pathways in the living human brain. *Proc Natl Acad Sci U S A* **96**(18):10422–7.
- [40] J. Coremans, R. Luyt, T. Verhelle, F. and Stadnik, M. Osteaux (1994). A method for myelin fiber orientation mapping using diffusion-weighted mr images. *Magn Reson Imaging* **12**(3):443–54.
- [41] G. Di Virgilio, S. Clarke, G. Pizzolato, T. Schaffner (1999). Cortical regions contributing to the anterior commissure in man. *Exp Brain Res* **124**(1):1–7.
- [42] S. Dorogovtsev, J. Mendes (2003). *Evolution of networks from biological nets to the internet and WWW*. Oxford University Press, Oxford.



- 
- [43] N. Dronkers et al. (2004). Lesion analysis of the brain areas involved in language comprehension. *Cognition* **92**(1-2):145–177.
- [44] A. Einstein (1956). *Investigations on the theory of the Brownian movement*. Dover Publications. Collection of papers translated from the German.
- [45] P. Erdos, A. Renyi (1959). On random graphs. *Publ Math Debrecen* **6**:290.
- [46] P. Erdos, A. Renyi (1960). On the evolution of random graphs. *Bull Int Stat Inst* **38**(4):343–347.
- [47] G. Falzi, P. Perrone, L. Vignolo (1982). Right-left asymmetry in anterior speech region. *Arch Neurol* **39**(4):239–40.
- [48] D. Fellman, D. Van Essen (1991). Distributed hierarchical processing in the primate cerebral cortex. *Cereb Cortex* **1**(1):1–47.
- [49] A. Field et al. (2002). Diffusion-tensor mr imaging patterns in white matter tracts altered by neoplasm. In *Workshop on Diffusion MRI: Biophysical Issues*, pp. 137–40, ISMRM.
- [50] M. Filippi et al. (2001). Diffusion tensor magnetic resonance imaging in multiple sclerosis. *Neurology* **56**(3):304–11.
- [51] R. M. Filippi M (2004). Magnetization transfer magnetic resonance imaging in the assessment of neurological diseases. *J Neuroimaging* **14**(4):303–13.
- [52] J. Foong et al. (2000). Neuropathological abnormalities of the corpus callosum in schizophrenia: a diffusion tensor imaging study. *J Neurol Neurosurg Psychiatry* **68**(2):242–4.
- [53] A. Foundas, Leonard, B. CM, Hanna-Pladdy (2002). Variability in the anatomy of the planum temporale and posterior ascending ramus: do right- and left handers differ? *Brain Lang* **83**(3):403–24.
- [54] A. Foundas et al. (1996). Pars triangularis asymmetry and language dominance. *Proc Natl Acad Sci U S A* **93**(2):719–22.
- [55] L. Frank (2001). Anisotropy in high angular resolution diffusion-weighted mri. *Magn Reson Med* **45**(6):935–9.
- [56] D. Friedman, E. Murray (1986). Thalamic connectivity of the second somatosensory area and neighboring somatosensory fields of the lateral sulcus of the macaque. *J Comp Neurol* **252**(3):348–73.
- [57] K. Friston (1994). Functional and effective connectivity: A synthesis. *Hum Brain Mapp* **2**:56–78.



- 
- [58] A. Galaburda, M. LeMay, T. Kemper, N. Geschwind (1978). Right-left asymmetries in the brain. *Science* **199**(4331):852–6.
- [59] A. Galaburda, G. Rosen, G. Sherman (1990). Individual variability in cortical organization: its relationship to brain laterality and implications to function. *Neuropsychologia* **28**(6):529–46.
- [60] R. Galuske, W. Schlote, H. Bratzke, W. Singer (2000). Interhemispheric asymmetries of the modular structure in human temporal cortex. *Science* **289**(5486):1946–9.
- [61] D. Geman (1990). Random-fields and inverse problems in imaging. *Lect Notes Math* **1427**:113–193.
- [62] S. Geman, D. Geman (1984). Stochastic relaxation, gibbs distributions, and the bayesian restoration of images. *IEEE T Pattern Anal* **6**(6):721–41.
- [63] M. Gernsbacher, M. Kaschak (2003). Neuroimaging studies of language production and comprehension. *Annu Rev Psychol* **54**:91–114.
- [64] C. Good et al. (2001). Cerebral asymmetry and the effects of sex and handedness on brain structure: a voxel-based morphometric analysis of 465 normal adult human brains. *Neuroimage* **14**(3):685–700.
- [65] C. Gossel et al. (2002). Fiber tracking from dti using linear state space models: detectability of the pyramidal tract. *Neuroimage* **16**(2):378–88.
- [66] C. Gray, P. Konig, A. Engel, W. Singer (1989). Oscillatory responses in cat visual cortex exhibit inter-columnar synchronization which reflects global stimulus properties. *Nature* **338**(6213):334–7.
- [67] A. Gupta, Y. Wang, H. Markram (2000). Organizing principles for a diversity of gabaergic interneurons and synapses in the neocortex. *Science* **287**(5451):273–8.
- [68] R. Gur et al. (1980). Differences in the distribution of gray and white matter in human cerebral hemispheres. *Science* **207**(4436):1226–8.
- [69] P. Hagmann et al. (2003). Dti mapping of human brain connectivity: statistical fibre tracking and virtual dissection. *Neuroimage* **19**(3):545–54.
- [70] P. Hagmann et al. (2004). Dti tractography of the wernicke and broca connectivity in right and left hander. vol. 11 of *Proc. Intl. Soc. Mag. Reson. Med*, p. 625.
- [71] J. Hammersley, P. Clifford (1968). Markov fields on finite graphs and lattices. *unpublished manuscript*.
- [72] D. Higham (2003). Unravelling small world networks. *J Comp Appl Math* **158**(1):61–74.

- 
- [73] C. Hilgetag, M. Kaiser (2004). Clustered organization of cortical connectivity. *Neuroinformatics* **2**(3):353–360.
- [74] C. Hilgetag, M. O’Neill, M. Young (2000). Hierarchical organization of macaque and cat cortical sensory systems explored with a novel network processor. *Philos T Roy Soc B* **355**(1393):71–89.
- [75] C. Hilgetag et al. (2000). Anatomical connectivity defines the organization of clusters of cortical areas in the macaque monkey and the cat. *Philos T Roy Soc B* **355**(1393):91–110.
- [76] A. J. Hoon et al. (2002). Diffusion tensor imaging of periventricular leukomalacia shows affected sensory cortex white matter pathways. *Neurology* **59**(5):752–6.
- [77] R. Horn, C. Johnson (1985). *Matrix Analysis*. Cambridge University Pres.
- [78] M. Horsfield, D. Jones (2002). Applications of diffusion-weighted and diffusion tensor mri to white matter diseases - a review. *NMR Biomed* **15**(7-8):570–7.
- [79] G. Innocenti (1994). Some new trends in the study of the corpus callosum. *Behav Brain Res* **64**(1-2):1–8.
- [80] B. Jacobs, M. Schall, A. Scheibel (1993). A quantitative dendritic analysis of wernicke’s area in humans. ii. gender, hemispheric, and environmental factors. *J Comp Neurol* **327**(1):97–111.
- [81] J. Jaeger et al. (1998). Sex differences in brain regions activated by grammatical and reading tasks. *Neuroreport* **9**(12):2803–7.
- [82] K. Jansons, D. Alexander (2004). Persistent angular structure: new insights from diffusion magnetic resonance imaging data. *inverse problems* **19**(5):1031–1046.
- [83] L. Jonasson, P. Hagmann, J. Thiran, W. VJ (2005). Fiber tracts of high angular resolution diffusion mri are easily segmented with spectral clustering. vol. 12 of *Proc. Intl. Soc. Mag. Reson. Med*, p. 1312.
- [84] L. Jonasson et al. (2004). In press: White matter fiber tract segmentation in dt-mri using geometric flows. *Medical Image Analysis* p. null.
- [85] D. Jones (2003). Determining and visualizing uncertainty in estimates of fiber orientation from diffusion tensor mri. *Magn Reson Med* **49**(1):7–12.
- [86] D. Jones, A. Simmons, S. Williams, M. Horsfield (1999). Non-invasive assessment of axonal fiber connectivity in the human brain via diffusion tensor mri. *Magn Reson Med* **42**(1):37–41.
- [87] M. Kaiser, C. Hilgetag (2004). Modelling the development of cortical systems networks. *Neurocomputing* **58-60**:297–302.

- 
- [88] L. Kaufman, P. Rousseeuw (1990). *Finding groups in data an introduction to cluster analysis*. Wiley, New York.
- [89] T. Klingberg et al. (2000). Microstructure of temporo-parietal white matter as a basis for reading ability: evidence from diffusion tensor magnetic resonance imaging. *Neuron* **25**(2):493–500.
- [90] V. Klyachko, C. Stevens (2003). Connectivity optimization and the positioning of cortical areas. *Proc Natl Acad Sci U S A* **100**(13):7937–41.
- [91] C. Koch, G. Laurent (1999). Complexity and the nervous system. *Science* **284**(5411):96–98.
- [92] M. Koch, D. Norris, M. Hund-Georgiadis (2002). An investigation of functional and anatomical connectivity using magnetic resonance imaging. *Neuroimage* **16**(1):241–50.
- [93] M. Koch et al. (2001). Estimation of anatomical connectivity from diffusion tensor data. In *Proc. of 7th Annual Meeting of the Organization for Human Brain Mapping, Brighton*, p. 10974, HBM.
- [94] E. Kreyszig (1989). *Introductory functional analysis with applications*. Wiley.
- [95] S. Laughlin, T. Sejnowski (2003). Communication in neuronal networks. *Science* **301**(5641):1870–4.
- [96] M. Lazar, D. Weinstein, K. Hasan, A. Alexander (2000). Axon tractography with tensorlines. In *Proceeding of International Society of Magnetic Resonance in Medicine, Denver, CO*, p. 482.
- [97] D. Le Bihan (1991). Molecular diffusion nuclear magnetic resonance imaging. *Magn Reson Q* **7**(1):1–30.
- [98] D. Le Bihan (1995). *Diffusion and Perfusion Magnetic Resonance Imaging: Applications to Functional MRI*. Lippincott Williams & Wilkins.
- [99] D. Le Bihan (1995). Molecular diffusion, tissue microdynamics and microstructure. *NMR Biomed* **8**(7-8):375–86.
- [100] D. Le Bihan (2003). Looking into the functional architecture of the brain with diffusion mri. *Nat Rev Neurosci* **4**(6):469–80.
- [101] D. Le Bihan et al. (1986). Mr imaging of intravoxel incoherent motions: application to diffusion and perfusion in neurologic disorders. *Radiology* **161**(2):401–7.
- [102] D. Le Bihan et al. (2001). Diffusion tensor imaging: concepts and applications. *J Magn Reson Imaging* **13**(4):534–46.

- 
- [103] K. Lim et al. (1999). Compromised white matter tract integrity in schizophrenia inferred from diffusion tensor imaging. *Arch Gen Psychiatry* **56**(4):367–74.
  - [104] C. Liu, R. Bammer, B. Acar, M. Moseley (2004). Characterizing non-gaussian diffusion by using generalized diffusion tensors. *Magn Reson Med* **51**(5):924–37.
  - [105] E. Luders et al. (2003). Relationships between sulcal asymmetries and corpus callosum size: gender and handedness effects. *Cereb Cortex* **13**(10):1084–93.
  - [106] J. Maldjian, R. Grossman (2001). Future applications of dwi in ms. *J Neurol Sci* **186**(Suppl 1):S55–7.
  - [107] H. Mamata et al. (2002). Combined mapping of functional domains and axonal connectivity in cat visual cortex using fmri and dti. In *Workshop on Diffusion MRI: Biophysical Issues*, pp. 121–4, ISMRM.
  - [108] R. Martin (2003). Language processing: functional organization and neuroanatomical basis. *Annu Rev Psychol* **54**:55–89.
  - [109] S. Milgram (1967). The small world problem. *Psychol. Today* **2**:60–67.
  - [110] P. Mitra, B. Halperin (1995). Effects of finite gradient-pulse widths in pulsed-field-gradient diffusion measurements. *J Magn Reson Ser A* **113**(1):94–101.
  - [111] L. D. Moffat SD, Hampson E (1998). Morphology of the planum temporale and corpus callosum in left handers with evidence of left and right hemisphere speech representation. *Brain* **121**(12):2369–79.
  - [112] S. Mori, B. Crain, V. Chacko, P. van Zijl (1999). Three-dimensional tracking of axonal projections in the brain by magnetic resonance imaging. *Ann Neurol* **45**(2):265–9.
  - [113] S. Mori, P. van Zijl (2002). Fiber tracking: principles and strategies - a technical review. *NMR Biomed* **15**(7-8):468–80.
  - [114] S. Mori et al. (2002). Brain white matter anatomy of tumor patients evaluated with diffusion tensor imaging. *Ann Neurol* **51**(3):377–80.
  - [115] S. Mori et al. (2002). Imaging cortical association tracts in the human brain using diffusion-tensor-based axonal tracking. *Magn Reson Med* **47**(2):215–23.
  - [116] J. Munkres (1975). *Topology a first course*. Prentice Hall, Englewood Cliffs, New Jersey.
  - [117] J. Neal, R. Pearson, T. Powell (1987). The cortico-cortical connections of area 7b, pf, in the parietal lobe of the monkey. *Brain Res* **419**(1-2):341–6.
  - [118] R. Nieuwenhuys, J. Voogd, C. van Huijzen (1988). *The Human Central Nervous System*. Springer-Verlag, 3rd edn.

- 
- [119] R. Oldfield (1971). The assessment and analysis of handedness: the edinburgh inventory. *Neuropsychologia* **9**(1):97–113.
- [120] S. Pajevic, C. Pierpaoli (1999). Color schemes to represent the orientation of anisotropic tissues from diffusion tensor data: application to white matter fiber tract mapping in the human brain. *Magn Reson Med* **42**(3):526–40.
- [121] S. Petersen (1988). Positron emission tomographic studies of the cortical anatomy of single-word processing. *Nature* **331**(6157):585–9.
- [122] M. Petrides, D. Pandya (1988). Association fiber pathways to the frontal cortex from the superior temporal region in the rhesus monkey. *J Comp Neurol* **273**(1):52–66.
- [123] F. Petroni et al. (2001). Simultaneity of responses in a hierarchical visual network. *Neuroreport* **12**(12):2753–9.
- [124] C. Pierpaoli et al. (1996). Diffusion tensor mr imaging of the human brain. *Radiology* **201**(3):637–48.
- [125] C. Poupon et al. (2001). Towards inference of human brain connectivity from mr diffusion tensor data. *Med Image Anal* **5**(1):1–15.
- [126] J. Powles, M. Mallett, G. Rickayzen, W. Evans (1992). Exact analytic solutions for diffusion impeded by an infinite array of partially permeable barriers. *Proc. R. Soc. Lond. A* **436**:391–403.
- [127] J. Pujol, J. Deus, J. Losilla, A. Capdevila (1999). Cerebral lateralization of language in normal left-handed people studied by functional mri. *Neurology* **52**(5):1038–43.
- [128] T. Reese, O. Heid, R. Weisskoff, V. Wedeen (2003). Reduction of eddy-current-induced distortion in diffusion mri using a twice-refocused spin echo. *Magn Reson Med* **49**(1):177–182.
- [129] S. Resnick (1998). *A Probability Path*. Birkhauser, Boston.
- [130] S. Rose et al. (2000). Loss of connectivity in alzheimer’s disease: an evaluation of white matter tract integrity with colour coded mr diffusion tensor imaging. *J Neurol Neurosurg Psychiatry* **69**(4):528–30.
- [131] V. Schmithorst, M. Wilke, B. Dardzinski, S. Holland (2002). Correlation of white matter diffusivity and anisotropy with age during childhood and adolescence: a cross-sectional diffusion-tensor mr imaging study. *Radiology* **222**(1):212–8.
- [132] H. Seldon (1985). *The Anatomy of Speech Perception: Human Auditory Cortex*, vol. 4 of *Cerebral Cortex*, chap. 7, p. 273. Plenum Press.
- [133] B. Shaywitz et al. (1995). Sex differences in the functional organization of the brain for language. *Nature* **373**(6515):607–9.

- 
- [134] E. Simoncelli, B. Olshausen (2001). Natural image statistics and neural representation. *Annu Rev Neurosci* **24**:1193–216.
- [135] A. Sorensen et al. (1996). Hyperacute stroke: evaluation with combined multisec-tion diffusion-weighted and hemodynamically weighted echo-planar mr imaging. *1996* **199**(2):391–401.
- [136] C. Sotak (2002). The role of diffusion tensor imaging in the evaluation of ischemic brain injury - a review. *NMR Biomed* **15**(7-8):561–9.
- [137] H. Steinmetz, J. Volkmann, L. Jancke, H. Freund (1991). Anatomical left-right asym-metry of language-related temporal cortex is different in left- and right-handers. *Ann Neurol* **29**(3):315–9.
- [138] E. Stejskal, J. Tanner (1965). Spin diffusion measurements - spin echoes in presence of a time-dependent field gradient. *J Chem Phys* **42**(1):288–292.
- [139] K. Stephan et al. (2000). Computational analysis of functional connectivity between areas of primate cerebral cortex. *Philos Trans R Soc Lond B Biol Sci* **355**(1393):111–26.
- [140] B. Stieltjes et al. (2001). Diffusion tensor imaging and axonal tracking in the human brainstem. *Neuroimage* **14**(3):723–35.
- [141] J. Talairach, P. Tournoux (1988). *Co-planar stereotaxic atlas of the human brain : 3-dimensional proportional system : an approach to cerebral imaging*. G. Thieme ; New York : Thieme Medical Publishers, Stuttgart ; New York.
- [142] E. Tardif, S. Clarke (2001). Intrinsic connectivity of human auditory areas: a tracing study with dii. *Eur J Neurosci* **13**(5):1045–50.
- [143] C. Tench, P. Morgan, M. Wilson, L. Blumhardt (2002). White matter mapping using diffusion tensor mri. *Magn Reson Med* **47**(5):967–72.
- [144] A. Toga (2000). *Brain mapping the systems*. Academic Press, Sang Diego.
- [145] G. Tononi, G. Edelman (1998). Consciousness and complexity. *Science* **282**(5395):1846–51.
- [146] G. Tononi, A. McIntosh, D. Russell, G. Edelman (1998). Functional clustering: iden-tifying strongly interactive brain regions in neuroimaging data. *Neuroimage* **7**(2):133–49.
- [147] A. Toosy et al. (2003). Diffusion tensor imaging detects corticospinal tract involvement at multiple levels in amyotrophic lateral sclerosis. *J Neurol Neurosurg Psychiatry* **74**(9):1250–7.

- 
- [148] W. Tseng et al. (2000). Myocardial fiber shortening in humans: initial results of mr imaging. *Radiology* **216**(1):128–39.
- [149] W. Tseng et al. (2003). Diffusion tensor mri of myocardial fibers and sheets: correspondence with visible cut-face texture. *J Magn Reson Imaging* **17**(1):31–42.
- [150] D. Tuch (2002). *Diffusion MRI of Complex Tissue Structure*. Ph.D. thesis, Massachusetts Institute of Technology, MA, USA.
- [151] D. Tuch, T. Reese, M. Wiegell, V. Wedeen (2003). Diffusion mri of complex neural architecture. *Neuron* **40**(5):885–95.
- [152] D. Tuch et al. (2002). High angular resolution diffusion imaging reveals intravoxel white matter fiber heterogeneity. *Magn Reson Med* **48**(4):577–82.
- [153] N. Tzourio et al. (1998). Functional anatomy of dominance for speech comprehension in left handers vs right handers. *Neuroimage* **8**(1):1–16.
- [154] D. Van Essen et al. (1990). Modular and hierarchical organization of extrastriate visual cortex in the macaque monkey. *Cold Spring Harb Symp Quant Biol* **55**:679–96.
- [155] M. Victor, A. Ropper, R. Adams (2000). *Principles Of Neurology*.
- [156] E. von dem Hagen, R. Henkelman (2002). Orientational diffusion reflects fiber structure within a voxel. *Magn Reson Med* **48**(3):454–9.
- [157] S. Warach, W. Chien, D amd Li, M. Ronthal, R. Edelman (1992). Fast magnetic resonance diffusion-weighted imaging of acute human stroke. *Neurology* **42**(9):1717–23.
- [158] D. Watts, S. Strogatz (1998). Collective dynamics of 'small-world' networks. *Nature* **393**(6684):440–42.
- [159] V. Wedeen, T. Reese, V. Napadow, R. Gilbert (2001). Demonstration of primary and secondary muscle fiber architecture of the bovine tongue by diffusion tensor magnetic resonance imaging. *Biophys J* **80**(2):1024–8.
- [160] V. Wedeen et al. (2000). Mapping fiber orientation spectra in cerebral white matter with fourier-transform diffusion mri. vol. 8 of *Proc. Intl. Soc. Mag. Reson. Med*, p. 82.
- [161] R. Weller, J. Kaas (1987). Subdivisions and connections of inferior temporal cortex in owl monkeys. *J Comp Neurol* **256**(1):137–72.
- [162] J. White, E. Southgate, J. Thomson, S. Brenner (1986). *Philos Trans R Soc London B* **314**:1–340.
- [163] M. Wiegell, H. Larsson, V. Wedeen (2000). Fiber crossing in human brain depicted with diffusion tensor mr imaging. *Radiology* **217**(3):897–903.



- [164] U. Wieshmann et al. (1999). Reduced anisotropy of water diffusion in structural cerebral abnormalities demonstrated with diffusion tensor imaging. *Magn Reson Imaging* **17**(9):1269–74.
- [165] M. Young (1992). Objective analysis of the topological organization of the primate cortical visual system. *Nature* **358**(6382):152–5.
- [166] E. Zaidel, F. Aboitiz, J. Clarke (1995). Sexual dimorphism in interhemispheric relations: anatomical-behavioral convergence. *Biol Res* **28**(1):27–43.
- [167] C. J. Zaidel E, Aboitiz F (1995). Sexual dimorphism in interhemispheric relations: anatomical-behavioral convergence. *Biol Res* **28**(1):27–43.
- [168] K. Zhang, T. Sejnowski (2000). *Proc. Natl. Acad. Sci. U.S.A.* **97**:5671.
- [169] Y. Zhang, M. Brady, S. Smith (2001). Segmentation of brain mr images through a hidden markov random field model and the expectation-maximization algorithm. *IEEE Trans Med Imaging* **20**(1):45–57.
- [170] L. Zhukov et al. (2003). Level set modelling and segmentation of dt-mri brain data. *J Electron Imag* **12**(1):125–33.



---

# Curriculum Vitæ

---

Name: Patric Hagmann  
Citizenship: Swiss  
Birthdate: July 25, 1975  
Origin: Däniken, Switzerland  
Marital status: Single

## Contact information

Address: Route de la Plaine, 5  
1022 Chavannes-Renens  
Switzerland  
Phone: +41 76 512 93 55  
Email: Patric.Hagmann@epfl.ch

## Currently

- ***Ph.D. student*** at Signal Processing Institute of École Polytechnique Fédérale de Lausanne
- ***Junior Medical Doctor*** affiliate of Department of Radiology, Lausanne University Hospital.

## Obtained Diplomas

- ***Federal Diploma in Medicine***, University of Lausanne
- ***Postgraduate Diploma in Biomedical Engineering***, École Polytechnique Fédérale de Lausanne
- ***Medical Doctorate***, University of Lausanne

## Awards and Fellowships

- Swiss National Science Foundation MD/PhD award, 2003: 3 year fellowship funding

- Faculty Prize 2004 of Medical School, University of Lausanne

## Publications

### Journal papers

- Wedeen VJ, Hagmann P, Tseng WYI, Reese T, Weisskoff RM. Mapping complex tissue architecture with diffusion spectrum magnetic resonance imaging. *Magn Res Med*, 2005 (accepted)
- Jonasson L, Bresson X, Hagmann P, Cuisenaire O, Meuli R, Thiran JP. White matter fiber tract segmentation in DT-MRI using geometric flows. *Medical Image Analysis*, 2004 (accepted)
- Hagmann P, Thiran JP, Jonasson L, Vandergheynst P, Clarke S, Maeder P, Meuli R. DTI mapping of human brain connectivity: statistical fibre tracking and virtual dissection. *Neuroimage*. 2003 Jul;19(3):545-54.
- Wolfensberger TJ, Hagmann P. Bilaterale schmerzlose Lidschwellungen : *Ophthalmologie* 1999 Sep;96(9):620-1

### Conference papers

- Hagmann P, Jonasson L, Thiran JP, Meuli R, Wedeen VJ. Tractography by segmentation of high angular resolution diffusion MR images. *Proc. Intl. Soc. Mag. Reson. Med*; 13, p. 388 (2005)
- Hagmann P, Masip S, Lin CP, Tseng WYI, Wedeen VJ, Thiran JP. Modelization and restoration of diffusion spectra. *Proc. Intl. Soc. Mag. Reson. Med*; 13, p. 1318 (2005)
- Jonasson L, Hagmann P, Thiran JP, Wedeen VJ. Fiber tracts of high angular resolution diffusion MRI are easily segmented with spectral clustering. *Proc. Intl. Soc. Mag. Reson. Med*; 13, p. ? (2005)
- Jonasson L, Hagmann P, Richero C, Bresson X, Pollo C, Meuli R, Thiran JP. Coupled, region based level sets for segmentation of the thalamus and its subnuclei in DT-MRI. *Proc. Intl. Soc. Mag. Reson. Med*; 13, p. 731 (2005)
- Hagmann P, Wedeen VJ. Why diffusion contrast is positive. *ISMRM Workshop on Methods for Quantitative Diffusion MRI of Human Brain*; p. ? (2005)
- Hagmann P, Cammoun L, Martuzzi R, Maeder P, Clarke S, Thiran JP, Meuli R. DTI tractography of the Wernicke and Broca connectivity in right and left hander *Proc. Intl. Soc. Mag. Reson. Med*; 12, p. 625 (2004)

- Hagmann P, Reese T, Tseng WYI, Meuli R, Thiran JP, Wedeen VJ. Diffusion Spectrum Imaging tractography in complex cerebral white matter: an investigation of the centrum semiovale. *Proc. Intl. Soc. Mag. Reson. Med*; 12, p. 623 (2004)
- Martuzzi R, Cammoun L, Hagmann P, Maeder P, Clarke S, Thiran JP, Meuli R. Language-related asymmetries of the arcuate fasciculus in right- and left- handers: a DT-MRI and fMRI combined study. *Proc. 10th Int. Conf. Functional Mapping of the Human*, p. 1087.553001, June 2004
- Butz T, Hagmann P, Tardif E, Meuli R, Thiran JP. A new brain segmentation framework. *Lecture Notes in Computer Science, Proc. MICCAI 2003*, Vol. 2879, pp. 586-593, 2003
- Hagmann P, Thiran JP, Jonasson L, Vandergheynst P, Clarke S, Maeder P, Meuli R. Mapping Brain Connectivity with Statistical Fibre Tracking and Virtual Dissection. *Proc. Intl. Soc. Mag. Reson. Med, ISMRM 11th scientific meeting, Toronto, Canada*, Vol. 11, p. 2156, July 2003
- Jonasson L, Hagmann P, Bresson X, Meuli R, Cuisenaire O, Thiran JP. White Matter Mapping in DT-MRI Using Geometric Flows. *Computer Aided Systems Theory - EUROCAST 2003*, Vol. 2809, pp. 585-596, 2003
- Hagmann P, Clarke S, Thiran JP, Maeder P, Meuli R. Variation in fiber spreading from the human corpus callosum: a statistical study on DT-MRI data. *Proc. 8th Int. Conf. Functional Mapping of the Human Brain*, p. 10015, June 2002
- Hagmann P, Thiran JP, Vandergheynst P, Clarke S, Meuli R. Statistical Fiber Tracking on DT-MRI data as a Potential Tool for Morphological Brain Studies. *ISMRM Workshop on Diffusion MRI: Biophysical Issues (2002)*, p. 216, March 2002
- Bach Cuadra M, Gomez J, Hagmann P, Pollo C, Villemure JG, Dawant BM, Thiran JP. Atlas-Based Segmentation of Pathological Brains Using a Model of Tumor Growth. *Medical Image Computing and Computer-Assisted Intervention*, 2002; 380-387; Tokyo; Japan; 2002.

### Invited Talks

- Hagmann P, Jonasson L, Thiran JP, Meuli R, Wedeen VJ. Tractography by segmentation of high angular resolution diffusion MR images. *Proc. Intl. Soc. Mag. Reson. Med, ISMRM 13th scientific meeting, Miami Beach, USA, May 2005 (accepted)*
- Hagmann P, Cammoun L, Martuzzi R, Maeder P, Clarke S, Thiran JP, Meuli R. DTI tractography of the Wernicke and Broca connectivity in right and left hander *Proc. Intl. Soc. Mag. Reson. Med, ISMRM 12th scientific meeting, Kyoto, Japan, May 2004*

- Hagmann P, Reese T, Tseng WYI, Meuli R, Thiran JP, Wedeen VJ. Diffusion Spectrum Imaging tractography in complex cerebral white matter: an investigation of the centrum semiovale. Proc. Intl. Soc. Mag. Reson. Med, ISMRM 12th scientific meeting, Kyoto, Japan, May 2004
- Hagmann P, Clarke S, Thiran JP, Maeder P, Meuli R. Variation in fiber spreading from the human corpus callosum: a statistical study on DT-MRI data. Proc. 8th Int. Conf. Functional Mapping of the Human Brain, p. 10015, June 2002

### Cover Pages

- Cover page of NeuroImage, July 2003.

### Press Coverage

- Swiss National Science Foundation : Image of the month Juni 2004. Dissection virtuelle du cerveau vivant. [http : //www.snf.ch/fr/com/prr/prr\\_arh\\_04jun08.asp](http://www.snf.ch/fr/com/prr/prr_arh_04jun08.asp)
- Article in Science et Vie, September 2004. Une carte des connexions cérébrales devrait faciliter le travail du chirurgien.
- Article in Science et Vie, Hors Serie : La Science en 2004, December 2004. Images de l'année 2004, catégorie biomédical.

### Educational History

- **November 2001 – March 2005**: Ph.D. student at Signal Processing Institute of École Polytechnique Fédérale de Lausanne
- **September 2003 – October 2003**: Visiting research fellow at NMR-Center, MGH, Harvard Medical School, Boston.
- **March 2001 – September 2001**: Postgraduate Program in Biomedical Engineering at École Polytechnique Fédérale de Lausanne
- **1999 – 2000**: Last year of medical school at University of Lausanne.
- **1998 – 1999**: Clinical attachments in: general surgery, paediatrics , ophthalmology, ENT (Canada), internal medicine, dermatology (UK), gynaecology et obstetrics (India). Laboratory attachment: molecular biology at Institute for Microbiology of Basel
- **1997 – 1998**: Fourth year of medical school at University of Leicester (UK). Clinical attachments in: internal medicine, general surgery, gynaecology and obstetrics, paediatrics, psychiatry.
- **1996 – 1997**: Third year of medical school at University of Basel.

- **1994 – 1996**: First and second year of medical school at University of Lausanne.
- **1994**: Federal Diploma of Maturity type C (sciences)

## Skills

### Languages

Swiss German:	mother tongue
French:	mother tongue
German:	fluent oral and written
English:	fluent oral and written

### Computing

Operating systems:	Linux, Unix, Windows
Programming languages:	Matlab (algorithmics and 3D visualization), C/C++